



N° d'ordre NNT : xxx

THÈSE DE DOCTORAT DE L'UNIVERSITÉ DE LYON
opérée au sein de
l'Université Claude Bernard Lyon 1

École Doctorale ED52
Physique et Astrophysique de Lyon

Spécialité de doctorat :
Discipline : Physique médicale

Soutenue publiquement à huis clos le 14/12/2018, par :
Mattia Fontana

Tests and characterization of gamma cameras for medical applications

Test et caractérisation de caméras gamma pour le médical

Devant le jury composé de :

Llosá Gabriela, Professeur associée, IFIC - Institut de Fisica Corpuscular, Paterna, Espagne
Rapportrice

Thirolf Peter, Professeur associé, Fakultät für Physik der LMU München - Lehrstuhl für Experimentalphysik - Medizinhce Physik, Garching, Allemagne
Rapporteur

Augier Corinne, Professeur, IPNL - Institut de Physique Nucléaire de Lyon, France
Examinateuse

Cerello Piergiorgio, INFN - Istituto Nazionale di Fisica Nucleare, sezione di Torino, Italie
Examinateur

Morel Christian, Professeur, CPPM - Centre de Physique de Particules de Marseille - Aix-Marseille Université, Marseille, France
Examinateur

Rafecas Magdalena, Professeur, Institut für Medizintechnik - Universität zu Lübeck, Allemagne
Examinateuse

Létang Jean Michel, maître de conférences, CREATIS - Centre de Recherche en Acquisition et Traitement de l'Image pour la Santé, Lyon, France
Co-directeur de thèse

Testa Étienne, maître de conférences, IPNL - Institut de Physique Nucléaire de Lyon, France
Directeur de thèse

Dauvergne Denis, Directeur de Recherche CNRS, LPSC - Laboratoire de Physique Corpusculaire de Grenoble, France
Invité

Tests and characterization of gamma cameras for medical applications

PhD Candidate

MATTIA FONTANA

Thesis directors

ÉTIENNE TESTA and JEAN MICHEL LÉTANG

Université Claude Bernard
Lyon 1
Physics department
Doctoral school ED52:
Physics and Astrophysics

Defended on December the 14th
2018

Abstract

The application of nuclear and particle physics techniques in the field of medical diagnosis and pathology treatment is nowadays well-established in the clinical routine. In particular, several medical imaging techniques are based on the exploitation of elementary particles (Positron Emission Tomography (PET), Single Photon Emission Computed Tomography (SPECT), Computed Tomography (CT) scans, etc.), as well as treatment methods, mainly concerning cancer, which causes about 9 millions deaths per year all over the world.

In this context, ion beam therapy is a promising technique in cancer treatment because of the ion defined range and favorable dose delivery features with respect to standard photon radiotherapy. Strict and precise treatment planning and monitoring are now key points for the method developments and full exploitation. In particular, with the aim of optimizing the ion treatment effectiveness, the ion range monitoring is mandatory: different solutions have been explored, but an online treatment check is still a challenge. The ion beam treatment monitoring is mainly performed by means of secondary charged or neutral particles. In this context, the detection of the prompt-gammas (PG) emitted during treatments has proven its potential in the ion range control in real time. Since the first evidence of the existing correlation between the emitted gamma profile fall-off and the Bragg peak position, several groups are involved in research activities in order to develop and optimize instruments and methods with the aim of improving this monitoring technique. Among the others, collimated and Compton cameras are being studied and optimized for this application. The same detectors can also be employed in nuclear medicine for the detection of the radioactive elements decay products.

A collaboration of 4 laboratories in France, called *Contrôle en Ligne de l'hadronthérapie par Rayonnements Secondaires* (CLaRyS), is involved in the parallel development of two composite detectors for ion beam monitoring and nuclear medicine applications, and this thesis is carried out within this collaboration with the detectors clinical trial as final aim.

The development project started a few years ago and is now at the final stage. The two cameras have been designed according to simulation studies, and the different components are now under tests. The collimated camera is composed of a multi-slit tungsten mechanical collimator, set in front of an absorber composed of 30 Bismuth Germanium Oxide - $\text{Bi}_{12}\text{GeO}_{20}$ (BGO) blocks, for a total size of $210 \times 175 \times 30 \text{ mm}^3$; each block presents a streaked structure with a 8×8 pseudo-pixel matrix and the signal is read-out by 4 photomultipliers. A $\sim 3 \text{ ns}$ time resolution can be achieved on average for the prompt-gamma detection. The same absorber is part of the Compton camera, in addition to a scatterer section composed of 7 Double-sided Silicon Strip Detectors (DSSDs) $96 \times 96 \times 2 \text{ mm}^3$ each. With the collimated camera, the parallel emitted photons are selected by the collimator and a mono-dimensional emission profile can be reconstructed. The Compton camera has a more efficient detection technique, thanks to the absence of a mechanical collimation system, and could potentially lead to 3D information via the reconstruction of the Compton cones. These features make it suitable for the application in nuclear medicine, in particular as an alternative to the present SPECT collimated cameras, allowing for accurate and efficient image reconstructions with the usage of high energy gamma source, which should reduce image blurring effects due to attenuation in the patient and the total released dose with respect to the present clinical routine.

Concerning the monitoring of ion beam therapy treatments, an additional detector component is needed to temporally and spatially tag the incoming beam ions and help rejecting the relevant background (mostly due to neutrons) which strongly affects the prompt-gamma yield. A scintillating fiber tagging hodoscope, which can be coupled to both collimated and Compton camera, is under development: it is composed of 2 perpendicular planes of 128 scintillating fibers, read-out from both sides by 8 64-channel photomultipliers by Hamamatsu.

The thesis work consists in the critical evaluation, characterization and tuning of the different components, together with the associated electronics, and of the complete detectors on beam. In parallel, simulation studies can improve the detection technique and optimize the detector structure, as well as pave the way for further applications.

After a general introduction devoted to expose the thesis context in chapter 1, an overview of the instrumental and technical state of the art of the gamma cameras is given in chapter 2. Chapter 3 focuses on the two cameras developed by the CLaRyS; the camera components are described in details, and all the characterization measurements performed during the three years of my PhD thesis are explained. Chapter 4 and 5 presents the simulation studies I performed with the aim of investigating the potential of the developed detectors for the application on ion beam therapy monitoring and nuclear medicine, respectively. The entire chapter 6 is dedicated to the description of the tests performed on proton beams for the detector characterization measurements. The final chapter 7 is used to summarize and discuss all the results obtained in this thesis work; furthermore, the perspectives of the project are fixed on a timeline for the next future, and new research directions emerging from the obtained results are proposed.

Contents

Prologue	1
1 Context	3
1.1 Ion beam therapy	5
1.1.1 Physics of ion beam therapy	6
1.1.2 Accelerators and beam delivery	11
1.1.3 Biological effects of ion beam therapy	13
1.1.4 Treatment planning	14
1.1.5 Advantages and drawbacks with respect to standard radiotherapy	14
1.1.6 Quality assurance in ion beam therapy	14
1.1.7 Ion range verification	14
1.1.8 Secondary radiation techniques	14
1.1.8.1 Positron Emission Tomography	14
1.1.9 Prompt-gammas: physics and features	14
1.1.10 State of the art of range verification	14
1.2 Nuclear medicine	14
1.2.1 PET and SPECT	15
1.2.2 State of the art of PET and SPECT	15
2 Prompt gamma detection and imaging	17
2.1 Photons	18
2.1.1 Photon interactions in matter	18
2.1.2 Photon detection	18
2.2 Prompt gammas	18
2.2.1 Ion range monitoring with prompt gamma radiation	18
2.3 Gamma cameras	18
2.3.1 Applications in medicine	18
2.3.2 Ion beam range monitoring	18
2.3.3 Nuclear medicine	18
2.4 Gamma cameras state of the art	18
3 CLaRyS prototypes	19
3.1 CLaRyS gamma camera components	20
3.1.1 Scatterer	21
3.1.1.1 Scatterer Front-End card	24
3.1.1.2 Scatterer thermal regulated box	25
3.1.2 Collimator	25
3.1.3 Absorber	26
3.1.3.1 Absorber Front-End and read-out cards	28
3.1.3.2 Absorber mechanical support	30
3.1.4 Beam tagging hodoscope	31
3.1.4.1 Hodoscope Front-End card	32
3.1.4.2 Hodoscope mechanical support	35
3.1.4.3 Small hodoscope prototypes	35
3.1.5 Camera acquisition system	36
3.1.6 Camera acquisition, monitoring and slow control software	37

3.1.7 Camera integration and mechanical support	40
3.1.8 Data analysis and image reconstruction	41
3.2 Camera component characterization and development status	44
3.2.1 Scatterer silicon layer characterization	44
3.2.2 Absorber BGO blocks characterization	46
3.2.2.1 Space and energy calibration and characterization	47
3.2.2.2 Qualitative test of spatial reconstruction accuracy	48
3.2.2.3 Pixel identification and energy calibration algorithm	49
3.2.2.4 Time response characterization method	50
3.2.2.5 Results: PM gain equalization	51
3.2.2.6 Results: block spatial precision	53
3.2.2.7 Pixel identification	56
3.2.2.8 Pixel energy calibration	56
3.2.2.9 Time characterization	62
3.2.2.10 Results for the 30 blocks	62
3.2.3 Hodoscope PMs characterization	62
3.2.4 Hodoscope fiber test with electron source	67
3.3 Summary and perspectives	70
3.3.1 Silicon scatterer	71
3.3.2 BGO absorber	72
3.3.2.1 Absorber upgrade	73
3.3.3 Scintillating fiber hodoscope	73
3.3.3.1 Hodoscope upgrade	74
3.3.4 Acquisition and software	74
3.4 Conclusion	75
4 Compton camera application for ion beam therapy monitoring	77
5 Compton camera application in nuclear medicine	79
5.1 Introduction	80
5.2 Material and methods	81
5.2.1 Radioactive sources	81
5.2.2 Compton camera simulation and data analysis	81
5.2.2.1 Simulation settings	81
5.2.2.2 Data collection and analysis	83
5.2.2.3 Compton camera study for SPECT application	84
5.2.3 Anger camera simulation and data analysis	85
5.2.3.1 Simulation settings	86
5.2.3.2 Data analysis	86
5.2.4 Figures of merit for the comparison study	89
5.3 Results: Compton camera study for SPECT application	92
5.3.1 Influence of Compton camera scatterer detector energy resolution	92
5.3.2 Compton camera coincidence study	93
5.3.3 Compton camera desing study	94
5.4 Results: Benchmark of Compton camera and Anger camera performance	95
5.5 Summary and discussion	98
6 Beam tests	101
6.1 Hodoscope: december 2017	102
6.2 Hodoscope: may 2018	102

6.3 Collimated camera: august 2018	102
6.4 Collimated camera: september 2018	102
7 Conclusions and discussion	103
Appendices	105
Appendix A Compton camera data format	107
A.1 Introduction	107
A.2 General features	107
A.2.1 Common information	107
A.2.1.1 Front End number	107
A.2.1.2 Pre-trigger and trigger	109
A.2.1.3 Mode number	109
A.3 Physical data format	111
A.3.1 Scatterer detector data format	111
A.3.2 Absorber detector data format	111
A.3.3 Beam hodoscope data format	114
A.4 Slow control, trigger and monitoring data format	114
A.4.1 Communication architecture	114
A.4.2 Transport protocol and processor packets	115
A.4.2.1 Definitions	115
A.4.2.2 Data encoding	116
A.4.2.3 Packets format	116
A.4.2.4 Possible control symbols	117
A.4.3 Transport layer	117
A.4.3.1 Control packet	117
A.4.3.2 Configuration packets	118
A.4.3.3 Monitoring process (Front End cards → μ-TCA)	119
A.4.3.4 Special command process (μ-TCA → Front End cards)	121
A.4.4 Data packets (Front End card → μ-TCA)	121
A.5 UDP packets format	123
A.6 Data throughput expected in clinical conditions	124
A.6.1 Clinical intensities	124
A.6.1.1 Review: detector and target sizes	124
A.6.2 Coincidence rate	125
A.6.3 Data flow (Front End cards → μ-TCA)	125
A.6.4 Acquisition data flow (μ-TCA → Acquisition PC)	126
A.6.5 Conclusions	127
List of abbreviations	129
Bibliography	135

List of Figures

1.1	Relative dose as a function of the particle depth in water for photons at different energies, protons, and carbon ions.	6
1.2	Treatment planning of lung cancer for the irradiation with x-rays (left) or carbon ions (right) (in Durante et al. 2016).	7
1.3	Schematic view of the abrasion-ablation model for the description of ion-nucleus interactions (in Durante et al. 2016): b is the distance between projectile center and target nucleus center, v is the projectile velocity.	9
1.4	Effects of nuclear interactions on the primary beam and resulting dose distribution.	10
3.1	Schematic view of the two CLaRyS gamma camera prototypes: the multi-collimated camera (a) and the Compton camera (b), both coupled to the beam tagging hodoscope. The ion beam is represented by the red line, and some beam bunches has been highlighted. The detection principle is also sketched for the two detectors: the tungsten collimator select the parallel incoming photons for the multi-slit collimated camera (a), while the Compton cone is reconstructed with the two interactions in scatterer and absorber in the Compton camera (b).	21
3.2	Overview of the scatterer layers, with its working principle (a) and a picture of the detector connected to the FE card in the thermal regulated box (b).	23
3.3	Scatterer silicon layers equipment: final version of the FE card (a) and scheme of the detector integration in the thermal regulated box (b).	26
3.4	Tungsten collimator and its setup in the multi-slit collimated camera. The two tungsten multi-slit collimators are placed in front of a 6×5 BGO block absorber setup in its mechanical support (see section 3.1.3).	26
3.5	Components of an absorber module and its working principle.	28
3.6	Absorber read-out electronics: FE card (a) and ASM board (b).	29
3.7	Details of the temporary absorber acquisition based on the Altera development card.	30
3.8	Absorber front view with the BGO block lines arranged in the mechanical support (a). Scheme of the BGO absorber with its mechanical support (b).	31
3.9	128 \times 128 scintillating fiber hodoscope on its 2-dimensional moving support.	33
3.10	Details of the scintillating fiber hodoscope setup.	34
3.11	HODOPIC board (a) and scheme of the beam-tagging hodoscope two-dimensional moving support (b).	34
3.12	Hodoscope small prototypes.	36
3.13	Acquisition system components: μ -TCA crate (a), AMC40 board (b) and THOR card (c).	38
3.14	Schematic view of the Compton camera acquisition system. For the multi-collimated camera, the trigger and pre-trigger signals are the same.	39
3.15	Software tools: user interface of the acquisition C++ software (a) and example of the ROOT (Brun et al. 1997) monitoring software visualization for the beam tagging hodoscope 32 \times 32 fiber prototype.	40
3.16	Details of the gamma camera integration and mechanical support.	41
3.17	Complete Compton camera with beam tagging hodoscope on the developed mechanical supports.	42

List of Figures

3.18 Scheme of the spatial and energy characterization test-bench.	47
3.19 Details about the BGO block time response characterization.	48
3.20 Logic for the event assignment to a single pixel. The dual pseudo-pixel grid is displayed: in white the mid points on the pseudo-pixel edges along rows, in red along columns. The sign of the outer products detailed in the red box are used to define the column and row (so that the pseudo-pixel) where to assign the reconstructed event.	49
3.21 Reference BGO block raw signals collected with the Wave Catcher acquisition system. The four outputs of the single PMTs are shown together with the sum signal.	51
3.22 PM signal amplitude spectra before (a) and after (b) the PM gain equalization.	52
3.23 1D integrated position distribution on the two transverse dimensions before (a) and after (b) the PM gain equalization. Blue curves: horizontal dimension. Green curves: vertical dimension.	52
3.24 Block energy spectrum before (a) and after (b) the PM gain equalization.	53
3.25 2D reconstructed position map before (a) and after (b) the PM gain equalization.	53
3.26 2D reconstructed position maps during a 2-mm step scan performed with the ^{60}Co source with the line aperture from the left to the right size of the block surface. 4 reference measurements points, the position of the aperture is shown by the semi-transparent yellow band.	54
3.27 2D reconstructed position maps during a 2-mm step scan performed with the ^{60}Co source with the line aperture from the bottom to the top side of the block surface. 4 reference measurements points, the position of the aperture is shown by the semi-transparent yellow band.	55
3.28 2D reconstructed position maps during a 1-mm step scan performed with the ^{60}Co source with the line aperture. 9 reference measurements points, the position of the aperture is shown by the semi-transparent yellow band.	57
3.29 1D integrated position distributions on the two transverse dimensions with the retrieved position of the pseudo-pixel average center (a). Reconstructed 2D map with the identified pseudo-pixels positions and surfaces.	58
3.30 Auxiliary position map used for the assignment of the reconstructed events to a single pixel. The highlighted points represent the “valleys” between neighboring pixels on their separation borders.	58
3.31 2D map of the reconstructed event assignations to pseudo-pixels.	59
3.32 Single pseudo-pixels (a) and whole block (b) energy spectra with the ^{22}Na source before (left) and after (right) the calibration process. The whole block spectra are reported in logarithmic scale. Three non calibrated spectra of pixels in reference positions (border, mid-center and center area) on the block are also reported with the non calibrated spectrum (a normalization factor has been applied for visualization purpose).	60
3.33 Relative number of entries for each pseudo-pixel as a function of the pixel relative position, represented by the row and column numbers (0 to 8 from left to right and bottom to top of the block surface). Figure(a) shows the entries in a selected energy window around 511 keV, Figure(b) in an energy window around 1275 keV. All the entries are normalized to the maximum collected number of entries, corresponding to 511 keV events in the central section of the block.	61
3.34 Distribution of arrival time differences between reference scintillator and BGO block.	62

3.35 Test-bench and tools for the characterization measurements performed on the Hamamatsu PMs of the beam tagging hodoscope.	65
3.36 Details of the hodoscope PMs and of the performed characterization measurements.	66
3.37 Two-dimensional response maps of one of the Hamamatsu PMs for the scintillating fiber hodoscope readout, obtained with the irradiation with a blue LED. The signal amplitude is normalized to the reference PM response.	67
3.38 Two-dimensional response maps of the Hamamatsu PMs for the scintillating fiber hodoscope readout, obtained with the irradiation with a blue LED. The signal amplitude is normalized to the reference PM response and then to each PM maximum detected amplitude.	68
3.39 Cross-talk study on neighboring PM pixels. The experimental results obtained with the irradiation with a blue LED through the plastic fiber mask on a reference PM (right) are compared to the specifications provided by the producer, measured in similar conditions (left). The cross-talk is expressed in % with respect to the irradiated anode, which is represented by the light-blue cell with 100% of the signal.	69
3.40 Comparison of the simulated distribution of energy deposited by electrons from the ^{90}Sr source on a single hodoscope fiber to the experimental signal amplitude distribution from a scintillating fiber irradiated with the ^{90}Sr source.	70
 5.1 Sketch of the simulated geometry of the two systems: Anger camera (left) and Compton camera (right), in 3 dimensions (top line) and side projection (bottom line).	82
5.2 Radial event distribution normalized by the circular surface corresponding to each bin for 4 representative source energies, with the linear fit performed for background rejection. The total number of simulated primaries for each data set is 10^8	88
5.3 Comparison between expected entries in the central collimator hole (blue dashed curve) calculated according to pure geometrical factors and detector interaction cross section and simulated detected entries after background rejection (red solid curve) with null spatial resolution (ideal detector) to avoid resolution effects and lower energy threshold set to 80 keV.	89
5.4 Normalized radial distribution with background rejection (red solid lines) compared to normalized radial distribution for infinite density collimator (blue dashed lines).	90
5.5 Normalized radial distribution with no event selection (red solid lines) compared to normalized radial distribution for full collimator (green dashed lines). Both curves are normalized to the maximum of the raw radial distribution.	91
5.6 Reconstructed radial distribution standard deviation as a function of the source energy. Two energy resolution values are set to the silicon detectors ($\sigma_E = 2\text{keV}$ - red dots solid line - and $\sigma_E = 4\text{keV}$ - blue dots dashed line), the Doppler broadening effect has been removed (green horizontal triangles dashed line) and the scatterer material has been changed with CdTe solid state detectors (black vertical triangles dashed line), for a fixed energy resolution of $\sigma_E = 2\text{keV}$	93

List of Figures

5.7 (a): number of true (green) and random (red) coincidences as a function of the source activity in the range 1-500 MBq, for the reference energy of 555 keV. (b): Percentage of random coincidences as a function of the source energy, with a fixed source activity of 200 MBq. Compton camera parameters: time resolution FWHM of 20 ns for silicon detectors, 3 ns for BGO and a coincidence window of 40 ns. The source branching ratio has been set to 100% for all sources for simplicity in the comparison of results.	94
5.8 Results of the Compton camera design study: reconstructed events efficiency (left) and standard deviation of the radial event distribution (right) as a function of the primary gamma energies for four reference energies and five scatterer stack configurations, with seven, six, five, four and three layers.	95
5.9 Overlap of the normalized radial distributions for 4 selected source energies.	96
5.10 Detection efficiency as a function of the source energy. Source activity = 200 MBq, Compton camera silicon detector $\sigma_E = 2 \text{ keV}$	96
5.11 Standard deviation of the radial event distributions as a function of the source energy. Source activity = 200 MBq, Compton camera silicon detector $\sigma_E = 2 \text{ keV}$	97
5.12 Signal-to-background ratio as a function of the source energy. Source activity = 200 MBq, Compton camera silicon detector $\sigma_E = 2 \text{ keV}$	97
A.1 Data acquisition logic: pre-trigger and trigger generation and readout process.	110
A.2 Scatterer detector data format.	112
A.3 Absorber detector data format.	113
A.4 Beam hodoscope data format.	114
A.5 Architecture of communication between DAQ cards and μ -TCA.	115

List of Tables

3.1 Comparison of the results obtained with the two pixel-assignment methods.	59
3.2 Calibration and characterization results for 10 tested BGO blocks.	63
5.1 Radioactive sources used in the comparison study. Decay mode list: EC for electron capture, β^- for electron emission, β^+ for positron emission, IT for isomeric transition. Half-life expressed in days (d), hours (h) or minutes (m). Data extracted using the National Nuclear Data Center On-Line Data Service from the Evaluated Nuclear Structure Data File database, file revised as of (2017-05-17) (Bhat 1992).	82
A.1 Front End number associated to each Front End card.	108
A.2 Packet with an even byte number cargo.	116
A.3 Packet with an odd byte number cargo.	116
A.4 Control symbol definition.	117
A.5 Control symbol definition.	118
A.6 Definition of the acknowledgement packet.	118
A.7 Writing register packet.	119
A.8 Reading register packet.	119
A.9 Two special registers(μ -TCA \rightarrow Front End cards)	120
A.10 Measurement packet (Front End cards \rightarrow μ -TCA)	120
A.11 Monitoring packet.	120
A.12 Monitoring messages.	121
A.13 Special command packets	121
A.14 Special commands examples	122
A.15 Control symbol for pre-trigger, trigger and physical data.	122
A.16 Pre-trigger packet	123
A.17 Trigger packet	123
A.18 Physical data packet	123
A.19 Coincidence and single rate as a function of the beam intensity. The BGO single rate corresponds to the pre-trigger rate.	125
A.20 Data flux between FE cards and μ -TCA.	126
A.21 Data flow between μ -TCA and acquisition PC.	126
7.22 Acquisition format of the Compton camera data.	128

Prologue

1

Context

Contents

1.1 Ion beam therapy	5
1.1.1 Physics of ion beam therapy	6
1.1.2 Accelerators and beam delivery	11
1.1.3 Biological effects of ion beam therapy	13
1.1.4 Treatment planning	14
1.1.5 Advantages and drawbacks with respect to standard radiotherapy . .	14
1.1.6 Quality assurance in ion beam therapy	14
1.1.7 Ion range verification	14
1.1.8 Secondary radiation techniques	14
1.1.9 Prompt-gammas: physics and features	14
1.1.10 State of the art of range verification	14
1.2 Nuclear medicine	14
1.2.1 PET and SPECT	15
1.2.2 State of the art of PET and SPECT	15

1 Context

The application of physics concepts and techniques to the field of health-care is nowadays well-established in the clinical routine. Even if physical techniques have been used in medicine from the earliest time (Duck 2014), the discipline today known as “medical physics” emerged and grown in the past century thanks to the increasing knowledge and use of ionizing radiations both for diagnosis and disease treatment. In the late 19th century, the x-ray discovery by Röntgen, the radioactivity discovery by Henri Becquerel, and the radium and radioactive isotopes studies by Pierre and Marie Curie paved the way to the whole medical physics practice of the next century, where x-ray imaging and radiotherapy were soon established. Only three weeks after the discovery of the x-rays, Robert Jones and Oliver Lodge imaged with x-rays a boy’s hand (Cantor 1988), officially starting the diagnostic application of such a radiation. Following the first successes, more attention were given to radio-protection and dosimetry studies, and the investigations focused on new ways to use radioactive tracers for imaging purpose; this finally led to the birth of nuclear medicine, with the clinical use of the radioisotope ¹³¹In in 1939 (Kereiakes 1987). Nuclear medicine rapidly gained importance in the diagnosis clinical panorama, also thanks to the introduction of new detectors, such as the Anger camera introduced in the ’60s, and new imaging techniques, such as the detection of photons from positron annihilation (PET). Moreover, several alternative methods were proposed or implemented for diagnosis (MRI, ultrasounds, etc.). In parallel, x-rays were soon employed also for tumor treatment: already in 1896, Emil Grubbe irradiated a woman with breast cancer (Evans 1951), and in the same year in Lyon a patient with a stomach cancer has been treated by Victor Despeignes (Despeignes 1896; Foray 2016). One year later, a skin tumor were successfully irradiated in Vienna using x-rays. Thanks to the invention of the klystron, and, later, of the so-called “magnetron”, by the Varian brothers with William Webster Hansen, the radiotherapy could spread and become a clinical reality; more refined treatment techniques were then introduced with the development of commercial particle accelerators after World War 2 (Keevil 2012).

At present days, the medical physics progress strongly relies on technological development and computer science, which already revolutionized several fields of science. In particular, cancer research is now a key area for technical and technological development, concerning both diagnosis and treatment (Webb 2009). Cancer continues to be one of the major issues in the medical scenario: it is at present the second cause of death worldwide, but it is expected to surpass heart diseases and become the main killer in the next tens of years (Jemal et al. 2010; Thun et al. 2010). The last two decades saw important improvements in radiotherapy techniques and machines, with more precise dose planning and delivery, which enhanced the patient survival and strongly reduced the impact of radiations on healthy tissues. This was possible also thanks to refined imaging technologies, allowing for an accurate tumor volume definition, as well as for image-guided treatments. In this scenario, ion beam therapy, already proposed in the middle of the past century, is rapidly spreading thanks to novel beam delivery technologies, able to relatively reduce the treatment costs and allowing for a commercial diffusion of this treatment method (which is still very limited with respect to standard radiotherapy). Notwithstanding the remarkable steps forward disclosed in the last years, there is still wide room for improvements in this fields, which mainly requires strong imaging basis in order to fully profit of the treatment technique potential.

The work presented in this document have been carried out in this context and deals with the development of gamma imaging detectors to be applied in the field of quality assurance for ion beam treatment. Furthermore, the same detectors have been applied to the nuclear

medicine field in simulation, with the aim of assessing its possible clinical implementation for a future development of the nuclear medicine clinical routine.

In the following sections, a general overview of the two main domains concerned in this thesis work is given, with particular focus on the present status of the involved instrumentation.

1.1 Ion beam therapy

Radiation treatment is an essential component of the tumor therapy, being the second most applied and successful kind of therapy after surgery (Schardt et al. 2010). The majority of patients with localized malignant tumors are treated with radiations (Baskar et al. 2012; Durante et al. 2009; Moding et al. 2013), applied in several fractions in different days in order to reduce the damages to normal tissues (Bentzen 2006). The most of the patients treated with radio-therapy techniques receives standard photon treatments, with x-rays coming from linear electron accelerators, while a small percentage undergoes specialized gamma treatments like brachytherapy or gamma knife irradiations. About 1 % of the radiotherapy patients are irradiated with charged particle beams, with the so-called ion beam therapy (Durante et al. 2016).

Ion beam therapy, or “hadrontherapy”, is a cancer radiation treatment method based on light ion beams instead of photons. It was first proposed by Wilson in 1946 in a famous seminal paper (R. R. Wilson 1946); the author was asked by its director Ernest Lawrence to clarify the stopping process of protons in matter. Thanks to measurements at the Berkeley cyclotron, he highlighted the physical principles and the possible benefits driven by the implementation of such a kind of radiation in clinical treatments, with particular focus on the simple case of protons and some considerations about heavier ions, like alpha particles and carbon ions. At that time, the accelerator technologies were still under development after the invention of the cyclotron by Ernest O. Lawrence in 1930, which allowed to increase the range of charged particles in matter, in particular in cells and human tissues, and the treatment required beam energy were about to be reached. Pioneering studies of the biomedical applications of accelerated hadron beams were performed by Cornelius Tobias in 1948 (Blakely et al. 2009) in Berkeley (USA), and the first patients have been treated almost ten years later in the same laboratory by Lawrence and Tobias (Tobias et al. 1958, 1955) with protons and, later on, with He ions (Halperin 2006). New accelerators in four continents were used to continue the quest started in Berkeley, and the experience were extended to carbon ion beams from 1994 in Japan (Chiba), and Germany (Heidelberg - HIT).

Nowadays clinical adapted machines are well-established on the market, making ion beam therapy emerging as a wide-spread technique in the every-day cancer treatment routine all over the world. Starting from the early 2000's, many new treatment centers have been designed and built, mainly in Europe and Japan. An intense research effort has been dedicated to this field in the last decades; in addition to considerable improvements achieved in the accelerator technologies, new and refined imaging techniques allowed for important enhancement in the treatment planning, also supported by the continuous development of computer science and the growth of calculation power. In parallel, the biological implications of ion irradiation has been deeply investigated (Brahme 2004; Friedrich et al. 2012; Tobias et al. 1982). Moreover, since more and more patient are treated every year with this technique, more clin-

ical data are at present available for further study and the connection between physicists and physicians is strongly progressing both in the research field and in treatment practice. Several advancements are expected in the next years, following the extensive research work carried out by several groups in the world. In the following paragraph, the basic physical principles and features of this treatment method are explained, and advantages and drawbacks with respect to standard radiotherapy techniques are analyzed. After that, the need of ion range verification is discussed and detailed in order to reach the main topic for this thesis: the prompt-gamma detection.

1.1.1 Physics of ion beam therapy

High-energy beams of charged nuclear particles show a characteristic depth-dose distribution in matter which makes them suitable for the application in cancer treatment as a valid alternative to standard photon therapy (x-ray or megavolt beams), bringing several advantages to the patient side. The peculiar energy deposition profile (“Bragg curve”) is named for Sir William Henri Bragg, who investigated the slowing-down process of α particles in air (Bragg et al. 1904, 1905). Low-energy (x-rays) and high-energy photons interacting with the patient body lose their energy according to an exponential attenuation law, with the deposited dose decreasing at increasing depth. Even if high-energy photons can spare the entrance surface thanks to a dose peak shift of a few centimeters (mainly due to forward scattered Compton electrons), a high relative dose is delivered to the tissues along the whole beam path. In order to maximize the tumor volume-to-healthy tissue dose ratio, a standard photon treatment always foresees several irradiation fields from different entrance points and angles (see Figure 1.2). In contrast to photons, the energy deposited per unit track increases for increasing depth for protons and heavier ions; the depth-dose profile is characterized by an entrance low relative dose *plateau* and by a narrow high deposited dose peak at the end of the ion range (in the last few millimeters), called “Bragg peak”. A visual comparison of low- and high-energy photon, proton and carbon ion relative dose profile in water is given in figure 1.1.

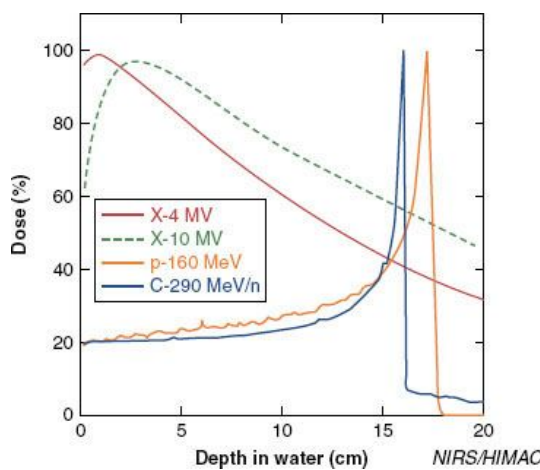


Figure 1.1: Relative dose as a function of the particle depth in water for photons at different energies, protons, and carbon ions.

In order to reach the target volume and deliver the prescribed dose to a tumor inside the patient body, the ions employed in treatment must be accelerated to about 60-70% of the

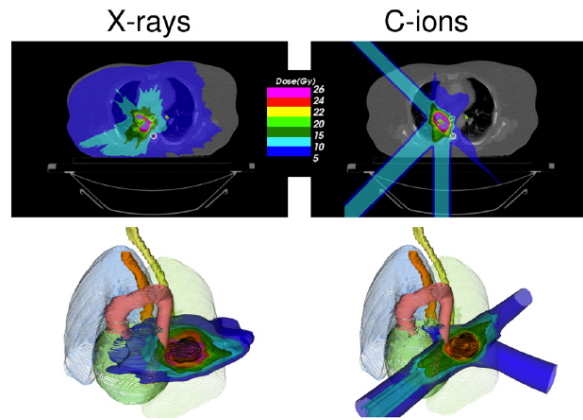


Figure 1.2: Treatment planning of lung cancer for the irradiation with x-rays (left) or carbon ions (right) (in Durante et al. 2016).

speed of light ($\beta = 0.6\text{--}0.7$, see Durante et al. 2016) via different acceleration techniques and machines, described in section 1.1.2. At that energy, the peculiar configuration of the charged particle energy deposition in matter is mainly governed by the energy loss in ionization of the atomic shell electrons, described by the formula attributed to Bethe (Bethe 1930) and Bloch (Bloch 1933), often referred as Bethe-Bloch formula, reported in equation 1.1 in its form independent of the mass density. This expression is also known as mass stopping power.

$$\frac{S}{\rho} = -\frac{dE}{\rho dx} = 4\pi N_A r_e^2 m_e c^2 \frac{z^2}{\beta^2 A} \left[\ln \frac{2m_e c^2 \beta^2 \gamma^2}{I} - \beta^2 - \frac{\delta}{2} - \frac{C}{Z} \right] \quad (1.1)$$

where N_A is the Avogadro's number ($6.022 \times 10^{23} \text{ mol}^{-1}$), r_e is the classical electron radius, m_e is the electron mass, z is the charge of the projectile, Z and A are the atomic number and weight of the target material, respectively, c is the speed of light, $\beta = v/c$ is the projectile velocity, $\gamma = (1 - \beta^2)^{-1/2}$, I is the mean excitation potential of the target material. The last two terms represent corrections for high energies (δ term) and low energies (C term) incident ions. As highlighted in Newhauser et al. 2015, the two main parameters governing the projectile energy loss rate in the human body are its velocity (energy) and the the material composition; the density in a patient can vary by almost three orders of magnitude, ranging from the air cavity in the lungs to the most dense bones.

The energy loss equation directly leads to the definition of the ion beam range in matter, which is the integral over the incident energy of the energy loss per track unit. In general, a CSDA is used for simplicity, assuming a mono-dimensional ion path and an average, continuos energy loss rate. To be noticed that the range is not a deterministic value, but it is intended as an average value and defined for the whole beam, not for single incident particles, which are affected by statistical fluctuations in the energy loss, leading to the so-called range straggling (described by different theoretical models, such as the ones in Bohr 1915; Landau 1944; Vavilov 1957). As realized by Bragg and Kleeman (Bragg et al. 1905), the range dependence on the incident particle energy can be practically expressed with the power law in equation 1.2

$$R(E) = \alpha E^p \quad (1.2)$$

where the constant α depends on the target material and the constant p is related to the projectile energy (or velocity) and ranges between 1 and 1.8 in proton-therapy (Durante et al. 2016). An empirical expression has been derived to scale the proton calculated range to heavier ions at the same energy per nucleon in the same material: it is reported in equation 1.3.

$$\frac{R_2}{R_1} = \frac{M_2 z_1^2}{M_1 z_2^2} \quad (1.3)$$

with M and z the ion mass and charge, respectively. Equivalently, for the same particle in different material, the scaling formula is reported in equation 1.4.

$$\frac{R_2}{R_1} = \frac{\rho_2}{\rho_1} \frac{\sqrt{A_1}}{\sqrt{A_2}} \quad (1.4)$$

with ρ and A density and atomic mass of the target material, respectively.

It is clear from this considerations that the ion range prediction is affected by uncertainties due to both the target and the projectile feature knowledge: in particular, target composition, mass density and linear stopping power, as well as the beam energy distribution, result in a considerable spread in the beam effective range with respect to the predicted one. In general, the longitudinal beam straggling can be described by a Gaussian function (Vavilov 1957), leading to the expression of the relative straggling in equation 1.5:

$$\frac{\sigma_R}{R} = (M^{-\frac{1}{2}}) \phi \frac{E}{Mc^2} \quad (1.5)$$

The straggling is then all the more reduced as the ion mass increases.

In addition to the overall energy loss considered till here which shapes the beam in the longitudinal direction (range variations), MCS and nuclear interactions play an important role in the resulting beam and dose distribution structure. The MCS is determined by elastic electromagnetic interactions of the beam ions with the target nuclei, causing considerable deflections in the single ion trajectory which mainly affect the lateral beam profile causing a spread. Starting from the single scattering model by Rutherford (Rutherford 1911), and moving to the calculation of the statistical distribution function for the scattering angle at a certain penetration depth given by Bothe 1921, a complete theory allowing for the calculation of the scattering angle probability has been proposed by Molière (Molière 1948) (confirmed to provide good predictions thanks to a large set of proton beam spread data - see Gottschalk et al. 1993) and then simplified for analytic calculations towards a Gaussian approximation. The Gaussian standard deviation expression in equation 1.6 is given by the characteristics MCS angle (Highland 1975)

$$\sigma_\theta = \frac{14.1 \text{ MeV}}{\beta pc} Z_p \sqrt{\frac{L}{L_{\text{rad}}}} \left[1 + 0.038 \ln\left(\frac{L}{L_{\text{rad}}}\right) \right] \quad (1.6)$$

where L is the material thickness and L_{rad} is the radiation length (reported for common materials in Tsai 1974). Even if the Gaussian approach is not always accurate to describe the lateral beam spread, it allows to retrieve the main parameters contributing to this effect: in particular, heavier particles have more narrow lateral beam shape, and the scattering effect increases at increasing ion range (but is inversely proportional to the beam energy) and for high-Z materials. A measurement of the lateral beam spread in a water column for different beam energies (ranges) is reported in Pedroni et al. 2005.

In addition to the elastic electromagnetic interactions, primary ions impinging on a target also undergo non-elastic reactions with the target nuclei which may cause the disintegration of the projectile and the target nucleus or a partial fragmentation. In general, nuclear reactions induce modifications in the beam composition which must be taken into account for the delivered dose estimate, causing both modification in the longitudinal and lateral beam structure. Moreover, this kind of reactions leads to the production of secondary particles, such as secondary protons, neutrons, hydrogen and helium isotopes and other ions (mainly with heavy ion irradiation), gammas.

The nuclear interactions occurring between projectile ions and target nuclei are described by a two-step process generally known as abrasion-ablation model (Hüfner et al. 1975; Serber 1947), depicted in Figure 1.3.

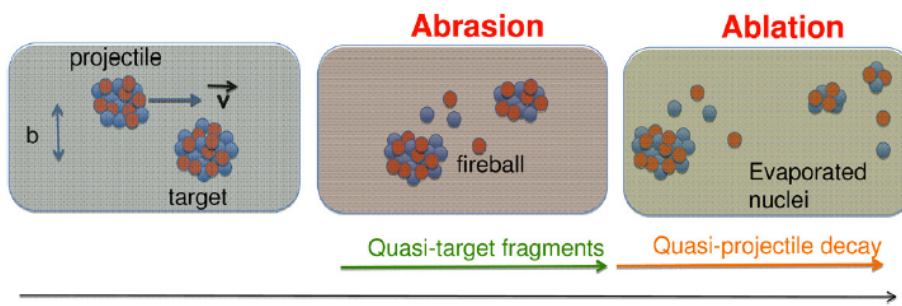
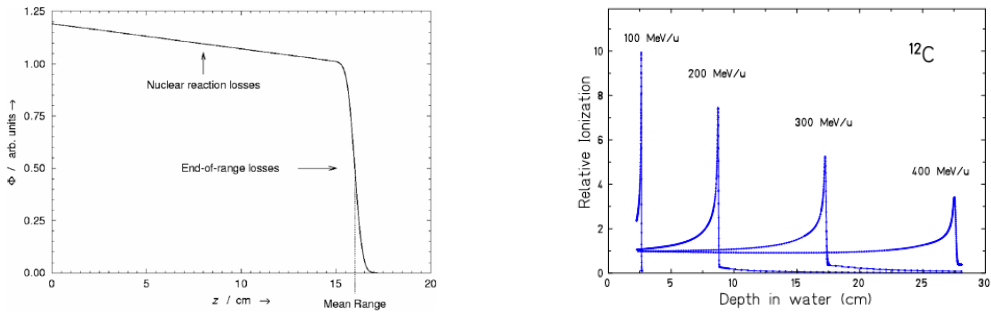


Figure 1.3: Schematic view of the abrasion-ablation model for the description of ion-nucleus interactions (in Durante et al. 2016): b is the distance between projectile center and target nucleus center, v is the projectile velocity.

Depending on the distance between projectile and target centers, named b , a variable number of nucleons is involved in the interaction and composes the reaction zone generally defined “fireball”. This nucleons are abraded in the first interaction step, while the “spectator” nucleons are almost not affected. During the second step, the fireball de-excites in an evaporation process. With increasing penetration depth, the increased number of nuclear reactions causes a growing loss of primary particles with the consequent production of lower-Z fragments. It is clear that peripheral collisions (high b) lead to smaller loss of primaries with respect to



- (a) Primary particle fluence loss in a proton beam as a function of the depth in water (in Newhauser et al. 2015).
 (b) Measured relative ionizations for carbon ion beams stopping in water (in Schardt et al. 2008).

Figure 1.4: Effects of nuclear interactions on the primary beam and resulting dose distribution.

central collision (small b), where projectile and target are most likely completely destroyed. Figure 1.4a shows the primary particle fluence loss in a proton beam as a function of the depth in water (Newhauser et al. 2015). In the entrance region before the falloff the fluence loss is caused by nuclear reaction, while close to the Bragg peak the fluence falloff is mainly due to absorption of primary particles which limited residual energy. In addition, the range straggling effect is visible. Concerning carbon ion beams, as reported in Durante et al. 2016, during a standard treatment only 50% of the primary ions reaches the Bragg peak region, while the others are undergoing fragmentation processes.

The projectile velocity determines the velocity of the secondary fragments, which can travel with longer ranges with respect to the primaries due to their reduced mass: this produces a tail in the dose distribution (for ions heavier than protons). The features of this tail have been deeply studied for different primary ions species (^{10}B , ^{12}C , ^{14}N , ^{16}O , ^{20}Ne), and shell-structure effects have been verified with a non-direct relationship between proton number Z and tails extension (Schall et al. 1996). Figure 1.4b shows the effects of nuclear reactions on the Bragg curves related to carbon ion beams at different energies stopping in water, measured in a water column (Schardt et al. 2008). With increasing primary energy and, consequently, beam penetration depth, the ratio between Bragg peak and entrance plateau dose is reduced by the decreased number of primary ions, while the tail after the Bragg peak is wider due to the increased number of lower- Z fragments traveling with longer range. In addition to this, the energy loss stochastic fluctuations is clearly visible in the broadening of the Bragg peak.

Further, interesting results about ion fragmentation in nuclear interactions can be found in Gunzert-Marx et al. 2008; Haettner et al. 2013, 2006; Matsufuji et al. 2003; Wroe et al. n.d.

Detailed information about fragmentation can be retrieved via Monte Carlo simulations and used to evaluate the impact on the delivered dose. As an example, simulations published in (Grassberger et al. 2011) of 160 MeV protons in water allowed to estimate the dose contributions given by primary particles (between 90% and more than 99% of the total depending on the range), with the remaining fraction of dose mainly connected to secondary protons and α particles: negligible dose is given by heavier fragments. A more intense dose contribution

from heavier fragments is expected for carbon ion irradiation, but an accurate Monte Carlo simulation of these processes is still a challenge.

As mentioned, in addition to charged fragments, nuclear interactions also produce gammas, mainly originating from atomic de-excitation processes (prompt-gammas) or from the annihilation of positron emitted by beta-emitter fragments (^{10}C , ^{11}C , ^{13}N , ^{14}O , ^{15}O), and neutrons. All the secondary particles which can be absorbed by the target contribute to the total dispensed dose to the target, while the others (except neutrons), escaping the target volume, can be exploited for non-invasive measurements of beam and target features. In particular, different techniques have been proposed and tested to measure secondary protons and gamma rays (both prompt-gammas and positron-annihilation gammas) with the aim of retrieving information about the ion range and obtain an online treatment verification. A detailed discussion about this topic will be given in section 1.1.8.

Focusing on neutrons, which are produced in large quantities and over a wide energy range, they must be modeled with care in order to evaluate the safety measures to be implemented in treatment centers (Newhauser et al. 2002), as well as the implications in the delivered dose and secondary cancer probability (Newhauser et al. 2011). The dose contribution caused by secondary neutrons strongly depends on the beam delivery system (see section 1.1.2 for the description of the beam delivery systems), as demonstrated in Gottschalk 2006. In particular, passive elements used for beam shaping have been identified as one of the main source of secondary neutrons contributing to the total delivered dose to the patient (Yan et al. 2002), so that in modern facilities deflecting elements are set after the passive modules in order to limit the neutron flux towards the target. It is interesting to notice that the amount of produced neutrons and resulting dose is compatible for protons and carbon ion irradiation, even if the neutron yield is higher for carbon ions: this is due to the different beam intensities used in clinics for the two species, with more than a factor 20 in favour of protons. Finally, if compared to photon standard radiotherapy, the neutron dose associated to ion beam therapy treatments results to be smaller, as demonstrated in recent studies (Schneider et al. 2015).

1.1.2 Accelerators and beam delivery

The goal of ion beam therapy is to treat deep-seated tumors with a conform dose distribution. Different ion species, hadrons and charged particles in general have been and are under study for the clinical application (neutrons, charged pions, antiprotons, helium ions - i.e. alpha particles -, heavier ions like lithium, oxygen, up to silicon ions), but only two are at present implemented for the patient treatments: protons and fully stripped carbon ions (Degiovanni et al. 2015). The ability of treating any kind of tumor at any depth in human body relies on the possibility of providing the employed particles enough energy to obtain a range of about 25 cm in soft tissues. This need translates into maximum energy values of the order of 200-250 MeV and 4500 MeV (i.e. 375 MeV/u) for protons and carbon ions, respectively (Braccini 2010). In order to achieve the desired ion energy, sizable accelerators are needed and different solutions have been explored; at present, cyclotrons and synchrotrons are clinically implemented and available on the market. In the following, after a brief historical introduction, we sketch the main characteristics of the accelerators used in clinics, and we highlight the main features which are reflected in the treatment delivery. In addition to this, the beam delivery systems are described following their chronological development since the first ion

beam therapy treatments. The final part of this section is dedicated to an overview of the main directions followed for the future acceleration and beam delivery techniques upgrade.

The way towards the possible application of ion beams in therapy (proposed only later by Wilson - see R. R. Wilson 1946) was opened by the invention of the cyclotron by Ernest Orlando Lawrence in 1929 (Lawrence et al. 1932), which added a magnetic field to the recently proposed linear accelerator (Wideroe 1928). A cyclotron is composed of two hollow electrodes with a frequency-alternating voltage applied between them, which accelerates the charged particles at each revolution. The circular trajectory is obtained thanks to a fixed vertical magnetic field. Nuclear physics saw a paramount development thanks to this invention, but also in the medical field the impact was remarkable. Already in 1935, Lawrence produced the first cyclotron-originated radionuclides, then used for radiotracing, diagnosis and treatment. The first cyclotron-based treatment was performed with fast neutrons (i.e. with kinetic energies between a few MeV and a few tens of MeV) in 1938, following a paper by Gordon Locher who underlined the therapeutic potentialities of neutrons (Locher 1936); the neutrons were produced by bombarding a beryllium target with cyclotron-accelerated deuterons (Stone et al. 1940). The unfavorable depth-dose distribution of neutrons and the difficulties linked to their collimation finally led to abandon the neutron treatments in 1948 (Stone 1948) and move towards proton-beam treatments in the 50's: neutrons were revised in 1965 by Catterall in London (Catterall et al. 1971) and are still used today in BNCT techniques (Barth et al. 2005; Nedunchezhian et al. 2016). As already mentioned in section 1.1, the first proton therapy treatment was conducted by Cornelius Tobias, and John Lawrence with the Lawrence cyclotron in 1954 (Tobias et al. 1958, 1955). Between 1954 and 1974, more than 100 patients were treated in Berkeley with cyclotron-accelerated protons. In parallel, in 1957 the first tumor was irradiated with protons at the Uppsala cyclotron in Sweden (Larsson 1962), and an intensive proton therapy program, leaded by Robert Wilson, was started in Harvard with a new-built cyclotron (R. Wilson 2004). Following these first experiences, new physics laboratories decided to set up proton beams for therapy (USSR, Japan, Switzerland), until the creation of the first hospital-based center, built at the Loma Linda University Medical Center in California, which started operating in 1990. This historical overview shows how the cyclotron technology has soon spread all over the world, not only in research centers, but also for therapy purpose. The present cyclotron machines, which are now commercially available by different providers, still rely on the same accelerating principle as the first Lawrence system, but the technology has greatly advanced. In particular, the vertical magnetic fields in charge of bending the particles on a spiral trajectory has been improved, giving the beam the desired transverse compactness. Moreover, the beam extraction efficiency has been improved, and multiple extractions are now possible to supply different transport lines.

In addition to cyclotrons, other accelerating machines initially developed for fundamental research have been translated to medical applications and are nowadays knowing a large diffusion: the synchrotrons. While the cyclotron present a fixed-value magnetic field, so that the radius of the beam trajectory increases during the acceleration process, in the synchrotron the trajectory radius is kept constant thanks to the variation of the bending magnetic field. The boost is provided by radio-frequency cavities, based on the same principle as the one composing linear accelerators: the radio-frequency increases to follow the particle revolution speed, and this acceleration principle allows to overcome the cyclotron energy limitation, as well as to obtain beam at different energies by tuning the extraction process. The invention is based on the independent ideas of Vladimir Veksler (Veksler 1944) and Edwin McMillan (McMillan 1945): the latter both coined the name of the machine in its letter, and constructed the first

electron synchrotron in 1945 in Berkeley. Some years later, the first proton synchrotron was designed in 1952 by Sir Marcus Oliphant, which already published a preliminary sketch of the machine in 1943 (Oliphant 1943).

1.1.3 Biological effects of ion beam therapy

In addition to the already presented physical differences between photon radiation therapy and ion beam therapy treatments, a fundamental aspect of the game lies in the biological effect of such radiations. In the following, the main biological implications of radiation therapy are summarized with the aim of highlighting the favorable contribution given by charged particles with respect to photons and, at the same time, discuss some controversial points (Paganetti et al. 2013).

Absorbed dose, defined in ICRU 1980, 1998 as

$$D = \frac{d\bar{\epsilon}}{dm} \quad (1.7)$$

where $d\bar{\epsilon}$ is the mean energy imparted by ionizing radiation to matter of mass dm . To be precise, the imparted energy must also be defined: in the same ICRU reports we find that

$$\epsilon = R_{\text{in}} - R_{\text{out}} + \sum Q \quad (1.8)$$

with R_{in} and R_{out} the sum of the energies of all ionizing particles entering or leaving the volume, respectively, $\sum Q$ the sum of all changes of the rest mass energy of nuclei and elementary particles in any nuclear transformations occurred in the volume due to the ionizing radiation.

LET TO BE DEFINED: number of ionizations which radiation causes per unit distance as it traverses the target.

In order to transfer the experience from photon data to ion irradiation and to create a common evaluation parameter, the RBE has been introduced and defined as the ratio between the photon and ion equivalent dose:

$$\text{RBE} = \frac{D_{\text{photon}}}{D_{\text{ion}}} \quad (1.9)$$

where D_{photon} and D_{ion} are the absorbed dose for photon and ion irradiation causing the same biological effect. Notwithstanding the apparently simple definition, RBE results to be a very complex quantity, but for the moment the only one really used in clinics: it depends on the particle type, energy, on the biological target, as well as on dose and LET.

1.1.4 Treatment planning

1.1.5 Advantages and drawbacks with respect to standard radiotherapy

1.1.6 Quality assurance in ion beam therapy

1.1.7 Ion range verification

1.1.8 Secondary radiation techniques

1.1.8.1 Positron Emission Tomography

PET is at present the only method clinically implemented for ion range verification (Bauer et al. 2013; Enghardt et al. 2004; Hishikawa et al. 2002; Parodi et al. 2007). PET techniques are based on the detection of the two back-to-back 511 keV photons produced by the annihilation of positrons (created by the emitter fragments of nuclear reactions) with patient electrons, resulting in a delayed radiation which should be detected with time coincidences, allowing for an intrinsic background reduction. Nevertheless, the monitoring with positron emitters secondary signal must deal with a limited count rate compared to medical imaging PET, with the lifetime of emitters providing a delayed information that implies the signal integration over a whole treatment fraction (not a single spot or group of spots), with physiological washout effects depending on the emitters lifetime.

Even if the only available and functional range monitoring system in a clinical center is based on this technique (Enghardt et al. 2004), several clinical experience with commercial or adapted PET system already shown intrinsic limitations mainly connected to the ring geometry (not directly applicable to the treatment monitoring due to the presence of the beam) or in general to geometrical constraints limiting the field of view and the resulting system global efficiency and spatial accuracy (the limited detection angle generates artifacts in the final image) (Parodi 2016). The research is ongoing and new results are expected for the next years thanks to the introductions of new systems with adapted geometries, to the improvements in acquisition and reconstruction techniques and to the clinical introduction of time-of-flight systems, intrinsically able to improve the detector spatial resolution via interaction time information, and depth-of-interaction reconstruction, which will allow for a more precise spatial reconstruction for reduced angular artifacts effects.

1.1.9 Prompt-gammas: physics and features

1.1.10 State of the art of range verification

1.2 Nuclear medicine

1.2.1 PET and SPECT

1.2.2 State of the art of PET and SPECT

2

Prompt gamma detection and imaging

Contents

2.1 Photons	18
2.1.1 Photon interactions in matter	18
2.1.2 Photon detection	18
2.2 Prompt gammas	18
2.2.1 Ion range monitoring with prompt gamma radiation	18
2.3 Gamma cameras	18
2.3.1 Applications in medicine	18
2.3.2 Ion beam range monitoring	18
2.3.3 Nuclear medicine	18
2.4 Gamma cameras state of the art	18

2.1 Photons

2.1.1 Photon interactions in matter

$$h\nu' = \frac{h\nu}{1 + \frac{h\nu}{m_0c^2}(1 - \cos(\theta))} \quad (2.1)$$

2.1.2 Photon detection

2.2 Prompt gammas

2.2.1 Ion range monitoring with prompt gamma radiation

2.3 Gamma cameras

2.3.1 Applications in medicine

2.3.2 Ion beam range monitoring

2.3.3 Nuclear medicine

LINE CONE RECONSTRUCTION (Cree et al. 1994), (Basko et al. 1998), (Parra 2000), (Hirashawa et al. 2003), (Maxim et al. 2009)

ITERATIVE RECONSTRUCTION (Schöne et al. 2010), (Zoglauer et al. 2011), (Gillam et al. 2011), (Lojacono et al. 2013), (Mackin et al. 2012)

2.4 Gamma cameras state of the art

3

CLaRyS prototypes

The characterization method and the results presented in section 3.2.2 of this chapter have been submitted for publication on JINST.

Contents

3.1 CLaRyS gamma camera components	20
3.1.1 Scatterer	21
3.1.2 Collimator	25
3.1.3 Absorber	26
3.1.4 Beam tagging hodoscope	31
3.1.5 Camera acquisition system	36
3.1.6 Camera acquisition, monitoring and slow control software	37
3.1.7 Camera integration and mechanical support	40
3.1.8 Data analysis and image reconstruction	41
3.2 Camera component characterization and development status	44
3.2.1 Scatterer silicon layer characterization	44
3.2.2 Absorber BGO blocks characterization	46
3.2.3 Hodoscope PMs characterization	62
3.2.4 Hodoscope fiber test with electron source	67
3.3 Summary and perspectives	70
3.3.1 Silicon scatterer	71
3.3.2 BGO absorber	72
3.3.3 Scintillating fiber hodoscope	73
3.3.4 Acquisition and software	74
3.4 Conclusion	75

Following the highlighted limits of ion beam therapy (see chapter 1), a collaboration of five French research institutions was established in 2010 with the aim of exploring different experimental solutions for the ion range online monitoring. The research group originally involved the “IPNL”, the “CPPM”, the “LPSC” in Grenoble, the “LPC” and the “CREATIS” in Lyon. The collaboration focuses on the investigation of methods and detection solution for the online monitoring of ion beam range during ion beam therapy treatment, and is so called CLaRyS.

The main goal of the created collaboration is the parallel development of three gamma detection systems to be employed for ion range online monitoring purpose in the ion beam therapy field: a PET detector called DPGA, a multi-collimated gamma camera and a Compton camera.

The design and development of the PET system is managed by the LPC group, which left the collaboration in 2017, and this detection system is not treated in this thesis work.

In this chapter the two gamma cameras (multi-collimated and Compton) prototypes are described in details, and the present status of the instrumental development is presented. In the following, an entire chapter (chapter 6) is dedicated to the tests of the detectors performed on ion beams.

3.1 CLaRyS gamma camera components

The two gamma cameras under development by the CLaRyS collaboration are devoted to the detection of prompt-gamma rays emitted during ion beam treatments (see section ??). The design of the two cameras has been optimized by different Monte Carlo simulation studies for what concerns both the detector components and the geometrical setup.

As already mentioned, a Compton camera is usually composed of two detector sections, a scatterer and an absorber: the CLaRyS prototype respects the standard design. In the scatterer, described in section 3.1.1, the prompt-gamma incoming ray is deflected by Compton interaction and the interaction position and energy deposited are stored. The scattered photon reaches then the absorber section, where its energy is ideally totally deposited and stored, again with the interaction position. This configuration is used to provide what is usually defined as “electronic collimation”, but a mechanical collimation is still an option for photon detection and localization. The scatterer section can be replaced by a mechanical collimator, described in section 3.1.2, which selects the parallel incoming photons then absorbed by the same absorber detector (a geometrical setup adaptation is possible to optimize the detection performance and will be discussed in the following). The mechanically collimated system is called multi-collimated camera, due to the collimator multi-slit structure.

As underlined in section ??, the prompt-gamma measurements are affected by several sources of background: in particular, the signals detected by the two cameras can come from secondary particles other than prompt-gammas, like photons from positron annihilation, neutrons and protons (for beam of ions heavier than protons). One of the possible solution for background rejection is the use of TOF information (see section ??), requiring a further detection section dedicated to the beam tagging. A beam tagging hodoscope is being developed in parallel and

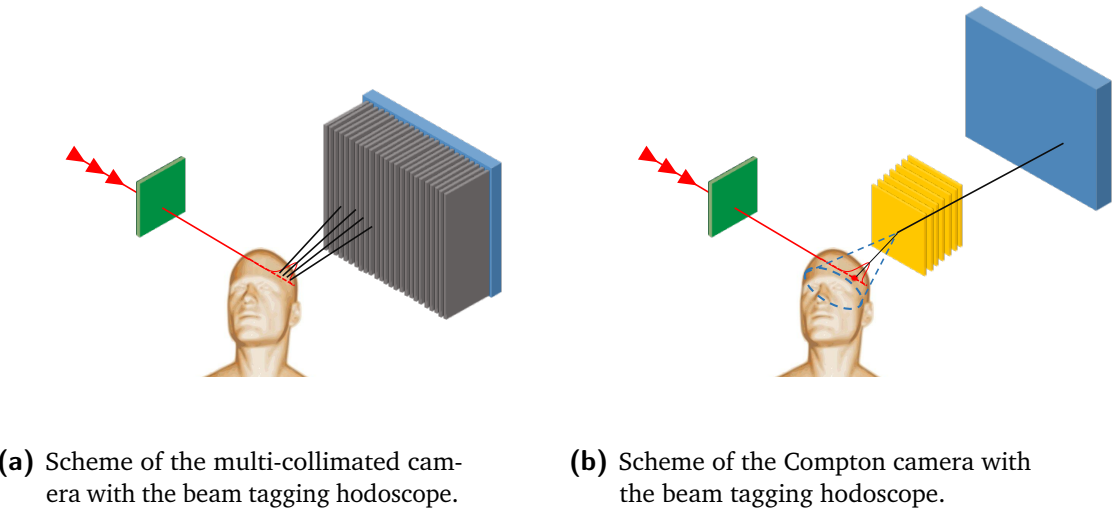


Figure 3.1: Schematic view of the two CLaRyS gamma camera prototypes: the multi-collimated camera (a) and the Compton camera (b), both coupled to the beam tagging hodoscope. The ion beam is represented by the red line, and some beam bunches have been highlighted. The detection principle is also sketched for the two detectors: the tungsten collimator select the parallel incoming photons for the multi-slit collimated camera (a), while the Compton cone is reconstructed with the two interactions in scatterer and absorber in the Compton camera (b).

can be coupled to both the gamma cameras for TOF measurements; its description is presented in section 3.1.4.

A schematic view of the two prototypes is given in Figure 3.1.

3.1.1 Scatterer

The scatterer stack is one of the components of the Compton camera prototype. Dedicated to the photon Compton scattering, its design has been studied to fulfill the camera requirements.

The Compton events reconstruction strongly relies on the measurement of the energy deposited by the photon in its Compton interaction, mandatory to properly calculate the Compton scattering angle, which is then the aperture of the resulting Compton cone. The camera accuracy is then strictly dependent on the scatterer energy resolution. At the same time, the camera efficiency is dominated by the balance between Compton interaction and photoelectric absorption probability in the scatterer detector.

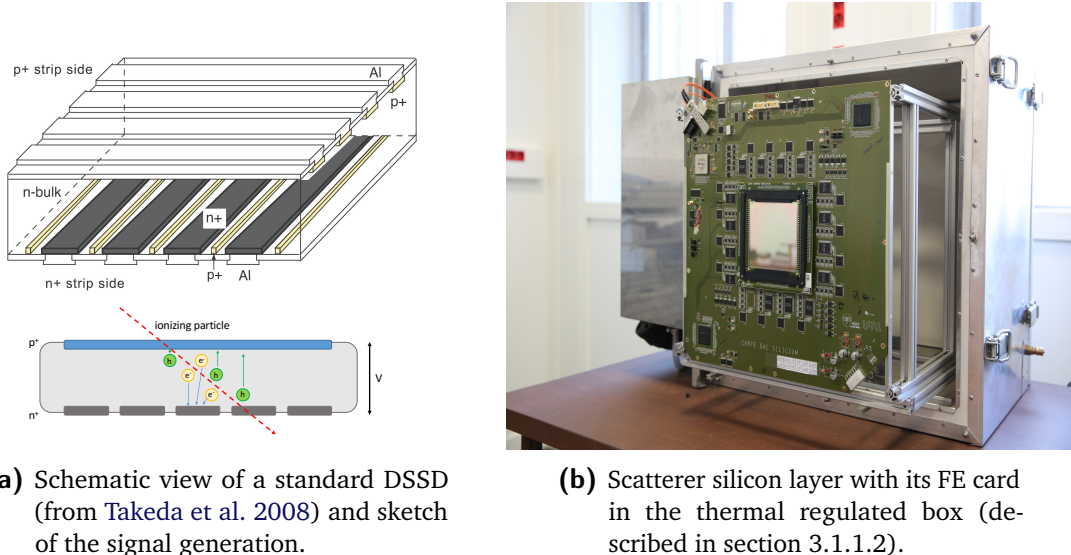
Given the need of at least two interactions for a proper event reconstruction (a Compton scattering in the scatterer section and an ideally complete absorption in the absorber section, described in 3.1.3), the material choice and the geometrical configuration play a fundamental role in the camera operation. The setup must be tuned in order to define the better trade-off between Compton and photoelectric interaction probability and to optimize, as mentioned, the detector energy resolution.

Given the fact that the Compton interaction probability linearly increases with the material atomic number (Z), while the photoelectric absorption depends on Z^n with n varying between 4 and 5 according to the photon primary energy (Knoll 2000), it is clear that a low Z material is preferred. Considering now the detector energy resolution, it must be noticed that the main parameter affecting the deposited energy detection is the so called “Doppler spread”. The Compton angle reconstruction formula in equation ?? neglects the initial recoil electron state, which is considered free or unbound. The Compton energy transfer continuum results affected by the binding energy of the electron, with a relatively increasing effects for decreasing incident photon energy. This effect adds uncertainty on the reconstructed deposited energy, and so in the Compton angle calculation. Given its direct dependence on the recoil electron binding energy, the “Doppler spread” is reduced for low Z materials. Following the described theoretical considerations, silicon detectors are the most coherent choice. This choice has been verified in simulation, where a silicon scatterer has been compared to competitor materials; the result are included in the Monte Carlo study presented in chapter 5.

Dedicated Monte Carlo simulation studies have been performed in order to define the most suitable geometrical configuration for the Compton camera, including the scatterer stack (Richard 2012). As a trade-off between detection efficiency and total cost, 10 layers were included in the original scatterer design. Concerning the layer size, about $10 \times 10 \text{ cm}^2$ of active area in the transverse plane have been identified as the most convenient choice, also considering the absorber size (see section 3.1.3) and the distances between the detection sections required by the TOF measurements and imposed by the detector rate acceptance in clinical conditions (see appendix A). Moving to the layer thickness, its choice is governed by the definition of the camera operation. The CLaRyS Compton camera does not aim to track the Compton recoil electron, which must be then absorbed inside the same scatterer layer where the Compton interaction took place. This requirement is necessary to well reconstruct the Compton interaction angle, which needs the whole transferred energy as parameter; in addition to this, a recoil electron escaping the involved detection layer can interact in a different layer causing false coincidences which affect the camera efficiency and imaging accuracy. In order to minimize the recoil electron escape probability, relatively thick detectors are needed.

The technological choice of the collaboration was oriented to silicon DSSDs, provided by the Norwegian company SINTEF. A schematic view of the detector principle is given in Figure 3.2a. The silicon crystal is doped with negative (n) and positive (p) charge carriers on the two opposite sides, creating diodes which are then reverse biased. A polarization voltage is applied to the two opposite sides of the crystal, and a depletion region with no free charges is created. A ionizing particle interacting in the depletion region generates electron-hole pairs in number proportional to the deposited energy. The generated charges drift towards anode (electrons) and cathode (holes) and are converted into electrical signals. The read-out is ensured by the implanted strips, which transfer the charges outside the detection region.

Each layer has an active volume of $96 \times 96 \times 2 \text{ mm}^3$, segmented with 64 strips per detection plane. The strip pitch is 1.41 mm, for a strip width of 1.31 mm. The applied polarization voltage is nominally -750 V, and it is uniformly shared on the whole surface to obtain a homogeneous depletion region. A guard ring, composed of 23 strips surrounding the read-out ones on the p side, ensures the desired voltage gradient. The more peripheral strip of the guard ring is connected to the high voltage, while the n side has a single strip for the guard ring,



(a) Schematic view of a standard DSSD (from Takeda et al. 2008) and sketch of the signal generation.

(b) Scatterer silicon layer with its FE card in the thermal regulated box (described in section 3.1.1.2).

Figure 3.2: Overview of the scatterer layers, with its working principle (a) and a picture of the detector connected to the FE card in the thermal regulated box (b).

connected to the ground. The p and n read-out strips are then connected to the FE electronics via bonding cables.

The FE electronics card has been developed by the IPNL electronics group and is described in details in section 3.1.1.1. The silicon detector is directly plugged on the card, and the mechanical support for the scatterer stack has been studied according to the card size, as shown in Figure 3.2b.

Among the 10 received DSSDs, only 7 fulfilled the requirements imposed by the Compton camera application, mainly in terms of noise level (leakage current); 3 layer have been rejected, so that the final prototype scatterer is composed of 7 silicon planes.

The 7 selected layers have been characterized with a temporary acquisition system in terms of leakage current at different temperatures. The results of these measurements can be found in Ley 2015. The measurements allowed to verify the producer specifications in terms of polarization voltage to be applied for a complete detector depletion, as well as to identify the noisy strips and create a complete characterization database. In addition to this, they highlighted the need to cool the detectors down with respect to the room temperature (25°C) in order to reduce the leakage current to acceptable levels, and so reducing the total noise level, affecting the detector performance. In order to accomplish the cooling task and respect, at the same time, the clinical restrictions, a thermal regulated box based on cold air pump has been designed and produced. It operates as the scatterer stack mechanical support, and it is described in section 3.1.1.2.

3.1.1.1 Scatterer Front-End card

As mentioned in the previous paragraph, the main requirement for the scatterer detector modules is a very good energy resolution. The desired working performance can be quantified as follows:

- 1 keV FWHM energy resolution;
- 1.41 mm spatial resolution (corresponding to the strip pitch);
- 15 ns FWHM time resolution.

The scatterer FE card has been developed by the IPNL electronics group in order to achieve this performance. It is composed of two well separated sections, analog and digital, which must be kept separated in the card layout in order to minimize the contribution of the digital noise on the treatment of the analog signals. Moreover, in order to reduce the electronic noise, the analog section must be placed as close as possible to the detector, to minimize the signal path length.

At first, a dedicated ASIC has been designed and developed to treat the signals directly coming from the DSSD ([Dahoumane et al. 2014](#)). Each ASIC processes 8 detectors channels, so that 8 ASIC per plane are required for the read-out of a complete silicon layer. This section represents the core of the analog stage. The ASIC has been designed and tested to achieve the desired performance in terms of ENC, which must be lower than 118 electrons RMS in order to obtain the 1 keV FWHM energy resolution, signal dynamics and accepted detection rate. The analog raw signal first passes through a CSA, which returns an analog amplified signal. This pulse can be further amplified with a SHS based on a CR-RC filter, which filters and shapes the signal in about 1 μ s, or via a fast amplifier (with 15 ns shaping time). The first mode is used for a refined charge (deposited energy) measurement and can be employed for detector tests and characterization, while the second is the standard working one which allows for fast energy and time measurements. The amplified signal finally passes through a discriminator, which gives a digital output. Analog (from CSA or SHS) and digital signals are then sent to the digital stage of the card for the measurement of time, position and energy.

The digital stage is mainly composed of one ADC module per ASIC and two FPGAs. The analog signal from the ASIC is processed by the ADC, which is a 12-bit module with 8 channels, with a sampling rate of 100 MSPS. Each ADC returns 16 LVDS pairs (2 per channel), which are sent to the FPGAs together with two clock signals (two LVDS pairs) and the 8 digital outputs of the ASIC. So, 44 input channels of the FPGA are used for the acquisition of 8 read-out channels (one ASIC). Two FPGAs Altera Cyclone III ([Altera 2012](#)) are installed on the card to handle the signals coming from the whole detector (128 channels, 64 per detection plane): both of them are equipped with a TDC for the time measurement.

A third FPGA (Altera StratixII GX ([Altera 2009](#))) is finally installed on the card to handle the processed data collection and the communication with the acquisition system, described in section 3.1.5, via a 3 Gbit/s link.

The ASIC has been developed in three versions, and the cards have been optimized during the

development process and produced in its final version (shown in Figure 3.3a) in the spring 2017. The 7 cards are now available and the development of the FPGA firmware is ongoing.

More details about the card layout, components and operating principle, as well as a description of the tests performed during the development can be found in [Chen 2017](#) and [Dahoumane et al. 2012](#).

3.1.1.2 Scatterer thermal regulated box

The results of the leakage current tests performed on the silicon detectors showed the need of cooling the detector down to achieve the required performance in terms of noise, which affects the spatial, time and energy resolutions. The leakage current has been studied in temperature cycles in the range -40 - +40 °C, and an overall consistent behavior has been observed both on N and P strips of the detector. The leakage current slightly increases in the range -40 - 0 °C, with values in the range 0 - 8 nA for the analyzed strips, and then drastically increases beyond 0 °C, with peaks of more than 80 nA at +40 °C. The complete description of the performed measurements and the detailed results can be found in [Ley 2015](#).

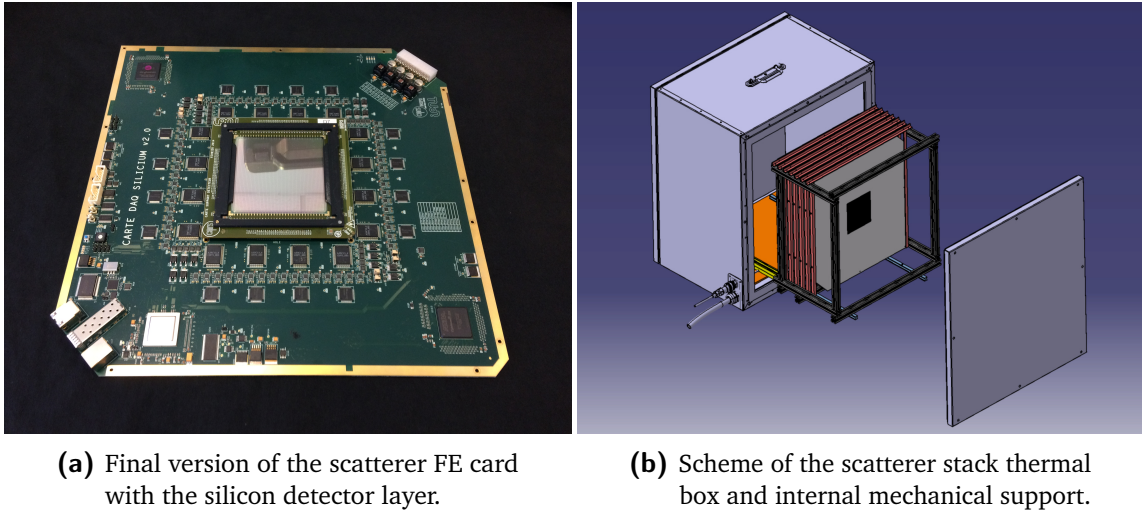
A cooling system is needed for the silicon detectors operations: it must be able to keep the temperature constant and below, at least, 0 °C, preferably around -20 °C where the leakage current is more stable in case of small temperature variations. The clinical environment limitations must be considered to design such a cooling system (portability, gas, noise level), as well as the material budget and the mechanical integration with the other camera components.

The implemented solution consists in the thermal regulated box shown in Figure 3.2b, together with one of the silicon layers. The size of the box is 490×490×300 mm³, and the structure is composed of 2 mm of aluminum and three insulation layers of 10 mm of silica aerogel Spaceloft® ([Aspen Aerogels 2011](#)), for an equivalent thickness of 2 mm of silicon (0.7% of interaction probability for 1 MeV photons). The cooling is performed via an electric air pump, which is able to keep the temperature inside the box at -20 °C with a 400 W heat evacuation power. The heat power produced by the 7 silicon FE cards in operation must be verified, but the estimate confirms the effectiveness of the thermal box nominal performance. Once card and detector will be fully operational, a test will be performed to check the temperature stability inside the box.

The FE cards and the silicon layers are fixed inside the box via a mechanical support designed and produced by the IPNL mechanics group. The support, which ensures a millimeter position accuracy, is fixed on metal rails which allow to easily handle each detector layer. A scheme of the thermal box and the internal support is shown in Figure 3.3b.

3.1.2 Collimator

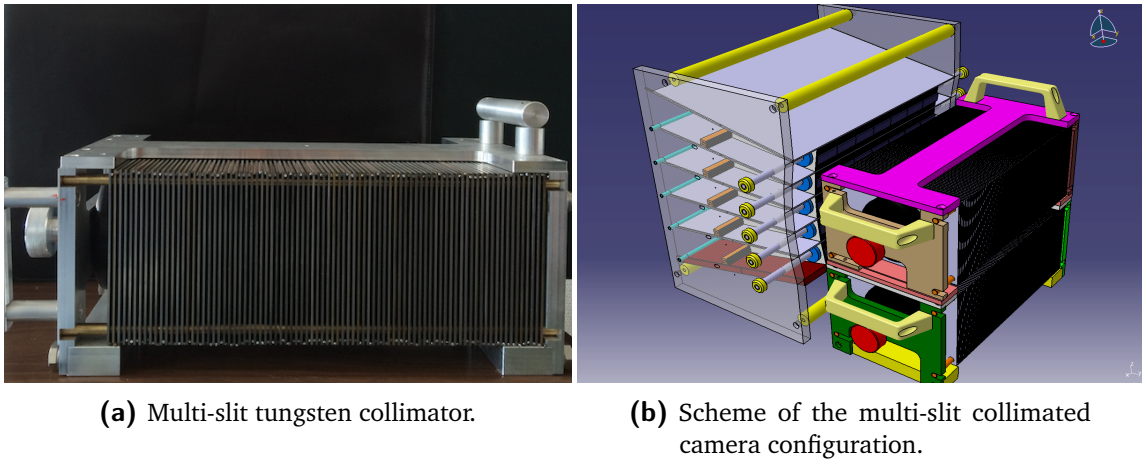
The multi-collimated camera is equipped with a multi-slit collimator, with tungsten slabs. Its design has been extensively studied in Monte Carlo simulations ([Pinto et al. 2014](#)), and it can be easily adapted to different geometrical configurations of the absorber detector and to various monitoring requirements. In particular, the distance between neighboring slabs can



(a) Final version of the scatterer FE card with the silicon detector layer.

(b) Scheme of the scatterer stack thermal box and internal mechanical support.

Figure 3.3: Scatterer silicon layers equipment: final version of the FE card (a) and scheme of the detector integration in the thermal regulated box (b).



(a) Multi-slit tungsten collimator.

(b) Scheme of the multi-slit collimated camera configuration.

Figure 3.4: Tungsten collimator and its setup in the multi-slit collimated camera. The two tungsten multi-slit collimators are placed in front of a 6×5 BGO block absorber setup in its mechanical support (see section 3.1.3).

be modified, as well as the number of total slabs, in order to find the best trade-off between detection efficiency and spatial resolution; this depends on the distance patient-collimator, on the required extension of the field of view and on the desired monitoring time. Two identical collimators of $30 \times 14 \times 17$ cm³ have been produced, in order to be able to set several absorber configurations in the transverse direction (extended version along the beam axis or in the perpendicular direction). In Figure 3.4a a picture of the tungsten collimator is presented, while in Figure 3.4b we show a schematic view of a possible multi-collimated camera configuration.

3.1.3 Absorber

The Compton and multi-collimated camera absorber was initially conceived as a very large surface plane composed of 96 BGO blocks recovered from a dismantled PET system HR+ by SIEMENS, documented in (Adam et al. 1997; Brix et al. 1997).

BGO is one of the most used scintillators for gamma detection applications, thanks to a fair energy resolution and a optimal gamma detection efficiency, given the high effective atomic number (75) and high density (7.12 g/cm^3) (Elftmann et al. 2015) which maximize the photoelectric effect. Moreover, the absence of internal radioactivity which characterizes other scintillator materials employed in the same field (i.e. LYSO, LSO), makes it suitable for low noise detectors, required by a Compton camera to reduce the amount of random coincidences, one of the main sources of background for the application in ion beam therapy monitoring (Ortega et al. 2015). As highlighted in (Hueso-González et al. 2015), LYSO and LSO show overall better performances with respect to BGO for what concerns energy, time and spatial resolution, due to an about 4 times higher light yield, but the gap is reduced for the detection of gamma rays in the prompt-gamma energy range (especially beyond 1 MeV). The limited cost of BGO with respect to LSO and the comparable performances in the prompt-gamma energy range make it an optimal solution for prompt-gamma camera prototypes.

Each BGO block composing the gamma camera absorber has a surface of $3.5 \times 3.8 \text{ cm}^2$, with a thickness of 3.0 cm. The mono-block BGO crystal is streaked in a 8×8 pseudo-pixel matrix; a reflecting material is inserted between the pseudo-pixels to improve the light collection and optimize the spatial information accuracy via pixel separation. The read-out is achieved via four PM tubes per block, composing a quartet, coupled to the block back surface. Thanks to the internal streaked structure of the block, the scintillation light is shared on the four PMs depending on the pseudo-pixel where the interaction takes place (in case of multiple interactions more than one pseudo-pixel can be involved). The streaks have a different thickness according to their position in the block: they fully cover the block thickness on the block borders and they progressively shorten towards the block center, with a mono-block structure in the central block section on the entrance face. The reconstruction of the position of interaction is done via Anger logic, i.e. with a center of gravity calculation.

The whole set of recovered blocks was supposed to undergo a “reconditioning” process, including the PM removal, the crystal back surface polishing with diamond-based abrasive tool, the single PMs gain characterization and grouping in quartets with similar gains, the final re-coupling of the PMs and block shielding.

A set of “reconditioned” blocks have been tested with the method described in section 3.2 and their performance have been compared to a set of original blocks. An overall degradation of the detection performance has been verified on all the tested “reconditioned” blocks, which showed lower amplitude output signals probably link to a reduction of the collected scintillation light. Various correction methods have been tested, with unsatisfactory results. According to the outcome of these tests, summarized in Sandjong et al. 2017, the collaboration finally opted to adapt the camera design for the use of original, “non-reconditioned” BGO blocks.

Thirty original blocks are now available to compose the absorber detector. In addition to the already presented features, it must be noticed that the lateral surfaces of the original blocks, as well as the half of the PM length, are covered with a reflecting material which ensures the complete collection of the scintillation light. This is probably a component which was not well reproduced during the reconditioning process. The whole structure is then protected by a 1 mm thick aluminum foil, which also isolates from external light contamination.

Figure 3.5a shows one BGO block before the coupling to the PM quartet: the streaked structure is clearly visible, as well as the white reflecting material separating the pseudo-pixels and the

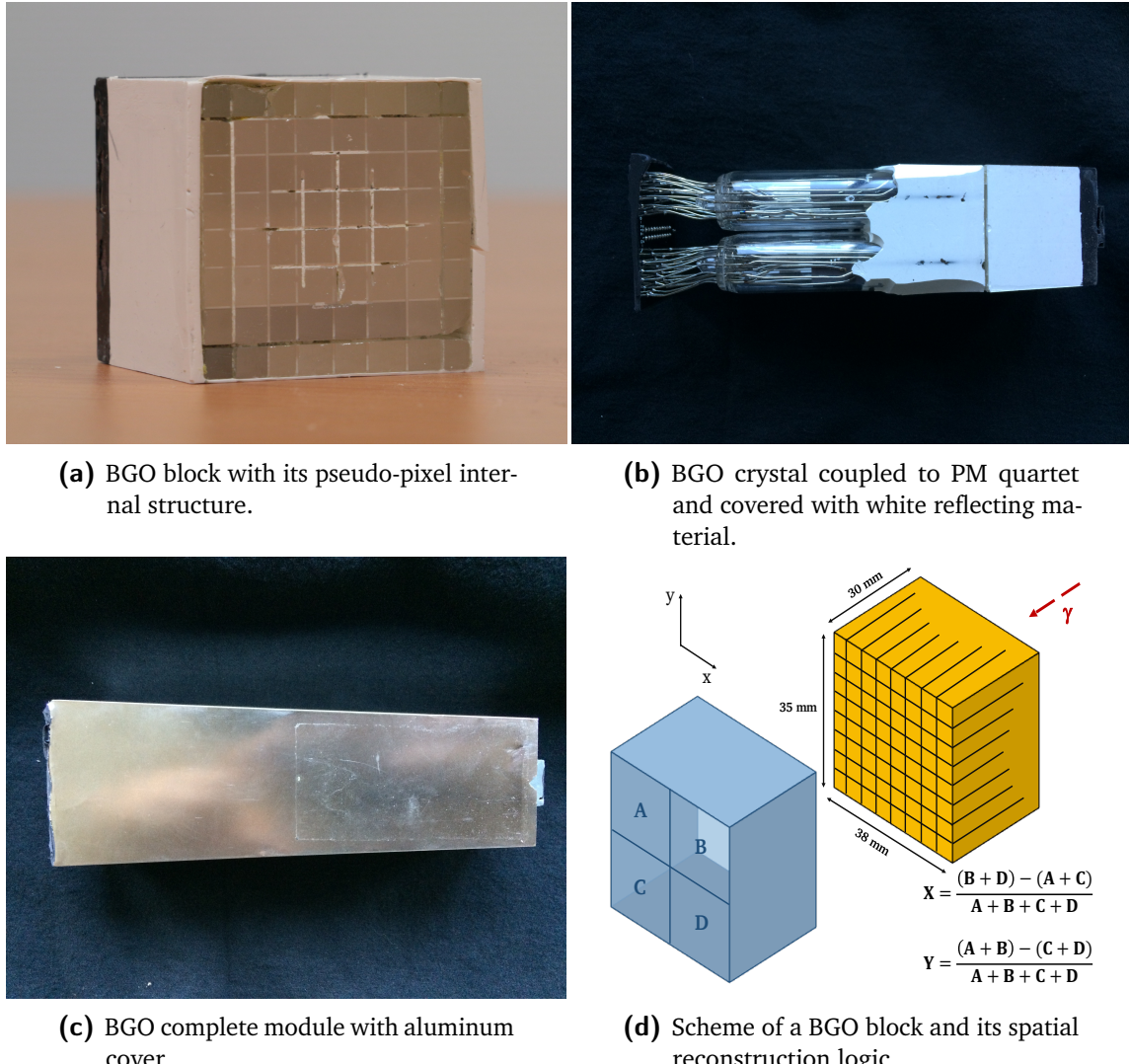
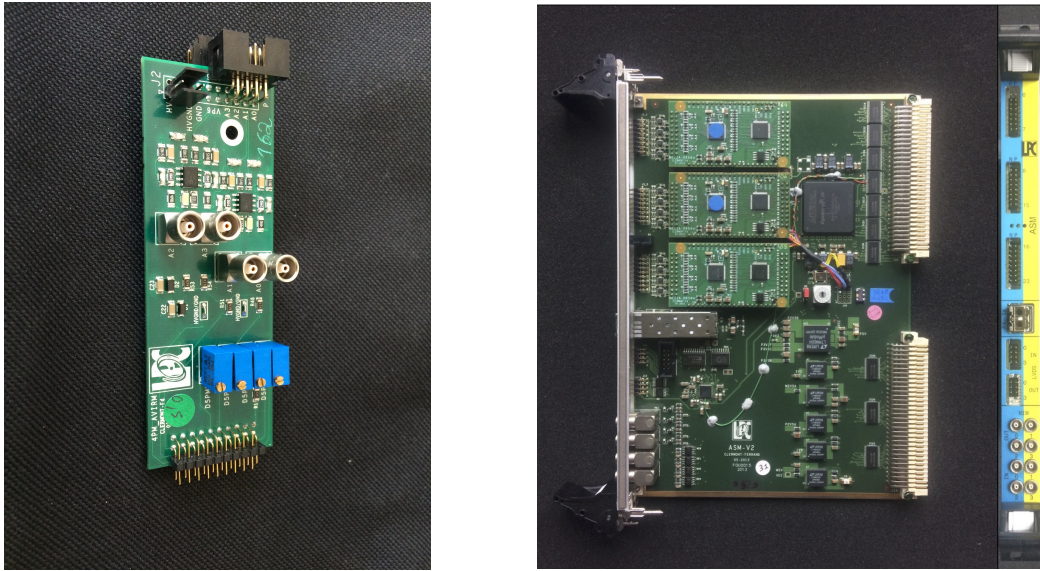


Figure 3.5: Components of an absorber module and its working principle.

one surrounding the block lateral sides. As mentioned, the same material also covers part of the photo-multiplier tubes, as shown in picture 3.5b, where the four PMs are glued to the block back surface. The described aluminum cover is visible in Figure 3.5c, while in Figure 3.5d a scheme of a block together with the related PM quartet is given. The spatial reconstruction logic is also reported in the same figure. To be noticed that the streaked structure of the pseudo-pixels depends on their position in the block: the reflecting streak covers about three fourth of the block thickness for the for the lateral pseudo-pixels, while it is limited to half of the block thickness for the central ones.

3.1.3.1 Absorber Front-End and read-out cards

A custom front-end card has been designed and produced by the LPC research group AVIRM and is used for the read-out of each BGO block. The card is equipped with four voltage modulators which divide the provided high voltage on the four PM tubes. The voltage sent



(a) FE card of the absorber BGO detectors.
4 analog outputs have been added for test purpose.

(b) ASM board of the absorber BGO detectors. Each board performs the read-out of 6 blocks.

Figure 3.6: Absorber read-out electronics: FE card (a) and ASM board (b).

to each PM can be tuned via screw-potentiometers on these modules. A ± 5 V low voltage is applied to the cards as supply for the differential amplifier modules, one per PM. Differential output channels are used to send the PM signals to the read-out card, called ASM board, via flat cables. A picture of the FE card is given in Figure 3.6a. To be noticed that four analog output channels have been added on some cards in order to allow laboratory tests with a signal treatment based on standard electronics modules, as described in section 3.2. These outputs retrieve the signal before the differential amplification stage, so that the low voltage supply is not needed for this read-out configuration.

The PM signals amplified by the FE card (differential outputs) are received by the ASM boards. Developed by the LPC AVIRM group, it is based on the VME standard and designed for the application in the DPGA PET system, equipped with LYSO mono-crystals, grouped in quartets and read-out by the same FE card described above. The adaptation to the gamma camera application, so that for the BGO modules signal treatment, involves only the firmware part, while the design of the board is unchanged. Each board has 24 differential inputs and it is so able to read the signals from 6 BGO blocks; a total of 5 boards are then needed for the complete read-out of the gamma camera absorber (30 blocks). The incoming signals are treated by three intermediate cards equipped with a DRS4 chip (Ritt 2009), designed and developed at the PSI, with 8 sampling channels at a maximum frequency of 5 GSPS (200 ps) for 1024 samples, and an ADC 12 bit-20 MHz module. The sampling frequency of the DRS4 can be modified to fit with the specific application: in particular, the BGO blocks produce wider signals with respect to the LYSO crystals of the DPGA. A FPGA Altera Cyclone IV GX (Altera 2015) receives and handles the digital outputs of the three intermediate cards and is in charge of sending the data to the acquisition system via a 3 Gbit/s optical link. The FPGA also governs the generation of the pre-trigger signal which is sent to an auxiliary board called THOR in order to start the acquisition of the gamma cameras, as detailed in section 3.1.5.

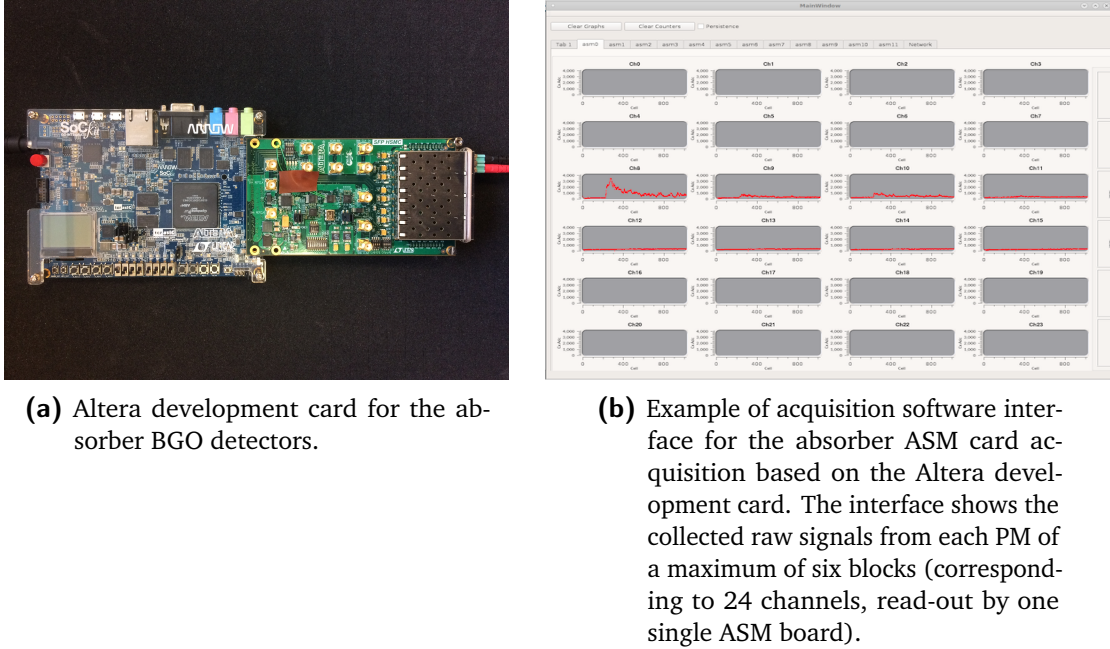


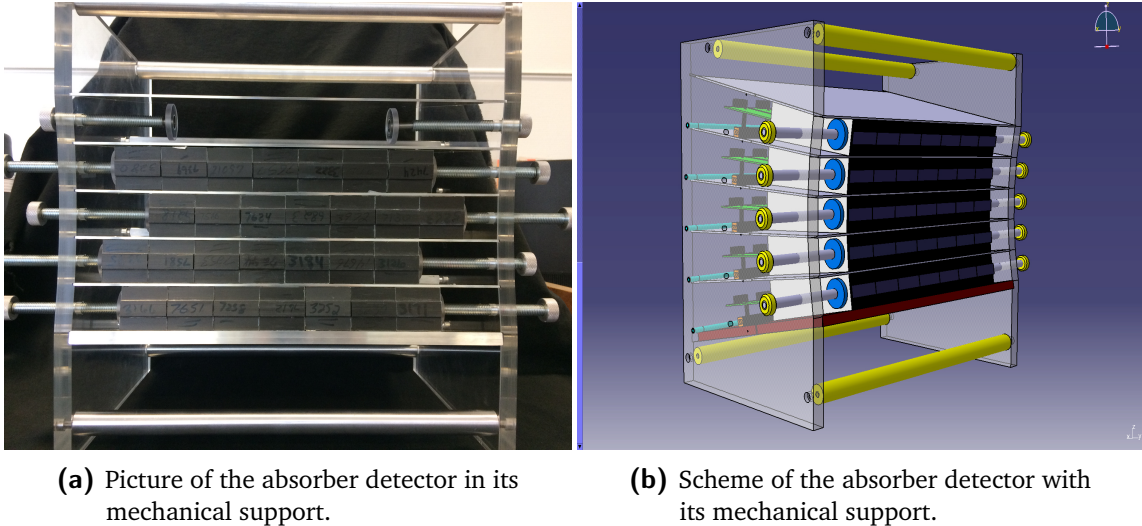
Figure 3.7: Details of the temporary absorber acquisition based on the Altera development card.

Absorber acquisition with development card

During the development of the final camera acquisition system based on the μ -TCA equipment, which required a dedicated firmware development ad testing process, a temporary acquisition system has been set for the absorber BGO blocks, mainly dedicated to the test and characterization of the ASM boards. It is based on a development commercial electronics card, provided by Terasic (Altera University Program), equipped with an FPGA Altera Cyclone V ([Terasic 2015](#)). The card FPGA can be programmed for the needed tasks, and it is directly connected to an acquisition PC via Ethernet cable. Three HSMC connectors allows for the connection to an expansion board SFP-HSMC ([Terasic 2009](#)), again by Terasic (Altera University Program), provided with a second FPGA and with optical fiber input/output connectors for the interface to the ASM boards. A single optical input is configured for this acquisition setup, with the firmware developed by the AVIRM group in LPC and adapted at the IPNL; one single ASM card can be connected to the board, so that a maximum of 6 BGO block can be read-out at the same time. A picture of the development card connected to the mezzanine is given in Figure 3.7a. Figure 3.7b shows an example of the user interface and data visualization of the C++ based acquisition software developed and provided by the AVIRM group.

3.1.3.2 Absorber mechanical support

A first mechanical structure for the absorber detector was initially conceived by the LPC group in order to hold up to 100 modules, foreseen by the original camera design. The reduction of the number of available blocks caused by the “reconditioning” process failure make necessary an adaptation of such a support. The new design has been carried out by the mechanics group of the IPNL in order to be compact and flexible in terms of detection modules setup. Figure 3.8 displays both a picture and a scheme of the absorber configuration with its mechanical support. The two lateral sides are built with PMMA boards connected by metal bars, and the BGO blocks



(a) Picture of the absorber detector in its mechanical support.

(b) Scheme of the absorber detector with its mechanical support.

Figure 3.8: Absorber front view with the BGO block lines arranged in the mechanical support (a). Scheme of the BGO absorber with its mechanical support (b).

can be arranged in up to 5 rows of variable size, ranging from 3 to 7 blocks. Each block row is supported by a thin metal foil, designed to reduce at minimum the blocks separation and to respect the original ring geometry deriving from the SIEMENS PET system. The blocks composing a row are then laterally pressed via two screws on the two sides of the structure, which can also be used to adapt the rows relative position horizontally. On the back side, a metal bar is added to avoid undesired movements, and the FE cards are fixed with plastic pillars. The realized support results to be versatile, compact and adapted to the prototype tests for both the Compton camera (where a squared setup is preferred) and the multi-collimated one (where the collimator geometry must be fit by the absorber geometrical configuration).

3.1.4 Beam tagging hodoscope

A beam tagging hodoscope is being developed in parallel to the two gamma cameras, mainly for background rejection and reconstruction optimization purposes [CIT]. As already mentioned, the detection of prompt-gammas (with mechanical or “electronic” collimation), is affected by the presence of other secondary particles produced during the ion beam irradiation, mainly neutrons. This background source can be efficiently identified and removed by applying TOF selection windows to the data acquisition. The TOF measurements can be performed using the accelerator radio-frequency signal as reference, but a direct beam detection results to be more accurate. An auxiliary detector is then needed before the beam interaction in the patient.

The CLaRyS hodoscope prototype is designed to provide space and time information about the incoming primary beam, particle by particle or bunch by bunch, depending on the beam intensity and detector efficiency and rate acceptance which must be characterized. In addition to the already explained use of the time information, a space primary particle tagging can be used to improve the reconstruction accuracy and constraint the possible reconstructed emission vertex in case of analytic reconstruction approach for both the multi-collimated and Compton cameras (see chapter 2).

The detector under development is based on squared 1 mm^2 polystyrene scintillating fibers BCF-12, 140 mm in length, provided by Saint Gobain ([Saint Gobain 2017](#)). A picture of the hodoscope on its mechanical support (detailed in the following) is presented in Figure 3.9. The fibers are arranged into two perpendicular planes for a two-dimensional spatial information: each plane is composed of 128 fibers, for a total active area (for 2D measurements in coincidence) of $128 \times 128 \text{ mm}^2$. The active detector surface is completely covered with black reflective tape, which shields from external light. The scintillation light produced in the fibers by an ionizing particle depositing energy is transported to the read-out system via FORETEC optical fibers (1.55 cm diameter, 1 m length), which are connected to the scintillating fibers thanks to a custom mechanical support and to a proper gluing process (see Figure 3.10a). Each scintillating fiber is read-out on both sides to optimize the detector efficiency and improve the time resolution which is not depending on the interaction position along the fiber with this configuration, so that the total number of read-out channels is 512. The signal read-out is ensured by 8 multi-anode PMs Hamamatsu H8500 ([Hamamatsu 2006](#)) shown in Figure 3.10c. The optical fibers are connected to the PM anode surfaces through a plastic custom mask, shown in Figure 3.10d. The PMs are equipped with custom black boxes which operate as mechanical support and external light protection (see Figure 3.10a). In order to provide further light isolation, the whole PM boxes are covered with black tape.

The optical fibers are connected to the PMs with the aim of increasing the maximum counting rate. 4 PMs are dedicated to the read-out of the horizontal fibers, and 4 to the vertical ones, and the neighboring fibers are connected to different PMs. An active area of $4 \times 4 \text{ mm}^2$ on the two planes is then read-out by all the 8 PMs. Moreover, the two sides of the same scintillating fiber are connected on the same PM. This fiber connection logic also improves the detector robustness; in case of problem on one PM, only 1 mm each 4 mm is lost on a single plane, so that the detection of the beam is still possible on the whole active area.

Each PM is connected to a single custom FE card. The hodoscope FE cards have been developed by the IPNL electronics group: their design is described in section 3.1.4.1. 8 FE cards are then used for the read-out, and the collected data are sent to the acquisition system described in section 3.1.5.

3.1.4.1 Hodoscope Front-End card

The hodoscope is designed to tag in space and time the incoming beam ions, so that the signal read-out must be optimized to provide accurate time measurements and a high detection rate acceptance, with reduced dead time and detection efficiency close to 100%. In particular, the design requirements include a maximum counting rate acceptance of 10^8 Hz per detection plane, with a time resolution of 1 ns ([Krimmer et al. 2014](#)). The hodoscope FE card shown in Figure 3.11a has been developed by the IPNL electronics group to fulfill the listed requirements. The Hamamatsu PM is connected to the 64-channel connector (4 connectors of 16 channels each) and two custom ASICs are dedicated to the data first treatment (32 channels each).

A first version of the FE ASIC has been developed in 2012 by the group MICRHAU for the read-out of 8 channels (designed for the 32×32 fiber hodoscope prototype described in section 3.1.4.3). The input part is composed of a current conveyor, and the output one has two sections: a current discriminator and a charge pre-amplifier for the charge measurements in

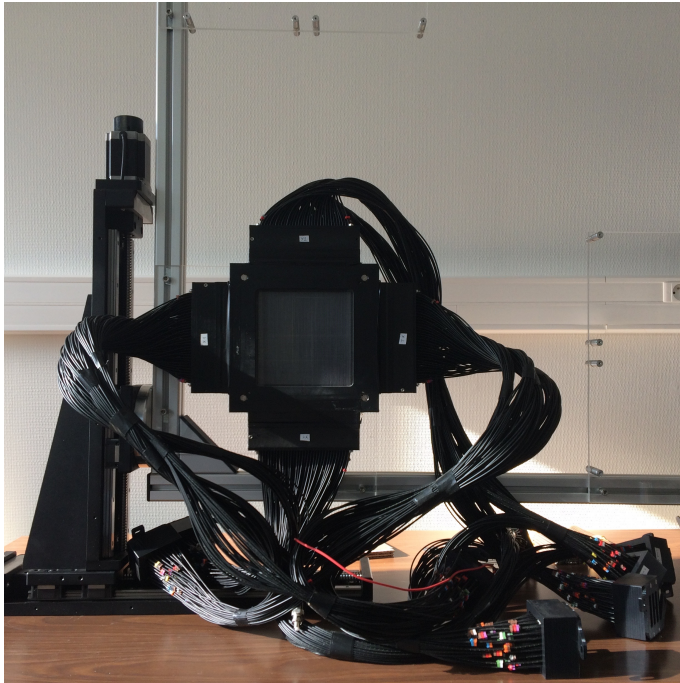


Figure 3.9: 128×128 scintillating fiber hodoscope on its 2-dimensional moving support.

test mode (Deng et al. 2012, 2013). In addition, the ASIC gain can be tuned channel by channel, so that the response of each PM output channel can be fine tuned with respect to the others.

The second version of the ASIC includes all the features of the first version, with the addition of a TDC based on a 160 MHz clock for a more accurate time tagging of the detected events. Moreover, a DLL is installed to divide the main clock in 32 intervals: for each event, the DLL state is stored in a 32 bit register and then encoded in a 5-bit Gray decoder. As a result, the TDC has a 6.25 ns dynamics, with a sampling step of 195 ps and a time resolution of 58.8 ps RMS, for a maximum accepted rate of 10^8 Hz (Deng 2012).

The third and final ASIC version, called HODOPIIC, is adapted to the big size hodoscope (512 read-out channels), with the extension to 32 channels and with the TDC implemented on the second version. An external ADC is used for the charge measurement in test mode for a single channel, selected via slow control. All the ASIC outputs are sent to a FPGA installed on the card for the actual time measurement and data decoding. The FPGA finally handles the data transmission to the acquisition system, depending on the card version.

A first card has been developed to test the first ASIC version with the 32×32 fiber hodoscope. It is based on a FPGA Altera Cyclone III (Altera 2012) and on 9 ASICs, with a LabVIEW acquisition. A single card is enough for the read-out of the complete small hodoscope prototype. This first setup has been tested on beam at the GANIL and the HIT, and a sub-ns time resolution has been verified, together with the expected 1 mm spatial resolution on the two fiber planes and an efficiency of more than 90% at a 10^6 acquisition rate.

The second prototype of the card, shown in Figure 3.11a, has been adapted to the 512-channel hodoscope described in the previous section and to the gamma camera acquisition system

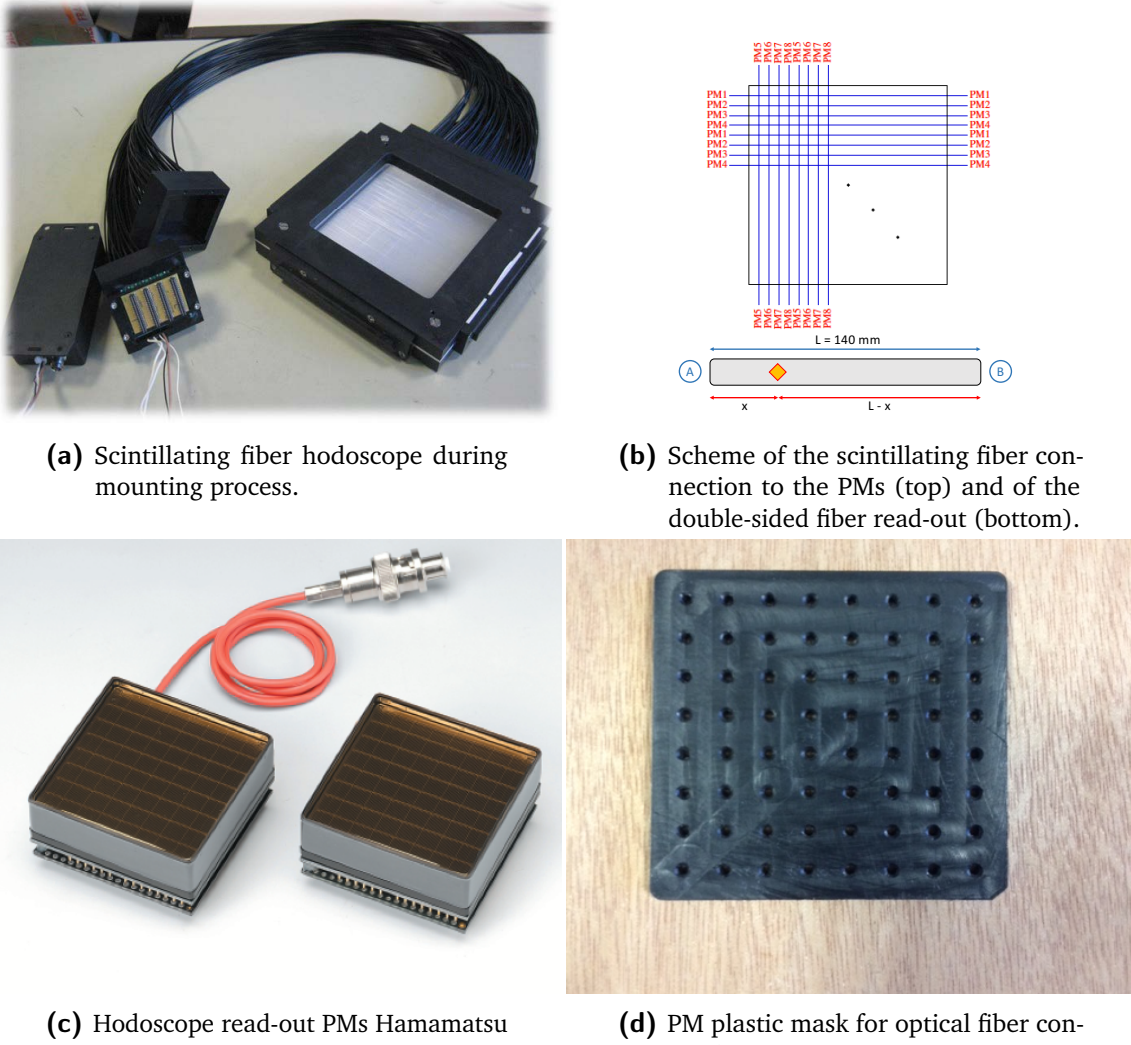


Figure 3.10: Details of the scintillating fiber hodoscope setup.

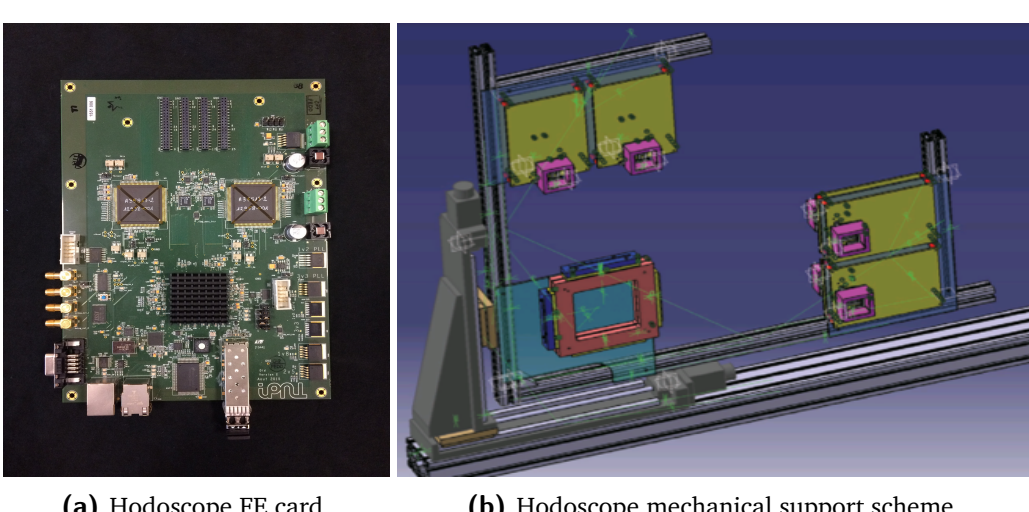


Figure 3.11: HODOPIC board (a) and scheme of the beam-tagging hodoscope two-dimensional moving support (b).

described in 3.1.5: each card has two HODOPIC ASICs, 32 channels each, so that it is designed for the read-out of a single 64-anode PM. 8 cards are then needed for the read-out of the whole hodoscope. This version is based on a FPGA Altera StratixII GX ([Altera 2009](#)), and the connection to the acquisition is ensured by a 3 Gbit/s optical link. 4 digital input-output channels are installed for test and validation purpose, together with an Ethernet port.

Further details about the different card versions and the applied validation tests can be found in [Chen 2017](#).

The hodoscope card firmware has been developed in 2017 and tested in simplified versions on beam, as detailed in chapter 6.

3.1.4.2 Hodoscope mechanical support

The beam tagging hodoscope is set between the beam nozzle and the patient and requires a dedicated mechanical support. In order to profit of the large active area and to be able to remotely control the hodoscope position in the beam transverse plane, the detector is mounted on a 2-dimensional moving table (see the picture in Figure 3.9), which also supports the FE cards. Detector and FE cards are then integral and translate together. A scheme of the moving table is given in Figure 3.11b.

The 2-axis table is provided by Beijing Winner Optical Instruments; it is composed of two motorized linear stages, connected via a right angle bracket. The two stages have a moving range of 30 cm each and the stepper motors have a step resolution of 20 μm . The employed motor controller is a Newport XPS-Q8 ([Newport 2017](#)), equipped with 8 channels for the simultaneous control of a maximum of 8 motors. The movements are steered with an online interface or with a LabVIEW-based program, which will be integrated in the final setup of the slow control software under development with the cameras.

3.1.4.3 Small hodoscope prototypes

Before the production of the large active surface hodoscope prototype described in section 3.1.4, two smaller prototypes have been produced and tested in order to assess the potential of such a kind of detector for the required application. The first and simplest version consisted of one single scintillating fiber per plane, and the readout was performed with two PM tubes directly coupled to the scintillating fibers, without optical fibers. A picture of this prototype is given in Figure 3.12a. This simple version of the detector has been used as a demonstrator of the basic detection principle.

A second small size version of the final detector has been produced with almost the same features as the large area prototype but with simplified read-out logic. It is equipped with two perpendicular planes of $32 \times 1 \text{ mm}^2$ scintillating fibers each (Saint Gobain BCF-10 ([Saint Gobain 2017](#))), with a length of 4 cm and a total active area for a 2D read-out of $32 \times 32 \text{ mm}^2$. As in the big hodoscope, the scintillating fibers are coupled to FORETEC optical fibers which transfer the scintillation light to 4 Hamamatsu H8500 PMs. 16 channels per PM are used, so that 2 PMs are dedicated to the horizontal fibers and 2 to the vertical ones, and the signal

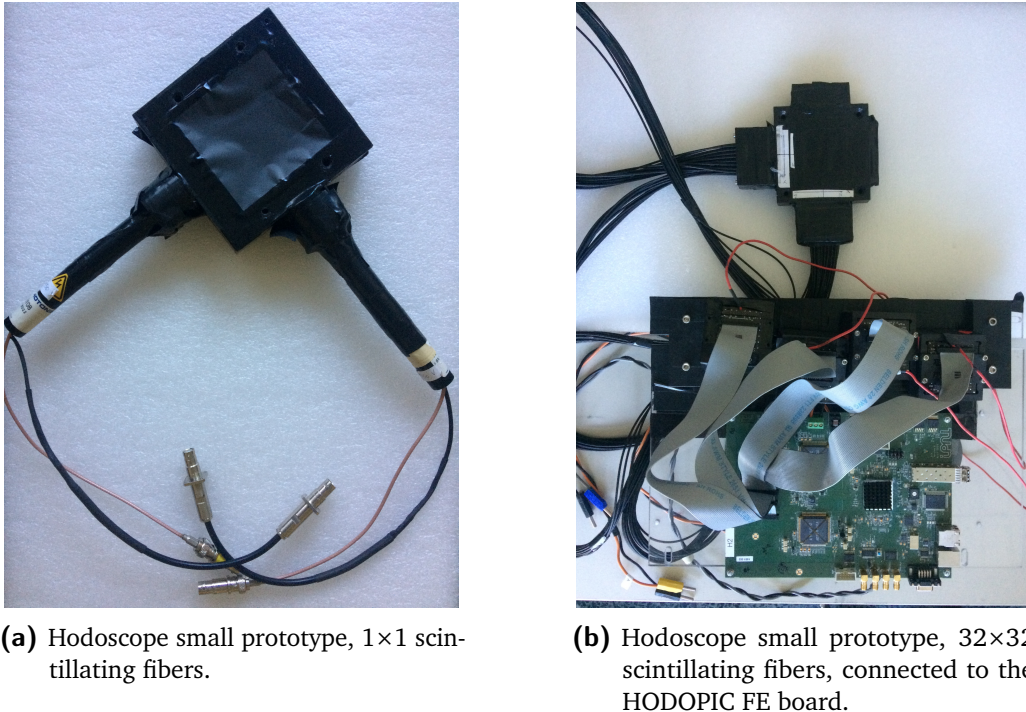


Figure 3.12: Hodoscope small prototypes.

read-out is performed on a single side of the scintillating fibers. As the total number of read-out channels is 64, a single FE card is enough for the whole detector. In Figure 3.12b the 32×32-fiber hodoscope prototype is shown together with its FE card; 4 connection cables (16 channels each) are used to couple the PMs to the FE card.

The 32×32-fiber hodoscope prototype has been tested in 2014 on proton and carbon ion beams (at the GANIL - 75 MeV/u ^{13}C , HIT - protons and carbon ions at various energy, IPNO - 25 MeV protons) with the first version of the FE card (see section 3.1.4.1): an efficiency of more than 90% has been retrieved, with a time resolution of 1 ns FWHM (timing measurements performed with respect to the accelerator high frequency signal). Some more details about this beam tests results are given in chapter 6. The final version of the FE card has been also tested with this detector, and the test description and results are presented in chapter 6.

3.1.5 Camera acquisition system

The TOF gamma cameras developed by the CLaRyS collaboration are composed of various detection sections: beam tagging hodoscope and BGO absorber for the multi-slit collimated camera, with the addition of the silicon scatterer stack for the Compton camera. The acquisition system must be able to handle the data flux from the different components, for a total of 20 FE cards (7 for the silicon scatterer, 8 for the hodoscope and 5 for the absorber), select the events according to the chosen trigger logic and create and send the data packet with the right format to the acquisition PC.

The system is based on the μ -TCA standard; originally conceived as an adaptation of the ATCA systems used in the telecommunication field for high-flux data transfers, it is employed

for relatively simpler tasks and adopted in the particle physics domain since less than ten years (Abellan et al. 2013; Cachemiche et al. 2012). A standard μ -TCA crate equipped with a MCH (shown in Figure 3.13a) is used as general purpose support for the AMC, which is the section adapted for each specific application. An AMC40 has been developed for high energy physics applications, in particular for the LHCb experiment at CERN, and has been adapted for the gamma camera acquisition system by the CPPM research group (see Figure 3.13b). This card includes a FPGA Altera Stratix V (Altera 2016), 24 optical inputs at 4.8 Gbit/s and 12 at 9.6 Gbit/s, a 1 Gbit/s Ethernet output for the connection to the acquisition PC. In addition to the μ -TCA based components, an intermediate card in VME format completes the acquisition system. The so-called THOR card (see Figure 3.13c), developed in VME format at LPC in parallel to the ASM card, is used to generate and share the clock signal common to the whole electronics cards for synchronization purpose (40 MHz) and to govern the pre-trigger and trigger signals as explained in the following lines.

For both cameras, the acquisition starts in case the absorber section detects an interaction: the ASM involved card deals with the creation of a pre-trigger signal, which corresponds to the digital output signal and contains a time stamp (see the ASM card description in section 3.1.3.1). The pre-trigger is sent to the THOR card who governs its distribution to the other system components.

In the multi-slit collimated camera, the pre-trigger signal directly operates as a trigger validating the data collection from absorber and hodoscope. In the Compton camera, the THOR card initially sends the pre-trigger to the scatterer FE cards, which explore their buffer looking for events in the coincidence time window; if a coincidence is found, a trigger signal is generated by the scatterer FE card and sent to the acquisition system, which then starts the data read-out from all the detectors. An graphical overview of the complete acquisition system and logic is given in Figure 3.14.

The AMC40 card makes use of three buffers for the three detector sections, where the collected data are stored until the creation of packets of the selected size to be sent to the acquisition PC. The data transfer is achieved via a 1 Gbit/s Ethernet link, and the chosen standard is the UDP. The data format has been fixed at the camera conception stage and slightly modified following the electronics developments; it is deeply described in the appendix A, which also reports the expected data flow obtained in previous simulation studies.

In addition to the already explained functions, the μ -TCA is also in charge of handling the slow control signals for the configuration of the detector FE cards. The chosen format is in this case the TCP, which is more reliable and ensures a feedback in case of communication failure. The possible slow control signals are detailed in appendix A.

3.1.6 Camera acquisition, monitoring and slow control software

The UDP data packets sent by the μ -TCA acquisition system via Ethernet link are received by the acquisition PC thanks to a C++ based acquisition software, developed at the IPNL. The software decodes the data packets and builds the events by grouping the data from the two (for the multi-slit collimated camera) or three (for the Compton camera) detection sections according to the time stamp. During the decoding process, the software also verify the received data format and can highlight problems in the data encoding by the μ -TCA; this feature is used

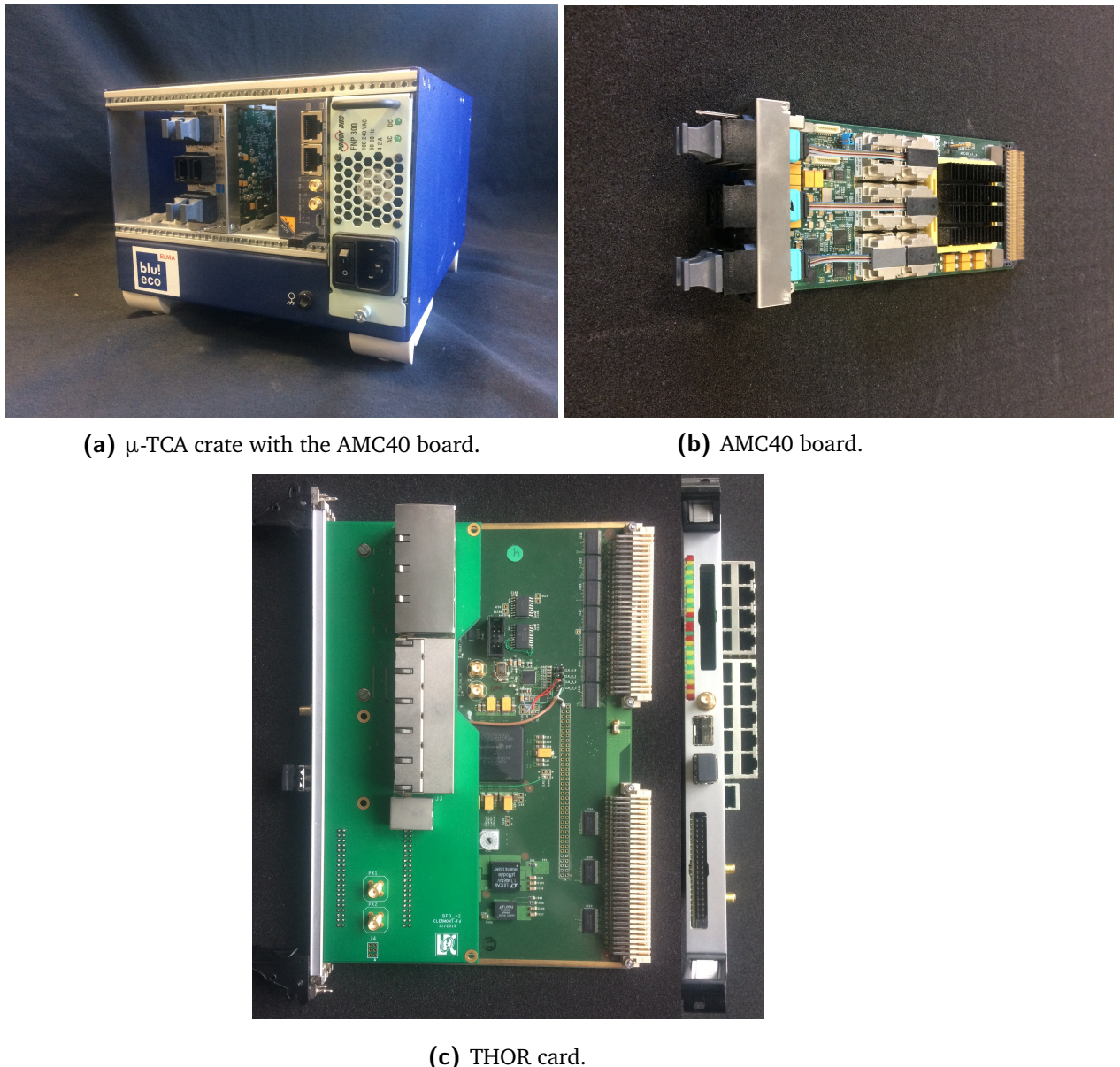


Figure 3.13: Acquisition system components: μ-TCA crate (a), AMC40 board (b) and THOR card (c).

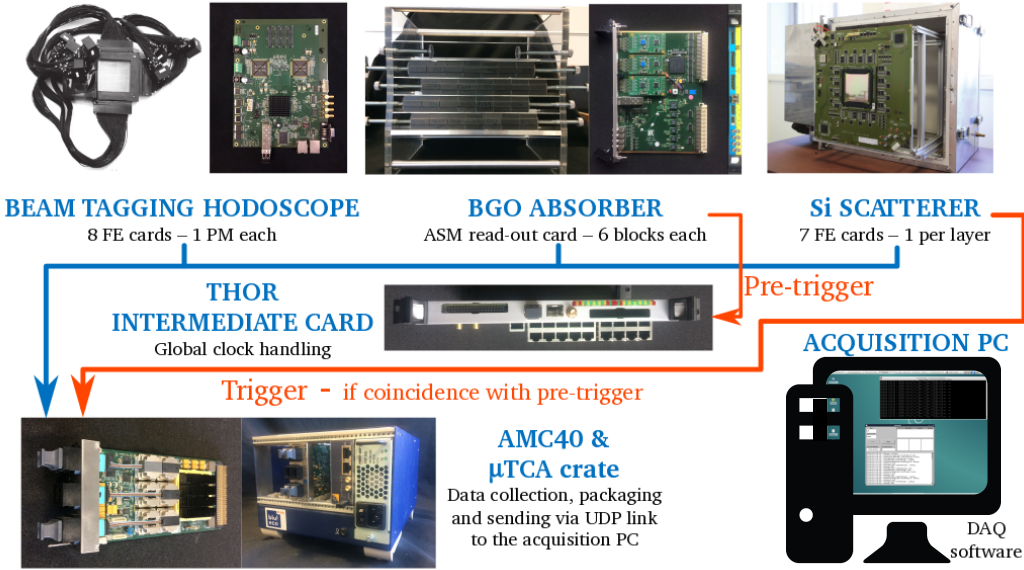


Figure 3.14: Schematic view of the Compton camera acquisition system. For the multi-collimated camera, the trigger and pre-trigger signals are the same.

during the test phase to check the functionality of the AMC40 firmware. The reconstructed events are then stored in binary files with the structure presented in appendix A. The data file size can be selected by fixing the number of events stored per run in the acquisition run, knowing that each event can be composed by slightly different number of bits, according to the amount of detector modules involved. The file collection corresponding to the same run will be then grouped at the analysis stage. The number of events per file must be tuned taking care of the available RAM (32 Gb), where the data are temporarily stored before the writing process on the hard-disk. In Figure 3.15a the minimal graphical interface developed for the acquisition software is shown.

A monitoring software has been developed in order to have a direct real-time feedback on the camera data acquisition. The software can show some information about the ongoing data collection, and it is at present designed to work on a single detector section (hodoscope, scatterer or absorber). It is based on ROOT (Brun et al. 1997) with the following working logic: during the acquisition, it continuously searches for new data files in the storage folder, and analyses in the desired way a selected number of events per file, directly from the binary format. An example of the visualized output for an hodoscope monitoring is shown in Figure 3.15b. This picture corresponds to an acquisition performed during a beam test at the CAL, where the 32×32 fiber hodoscope have been tested, together with the monitoring software. More details about the beam test are given in chapter 6.

As mentioned, the present version of the software is not yet adapted to the monitoring of the whole camera, even if it can handle at least two detectors with minor modifications. In addition to this, it is not automatically synchronized with the acquisition software, and not optimized in terms of needed calculation time. In the next future the planned upgrade will slightly modify the working logic by directly connection the monitoring to the acquisition: the acquisition software will automatically send a selected fraction of events to the monitoring

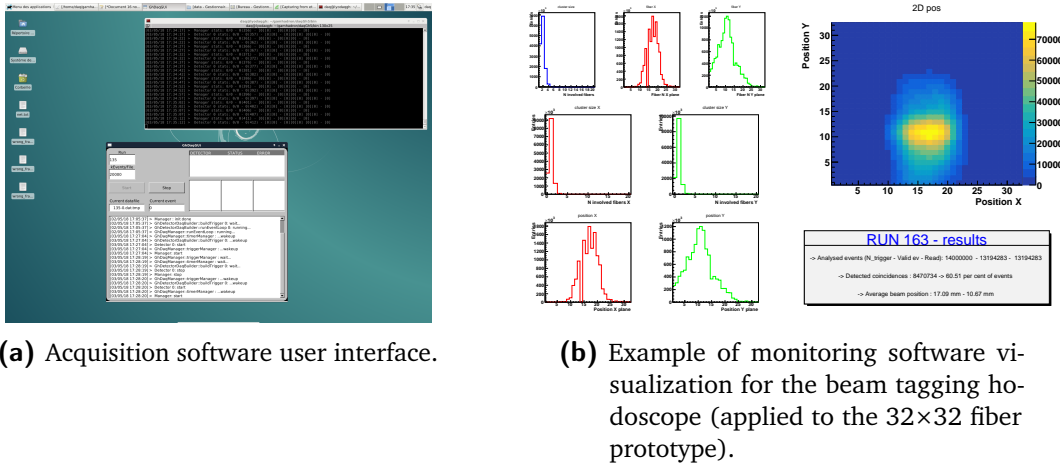


Figure 3.15: Software tools: user interface of the acquisition C++ software (a) and example of the ROOT (Brun et al. 1997) monitoring software visualization for the beam tagging hodoscope 32×32 fiber prototype.

output during the acquisition, so that the search for data files would not be anymore necessary. This will drastically reduce the monitoring dead time and calculation time, achieving an actual online control.

Acquisition and monitoring software has been tested thanks to a data simulator developed in C++, which is able to create data UDP packets with the correct format and send them on the same Ethernet port used for the data collection, simulating a server-client communication.

As mentioned in section 3.1.5, the μ -TCA handles both the data collection and transfer and the slow-control of the whole system, where with slow-control we intend the configuration of all the electronics cards (discriminator thresholds, channel gains, ASIC reset signals, working mode, etc.) and the read-out of the feedback signals. The development of the slow-control software is ongoing at the IPNL: it is designed in LabVIEW and includes all the needed controls in a single user interface. A dedicated PC is foreseen for this task, connected to the μ -TCA via TCP protocol. The slow-control software will also govern the high and low voltage suppliers for the detectors and acquisition electronics boards, the scatterer thermal box temperature setup and control, the steering of the 2D positioning table dedicated to the hodoscope, and the steering of the camera moving table, described in the next section. All the listed instruments will be connected to a patch panel, and a local network will be created for the camera equipment.

3.1.7 Camera integration and mechanical support

In order to setup the two camera configurations (multi-slit and Compton), the described components, together with the related mechanical supports, must be integrated in an integral system, with the exception of the beam tagging hodoscope who has its own dedicated mechanical support, being placed between the beam nozzle and the target. A general mechanical structure is then needed to support the camera; it is required to be movable, as compact as possible but at the same time robust and large enough to support absorber and scatterer (or collimator), for a total maximum weight of about 100 Kg. In addition to this, it should be



(a) Schematic view of the Compton camera integration on the positioning table.

(b) Gamma camera position table.

Figure 3.16: Details of the gamma camera integration and mechanical support.

possible to remotely control the position of the various camera components in order to adapt their position in 3D with respect to the beam line and to the target.

The realized solution is shown in Figure 3.16b. It is composed of two sections: a positioning table on wheels, designed and provided by Rose & Krieger, equipped with 4 telescopic feet, and a 4-axis moving table installed on it, developed by Kinetic System. The wheels allow to first position the camera, and the 4 telescopic feet are used to regulate with 1 mm precision the whole system height, in the range 630 mm - 1280 mm from the ground, to be adapted to the specific beam line. The feet are expected to be able to support a maximum weight of 150 Kg. The telescopic feet are not connected to the slow-control but are controlled by a remote controller on the table itself. On the top surface of the table, $1200 \times 750 \text{ mm}^2$, the 4-axis moving table is fixed and allows to adapt the camera position in 3D (distance camera-target, height, direction parallel to the beam line) with a $100 \mu\text{m}$ resolution and a range of 40 cm. In addition to this, a fourth axis allows to adjust the distance between the two detector components in the direction perpendicular to the beam line, in a range of 30 cm (to be noticed that this range is reduced by the size of the scatterer thermal box). The four axes are connected to the positioning table patch panel, which is directly controlled by the slow-control program in LabVIEW. Finally, a further manual control allows to rotate the whole system with respect to the table axis, in a range of ± 10 degrees.

In Figure 3.16a we present the mechanical scheme of the complete positioning table, with the Compton camera installed on it.

In Figure 3.17 we show a view of the three detectors composing the Compton camera, with one scatterer layer installed in the thermal box and the absorber mounted on the positioning table, and the beam tagging hodoscope on the right side on its dedicated mechanical support.

3.1.8 Data analysis and image reconstruction

All the data collected at the detector characterization stage (in standalone working mode) are analyzed via ROOT (Brun et al. 1997) and Python custom developed code. Further details

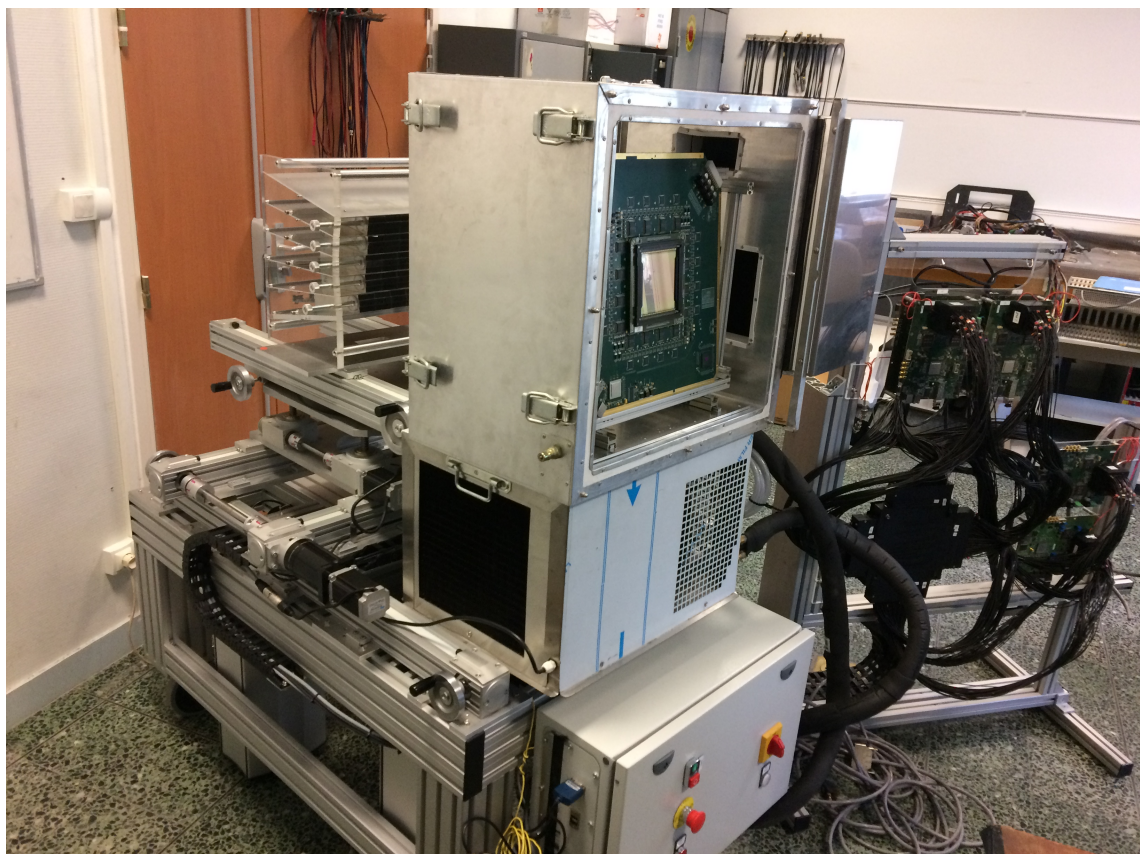


Figure 3.17: Complete Compton camera with beam tagging hodoscope on the developed mechanical supports.

are given in section 3.2, where the performed characterization measurement on the three detector section are described. Concerning the data analysis for the complete systems (multi-collimated and Compton camera), automatic ROOT-C++ based programs will be developed in order to achieve an online data treatment for both tests and clinical application purposes. The raw collected data samples must be adapted to the image reconstruction codes, needed to retrieve the final image for both camera configurations.

The multi-collimated camera is designed to provide 1-D information about the prompt-gamma emission distribution: the required data treatment is then relatively simple, and based on the chosen geometrical configuration of collimator and absorber. The detected events are spatially assigned to the BGO block pseudo-pixel where the gamma interaction took place, by means of center of gravity calculation with the four signals provided by the involved block and then with an automatic algorithm developed for test purposes and detailed in section 3.2.2.3. Knowing the block position within the whole absorber setup, the prompt-gamma emission profile can be reconstructed assuming a photon path perpendicular to the absorber entrance face. This simple approach can be refined thanks to the spatial information given by the beam tagging hodoscope. The detected beam position can constrain the reconstructed emission position to a point, so that a 3-D emission profile can be obtained. This solution is being explored but a final, working reconstruction code is still not available.

Concerning the Compton camera, the image reconstruction requires the detection of coincidences in the scatterer and absorber sections: position and deposited energy information in the two detectors allow for the reconstruction of the emission cone via Compton kinematics, as explained in details in chapter 2. The photon emission profile (prompt-gammas for the ion beam therapy application, gamma emitted by the radio-tracer for the nuclear medicine approach) is then obtained via the overlap of several reconstructed cones. As described in chapter 2, analytic and iterative algorithms have been proposed and developed to reconstruct the final image given by a Compton camera, which intrinsically transport a 3-D information. In particular, the image reconstruction of the CLaRyS Compton camera relies on the code developed by the CREATIS group for both the analytic ([Maxim et al. 2009](#)) and iterative ([Hilaire et al. 2014; Lojacono et al. 2013; Maxim 2014](#)) methods.

The analytic reconstruction is only applicable in ion beam therapy monitoring and is based on the intersection of each reconstructed emission cone with the beam direction information given by the beam tagging hodoscope. This method assumes that the prompt-gammas are generated along the beam path, considered as a straight line, and limits to two points the possible emission position for each detected events. The overlap of several events will then allow for the emission distribution definition in 2-D. The Compton camera performance have been tested for the application in ion beam therapy monitoring, and this reconstruction code has been employed to treat the simulated data: the results are given in chapter 4, where we usually refer to this reconstruction method as “line-cone”.

The iterative algorithm is called LM-MLEM and is able to include in the calculations the space and energy resolution of the involved detectors, leading to the reconstruction of a 3-D image. It requires the definition of a reconstruction volume, which is divided in a given number of voxels, and the list of coincidence events. Starting from the simple event back-projection, it defines the probability that a given photon detected in the Compton camera has been emitted from the voxels in the defined volume. For every iteration, this probability is re-computed taking into account the results of the previous iteration, converging to the most likely emission

distribution. The number of iteration is fixed by the user and must be a trade-off between reconstruction accuracy and calculation time. This method has been used with ion beam therapy monitoring simulated data and compared to the line-cone method (see chapter 4), as well as for the reconstruction of point-like sources simulated for the application of the camera in nuclear medicine, presented in chapter 5. To be noticed that, concerning the reconstruction of prompt-gamma emission distribution in ion beam therapy application, the spatial information about the beam given by the beam tagging hodoscope is still not included in the employed version of the code. An upgrade is under study, but it has not been tested yet and it has not been used to obtain the results presented in this thesis.

3.2 Camera component characterization and development status

As detailed in the previous sections, the CLaRyS TOF gamma cameras are equipped with various detector components with very different features. Each part must be separately studied in order to characterize its behavior and allow the final camera integration and operation.

I mostly worked on the beam tagging hodoscope and on the BGO absorber, and in the next paragraphs the performed measurements are described in details. Concerning the scatterer stack, the results achieved before the beginning of my PhD thesis are briefly described for the sake of completeness.

The results presented in this section also introduce the following one (3.3), where all the development steps still needed for a clinical implementation of the cameras are explained.

3.2.1 Scatterer silicon layer characterization

The 7 DSSDs selected for the application in the Compton camera system among the 10 provided by the producer have been characterized in terms of leakage current. The measurements have been performed by colleagues before the beginning of my PhD thesis, and are summarized here for the sake of completeness. The extended description of the employed test-bench, the performed tests and the results is presented in [Ley 2015](#).

The leakage current is an evaluation of the systematic uncertainty expected on each read-out channel, corresponding to a background current detected without an energy deposit in the depletion region. The 7 layers have been tested at the complete depletion voltage of -750 V with a test-bench developed at the IPNL specifically for these measurements. It is composed of a custom electronics card which is used to supply the detector with the depletion voltage and to the current read-out via the connection to a nano-amperometer (NIM module with 0.1 nA resolution). Moreover, temperature variations in the range -40°C - +40°C have been realized with an automatic system, with the detectors and read-out card placed in a temperature programmable chamber Weiss WTL 64 ([WeissTechnik 2017](#)). The temperature variations, the channel selection and the data acquisition are handled by a Raspberry Pi. The temperature step has been fixed to 5°C. Finally, temperature cycles have been carried out in order to study the detector response to rapid temperature variations and the time required

to stabilize the leakage current at the working temperature, with temperature steps between -20°C (working temperature) and +25°C (room temperature).

The leakage currents measured at room temperature (+25°C) are homogeneous on all the strips, with some local exceptions. The average detected value is about 20 nA. Concerning the measurements at -40°C, the average value for the n strips is close to 0 nA, while a current of 3-4 nA is still detected on the p strips. On each layer, a maximum of 3 strips show higher leakage current values; this is acceptable for the final application in the Compton camera. Moving from -40°C to +40°C, the leakage currents respect, on average, the expected trend defined by equation 3.1 (Spieler 1998).

$$I_p(T) \propto T^2 \times e^{-\frac{E}{2k_B T}} \quad (3.1)$$

where $I_p(T)$ is the leakage current as a function of the temperature, T is the temperature in Kelvin, E the silicon energy gap energy in eV, k_B the Boltzmann constant (8.617×10^5 eV K $^{-1}$).

The leakage current is generally stable or is slightly increasing for temperatures below 0°C, with values always below 10 nA. Beyond 0°C, it rapidly increases reaching some tens of nA at 40°C, depending on the specific strip. This observation justify the need of the described thermal regulated box, which is able to maintain a constant temperature of -20°C during the detector operation, placing them in a minimum and stable leakage current regime.

The application of quick temperature variation steps between -20°C and +25°C allowed to estimate the time required by the detector to re-establish the working regime with minimal leakage current. When moving from -20°C to +25°C, the leakage current increases rapidly up to the values already detected during the slow temperature variations, with a transition time of the order of less than ten minutes. Approximately the same time is required to stabilize the leakage current after the cooling down to -20°C.

In addition to the described leakage current measurements carried out with the 7 10×10 cm 2 DSSDs, a small silicon layer prototype (8×8 strips) has been tested with the first version of the FE card ASIC. The first version of the card allowed for the read-out of 8 channels, so that the 8 p strips have been characterized with this read-out system, while the n strip data have been collected with NIM modules. The data treatment has been performed thanks to VME modules.

The detector has been exposed to ^{22}Na and ^{57}Co radioactive sources: the ^{22}Na source, producing two back-to-back 511 keV gammas as a result of the β^+ annihilation, has been used for timing measurements in coincidence with a LaBr₃ crystal, while the 122 keV photons of the ^{57}Co source are used to characterize the energy response by photoelectric absorption.

The detected time resolution has been estimated to be in the range 13-23 ns FWHM for the p strips, and between 30 and 80 ns FWHM for the n strips (knowing that the “hole” drift time is about 3-4 times more than the electron one). The energy resolution is between 10 and 20 % FWHM for the tested strips. This test also allowed to verify the first version of the card and move forward with the development of the second and third version at present available for the final detector.

Thanks to the summarized measurements, a calibration database is available for the 7 silicon layers, which showed overall stable and acceptable performance. The final version of the card must be tested in order to check these results, validate the board behavior and move to the first detector tests on beam. All the details concerning the next development steps are presented in section 3.3.1.

3.2.2 Absorber BGO blocks characterization

The BGO modules composing the Compton and multi-collimated camera absorber have been recovered from a SIEMENS PET system: they have been originally optimized for the detection of 511 keV photons from positron annihilation, and they have to be tested for the new gamma detection system, which must be able to deal with photons in the prompt-gamma energy range, i.e. from some hundreds of keV to a few MeV.

Each block must be characterized in terms of spatial and energy response, and the read-out PMs have to be calibrated to obtain a uniform response on the whole block surface (see section 3.1.3 for the detector description). The employed method relies on the work presented in Rogers et al. 1994 and Tornai et al. 1994 and on the calibration process described in Golnik 2015 and Hueso-González et al. 2015, and has been extended with more refined features.

The measurements are performed with the irradiation by gamma sources, emitting photons at defined energies: in particular, we used 511 keV and 1275 keV photons from a ^{22}Na source, and the two photons emitted by a ^{60}Co source, at energies of 1173 keV and 1332 keV.

The employed ^{22}Na source is a cylindrical source with an active diameter of 4 mm, and an activity of about 400 kBq: it has been placed at a distance of about 5 cm from the block entrance surface, with the center of the source facing the center of the block transverse surface. The ^{60}Co source has been installed in a lead cylindrical container (12 cm radius and 35 cm height), equipped with three different apertures: point-like ($2 \times 2 \text{ mm}^2$), linear ($2 \times 50 \text{ mm}^2$) and squared ($50 \times 50 \text{ mm}^2$). The design of the lead container has been studied in simulation to ensure the proper radiation protection, and produced according to the specifications defined by the IPNL mechanics group. The activity of the ^{60}Co source is about 1.7 MBq, and the square shape has been used to obtain an homogeneous irradiation of the BGO block, with the block set with the center of the entrance surface corresponding to the source position, at a distance of 12 cm.

The signals produced by the four PMs of each block are collected via four analog outputs on the FE card (see picture 3.6a). The four retrieved signals per event are treated via standard NIM modules in order to be adapted to the acquisition systems and measurement purposes.

Two different acquisition systems have been used for this characterization work. First, the PXIe described in section 3.2.3 with its two flash ADC read-out modules, 8 channels each, is used for the spatial and energy characterization and calibration of the tested blocks. The raw signals coming from the four PMs are amplified and shaped via NIM modules (quad shaping bipolar amplifiers), which were fine-tuned via a pulse generator in order to adapt the amplification factor of each channel (an amplification factor of about 50 has been applied to the raw signals). The amplified signals are then split in order to be treated for trigger purpose. The trigger for the acquisition is based on the sum of the four signals, and a fixed threshold

is applied for background rejection. The employed discriminator provides the logical trigger signal, which is sent to the trigger input of the ADC modules on the PXI. The four amplified signals, conveniently delayed, are sent as inputs to the ADC modules on the PXI, together with the sum signal which is used for experimental verification of the acquisition setup. A LabVIEW-based acquisition software, developed for this particular application at the IPNL, provides real time event visualization together with a partial, on-line spatial reconstruction of the events, and stores them in text files for further analysis. A second threshold can be set at the software level in case particular selections are needed during the acquisition, otherwise the event selection is performed at the analysis stage. A scheme of the acquisition setup for the spatial and energy calibration is given in figure 3.18.

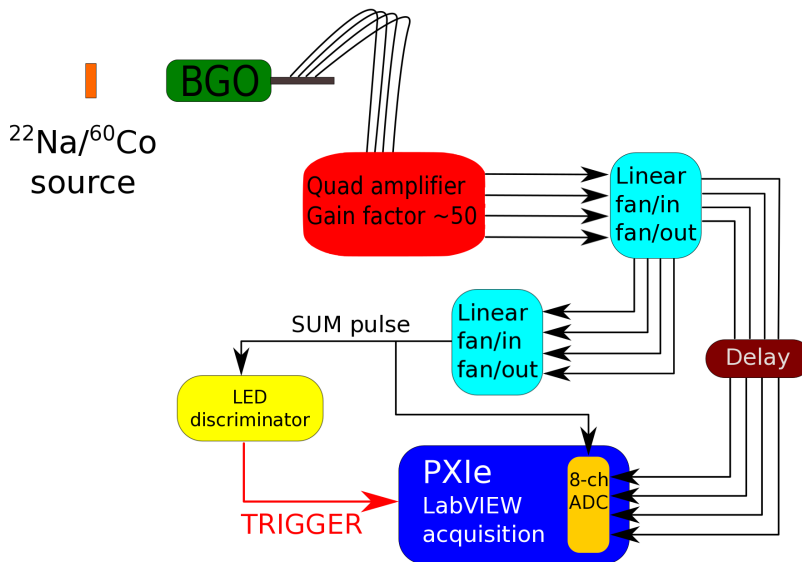


Figure 3.18: Scheme of the spatial and energy characterization test-bench.

Concerning the timing characterization measurements, an eight-channel signal digitizer at 3.2 GS/s has been employed for high time resolution acquisitions. The so-called WaveCatcher, shown in Figure 3.19a, has been developed by the LAL in Orsay and the IRFU in CEA-Saclay, and its features are detailed in Breton et al. 2014. The digitizer is connected to the acquisition PC via USB port, and the data read-out and storage are performed thanks to a custom acquisition software. The measurements are based on the coincidence detection of back-to-back 511 keV photons emitted by a ^{22}Na radioactive source, in order to be able to compare the time response of the tested BGO block to a reference fast timing scintillator. An external trigger is then provided to the WaveCatcher by treating the BGO block and reference scintillator signals with logic coincidence NIM modules, after proper discrimination. Further details are given in section 3.2.2.4, while a scheme of the acquisition setup is given in Figure 3.19b.

3.2.2.1 Space and energy calibration and characterization

The space and energy calibration process is mainly divided into three stages:

- PM gain equalization (^{22}Na): the block is irradiated with the ^{22}Na source and the raw

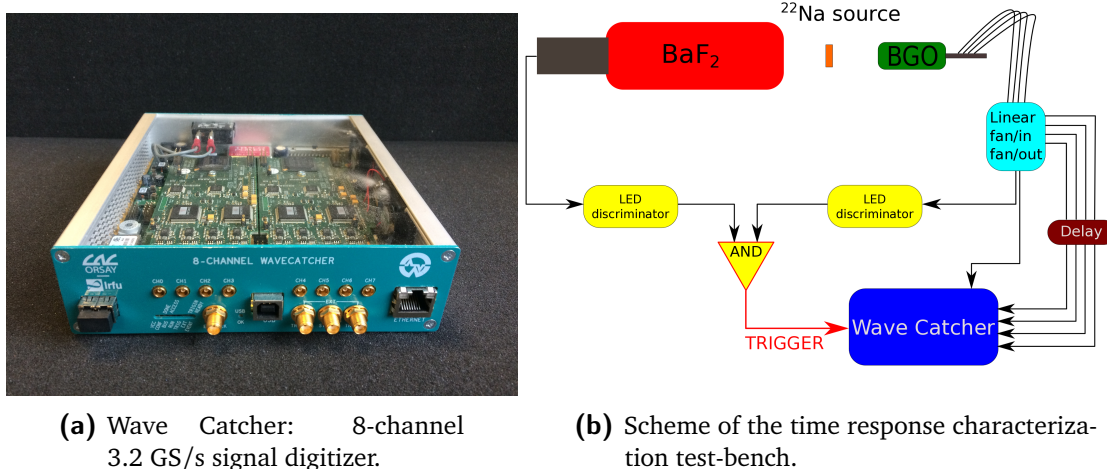


Figure 3.19: Details about the BGO block time response characterization.

ADC distributions for the four PMs are retrieved. The upper-energy falloff in the raw ADC spectra are taken as reference to equalize the distributions. Four energy calibration factors are extracted and used to the data correction; this correction corresponds to the PM gain equalization.

- Pixel identification (^{60}Co): once the calibration factors are extracted thanks to the ^{22}Na irradiation data, the block is exposed to the ^{60}Co source. The collected data are analyzed as in the previous step and calibrated according to the already calculated correction factors. The energy spectrum, the mono-dimensional spatial projections and the flood map are produced. The custom algorithm briefly described in the following section 3.2.2.3 has been developed to identify the pseudo-pixel positions on the flood map. It is applied to the ^{60}Co irradiation data and the pseudo-pixel position map is stored.
- Pixel energy calibration: the ^{22}Na irradiation data are re-analyzed in this last calibration step in order to assign each interaction to a single pseudo-pixel according to the pixel position map obtained with the ^{60}Co data. Then, the energy spectrum of each pixel can be produced and the two identified peaks (corresponding to the two photon energies emitted by the ^{22}Na source - 511 keV and 1275 keV) can be used to equalize the pseudo-pixel response. The sum of all the pixels spectra produces the block energy spectrum. At this stage, the ADC channel values are calibrated to obtain the absorbed energy values in keV.

It is worth to notice that the ^{60}Co irradiation is useful for the pixel identification given the high energy and narrow energy range of the emitted photons. The equalization factors obtained with the ^{22}Na source irradiation have been verified to be consistent with the ^{60}Co irradiation data, as expected. The whole method results to be robust.

3.2.2.2 Qualitative test of spatial reconstruction accuracy

Specific acquisitions have been devoted to the test of the block spatial accuracy potential. The detector is expected to be able to locate the collected interaction on the pseudo-pixel grid,

but the possible sub-pixel accuracy can be tested with a collimated source scan of the block surface. The ^{60}Co source has been employed for this purpose, with the linear aperture. The block has been placed on a moving table with no distance between its entrance surface and the collimator aperture. The whole surface has been irradiated with horizontal and vertical movements of 1 mm and 2 mm per step. The collected data have been calibrated with the factors obtained with the homogeneous ^{22}Na irradiation, as explained in the previous section. We present and qualitatively discuss the results in section 3.2.2.6.

PUT ALSO POINT-LIKE SCAN ????

3.2.2.3 Pixel identification and energy calibration algorithm

Subsequent to that gain equalization process, an automatic iterative algorithm has been developed to identify the block pseudo-pixel positions. Integrated mono-dimensional spatial projections are computed along rows and columns of the calibrated flood map in order to derive the peak and valley positions in the distributions with the ROOT (Brun et al. 1997) methods included in the TSpectrum class and simple analytical calculations. With the resulting valley positions, a first rectangular grid of pseudo-pixels is initialized. The projection of each identified pseudo-pixel row (respectively column) is re-analyzed using the same integrated 1-D spatial projections along columns (respectively rows) looking for peaks and valleys as before. A refined grid is then produced, distorted from the initial rectangular one, and this process is iterated until a complete 8×8 pseudo-pixel grid is obtained.

Once the pseudo-pixels grid is fixed, the maximum (center of gravity of counts) of each pseudo-pixel region is automatically identified and its position defines the pseudo-pixel center relative position in the map.

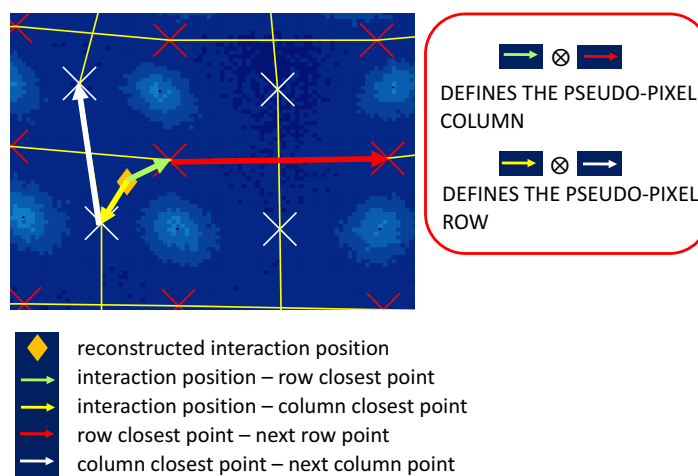


Figure 3.20: Logic for the event assignment to a single pixel. The dual pseudo-pixel grid is displayed: in white the mid points on the pseudo-pixel edges along rows, in red along columns. The sign of the outer products detailed in the red box are used to define the column and row (so that the pseudo-pixel) where to assign the reconstructed event.

The event data are then assigned to the pseudo-pixels with the application of the following process, illustrated in Figure 3.20. The dual pseudo-pixel grid is created rows- and columns-wise to get the mid points on the pseudo-pixel edges. The even data assignment is then done by calculating the minimal distance between a column and a row average point with respect to the reconstructed event and then calculating two outer products, between the vector connecting the reconstructed point and closest column (row) average point and the vector connecting this average point to the previous or next one on the same column (row). The sign of the products defines the column (row) where to assign the interaction. Knowing the relative position of the interaction point with respect to the two minimal distance points on row and column, the correct pseudo-pixel is identified. A more simple approach could have been used, using the search of the minimal distance between the reconstructed event position and the pseudo-pixels centers, but it proved to be more liable to some assignment discrepancies due to the grid distortions.

3.2.2.4 Time response characterization method

The test-bench for the time response characterization has been set as shown in Figure 3.19b. A BaF₂ mono-block scintillator, read-out by a single photo-multiplier tube, has been used as reference detector. Its excellent time resolution makes it suitable for relative timing measurements in comparison to the BGO blocks. The reference scintillator and the BGO block under test have been set at arbitrary distances from the ²²Na source with the aim of detecting in coincidence the two 511 keV back-to-back photons resulting from the positron annihilation. The four raw signals coming out from the BGO block are summed with a NIM linear fan-in/fan-out module, and the resulting signal is sent to a leading edge discriminator and converted to a logic signal according to a fixed threshold. The single signal emerging from the reference detector passes through a selected threshold and is converted to logic signal. The two digital pulses, 100 ns width, are then sent to a coincidence module to create the trigger input for the WaveCatcher acquisition system described in section 3.2.2. The four BGO output raw signals, the reference scintillator raw output signal and the sum of the four raw BGO signals are sent to the WaveCatcher for digitization. An example of the collected raw signals from the reference block is shown in figure 3.21: the 4 output signals of each single PMT are shown together with the resulting sum signal. The four signals exhibit a noisy feature that could be observed using the fast sampling acquisition, with a 80-100 MHz oscillatory behavior. At the present stage we did not infer the sources of this noise, that would be canceled by appropriate lower frequency filtering.

For each coincidence event, the six collected signals are analyzed with focus on the signal rising edge. The time corresponding to the amplitude maximum and to 20%, 30%, 50% and 80% of the maximum is retrieved for constant fraction discrimination tests. In addition to this, a fixed threshold is used for fixed value discrimination.

Different comparison methods have been tested in order to identify the more robust one for the definition of the time resolution of the blocks. The noisy structure of the single BGO raw signals (see figure 3.21) leads to very variable results depending on the defined threshold, and the more stable results are given by the comparison of the sum of the four BGO signals and the reference scintillator with the arrival time identified by a fixed tuned threshold. With this method, the arrival time of each signal can be defined and the time difference distribution of the two signals can be produced.

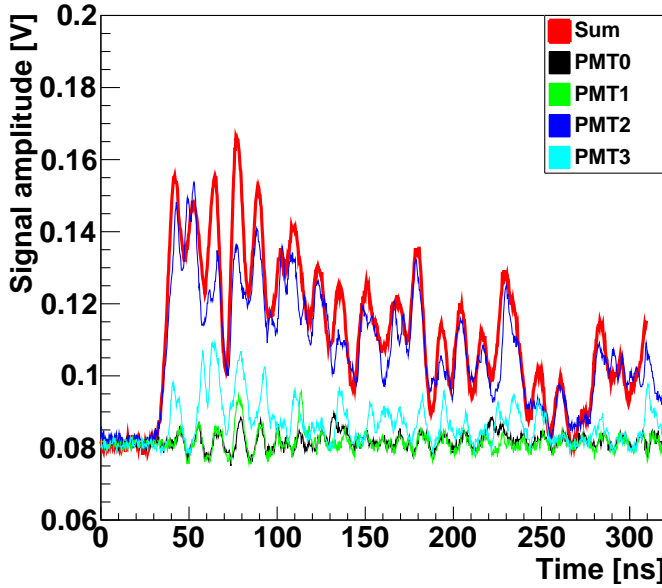


Figure 3.21: Reference BGO block raw signals collected with the Wave Catcher acquisition system. The four outputs of the single PMTs are shown together with the sum signal.

The same analysis has been applied to a data set obtained with two identical BaF_2 detectors exposed to the ^{22}Na source in coincidence. This data set allowed for the definition of the reference scintillator time resolution.

The resulting BGO time resolution is defined as the FWHM of arrival time difference distribution between BGO block and reference scintillator, with the subtraction of the reference scintillator contribution via uncertainties composition calculation.

3.2.2.5 Results: PM gain equalization

Figures 3.22, 3.23, 3.24, 3.25 show the effect of the PM gain equalization on the data collected with the reference BGO block irradiated with the ^{22}Na source. Figures 3.22a and 3.22b show the raw and equalized ADC profiles of the four read-out photo-multipliers (the peaks above 3000 ADC counts in Figure 3.22a correspond to the saturation of the NIM linear fan-in/fan-out module used to handle the data read-out; these values are rejected during the equalization stage). Figures 3.23a and 3.23b show the projection on the two axes of the position of interaction reconstructed via Anger logic, before (left) and after (right) the PM gain equalization. Figures 3.24a and 3.24b show the ADC event spectrum, obtained by the sum of the ADC values of the four PMs, before (left) and after (right) the PM gain equalization. Figures 3.25a and 3.25b show the two dimensional event position map (this will be called “flood map” in the following), before (left) and after (right) the PM gain equalization; the interaction position is reconstructed via Anger logic (see Figure 3.5d for details).

As shown by Figures 3.22 to 3.25, the PM gain equalization performed in this first calibration step is mandatory to optimize the spatial and energy response of the tested block. Figure 3.23b highlights the better definition of the pseudo-pixels ensured by the gain equalization: the peak-

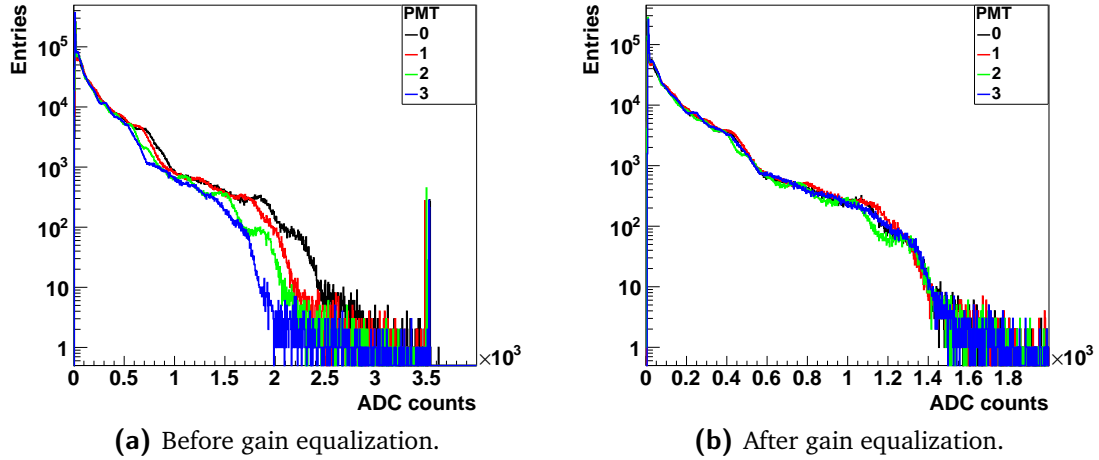


Figure 3.22: PM signal amplitude spectra before (a) and after (b) the PM gain equalization.

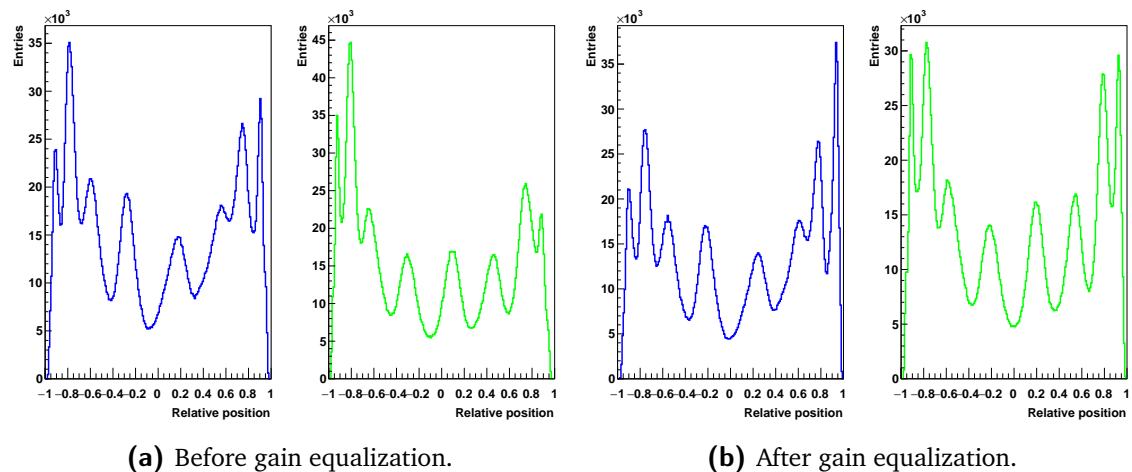


Figure 3.23: 1D integrated position distribution on the two transverse dimensions before (a) and after (b) the PM gain equalization. Blue curves: horizontal dimension. Green curves: vertical dimension.

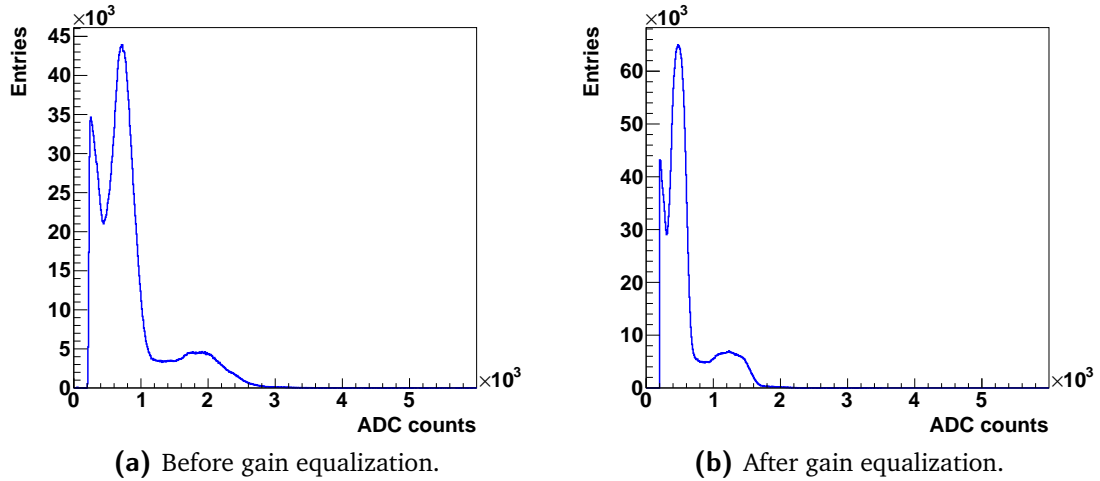


Figure 3.24: Block energy spectrum before (a) and after (b) the PM gain equalization.

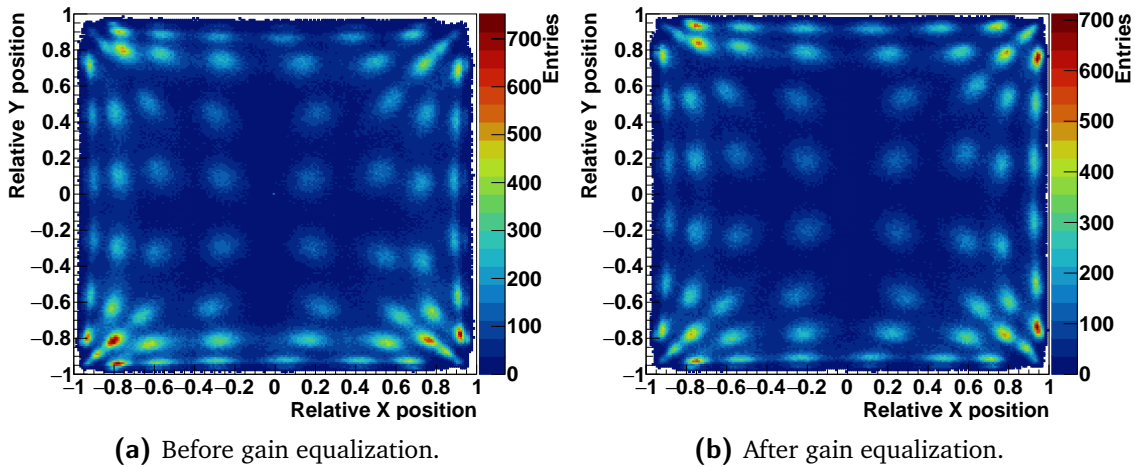


Figure 3.25: 2D reconstructed position map before (a) and after (b) the PM gain equalization.

to-valley ratio is increased, in particular for the most external pixels. The spatial response improvement is also reflected in a better energy response, as shown in Figure 3.24b, where the two energy peaks of the ^{22}Na source are more narrow with respect to the ones obtained with the raw data. The obtained energy response is still not satisfactory, and the next steps of the calibration process are dedicated to the improvement of this result. The flood map in Figure 3.25b shows how the gain equalization and the offset tuning allow to arrange the position map over the whole block surface; the borders are better defined and the pseudo-pixels on the block limits (especially on the corner) are better separated.

3.2.2.6 Results: block spatial precision

Figure 3.26 shows four consecutive steps of the ^{60}Co source collimated irradiation, with a 2-mm step movement from left to right and the linear aperture ($2 \times 50 \text{ mm}^2$) set in vertical position. A qualitative analysis is enough to appreciate the block spatial precision limitation.

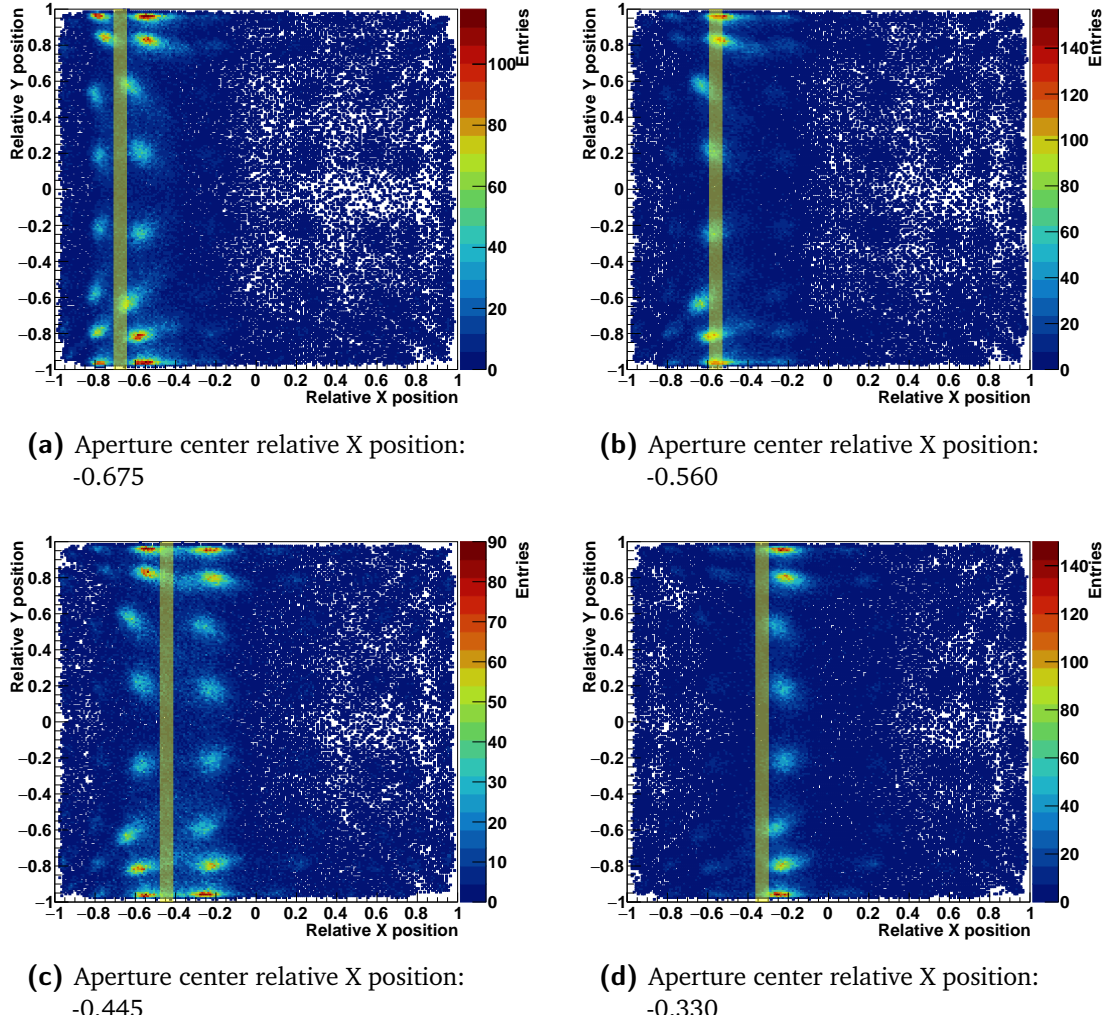


Figure 3.26: 2D reconstructed position maps during a 2-mm step scan performed with the ^{60}Co source with the line aperture from the left to the right size of the block surface. 4 reference measurements points, the position of the aperture is shown by the semi-transparent yellow band.

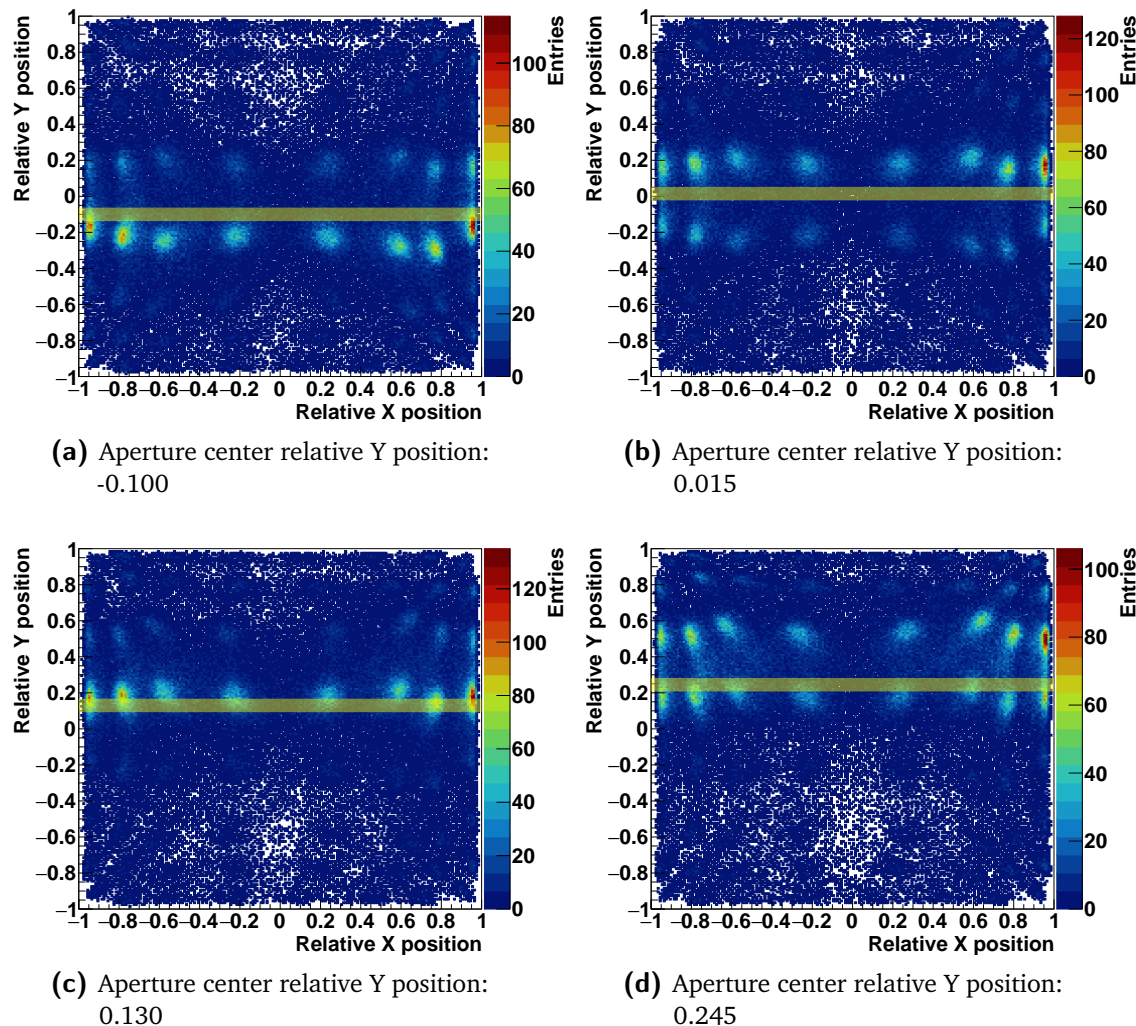


Figure 3.27: 2D reconstructed position maps during a 2-mm step scan performed with the ^{60}Co source with the line aperture from the bottom to the top side of the block surface. 4 reference measurements points, the position of the aperture is shown by the semi-transparent yellow band.

The presented four points of the scan irradiated a total of three pseudo-pixel columns, moving from the left geometrical border of one column to the center of the next one. As shown by Figure 3.26b and 3.26d, as the collimator aperture position is in front of the center of a pixel column, the whole pseudo-pixel surface is reconstructed: no difference is observed with respect to the same column in Figure 3.25b, obtained with the homogeneous irradiation. In case the aperture faces the border between two pixel columns (Figure 3.26a and 3.26c), the events are shared between the two. This could show a possibility of sub-pixel resolution for integrated measurements, which is anyway not reproducible on a single event basis. The same behavior has been verified with a vertical scan (shown from Figure 3.27a to Figure 3.27d); the collimator and table configurations have been kept unchanged, while the block has been turned of 90°.

In order to further confirm these results, a scan with reduced step size (1 mm) has been performed with the same collimator aperture, and no modifications have been detected in the spatial distribution of events for the steps centered on the same pseudo-pixel column. As before, when the collimator aperture faces the limit between two pseudo-pixels columns, the events are equally distributed on the two. 9 measurement positions for this 1 mm scan are shown from Figure 3.28a to Figure 3.28i.

All these set of data verify that the spatial reconstruction accuracy of the employed blocks is limited to the pseudo-pixel size, and a sub-pixel resolution is not achievable on a single event basis.

3.2.2.7 Pixel identification

The results of the pixel identification algorithm described in section 3.2.2.3 are shown in Figure 3.29. Figure 3.29a shows the identified average values of the pseudo-pixels positions on the two transverse dimensions. As already detailed in the description section, starting from these average positions, the single pseudo-pixels positions in rows and columns are extracted and the “valleys” between neighboring pseudo-pixels are used to define the grid shown in Figure 3.29b together with the pseudo-pixel center position map.

3.2.2.8 Pixel energy calibration

Once the pseudo-pixel positions and the related grid are defined, each interaction can be assigned to a single pixel. The energy spectrum of each pixel is then separately studied in order to equalize the energy response on a pixel basis.

The assignation method described in section 3.2.2.3 makes use of the dual pseudo-pixel position map shown in Figure 3.30. The position assignment scheme to pseudo-pixels is shown in Figure 3.31: a color has been given to each reconstructed point according to the pseudo-pixel region where it has been assigned by the described method. The method robustness is verified by the comparison of this map to the grid in figure 3.29b and 3.30.

In Figure 3.32 the results of the pseudo-pixel energy calibration are shown. Figure 3.32a (left) shows the overlap of the energy spectra for 60 pseudo-pixels before the energy calibration and

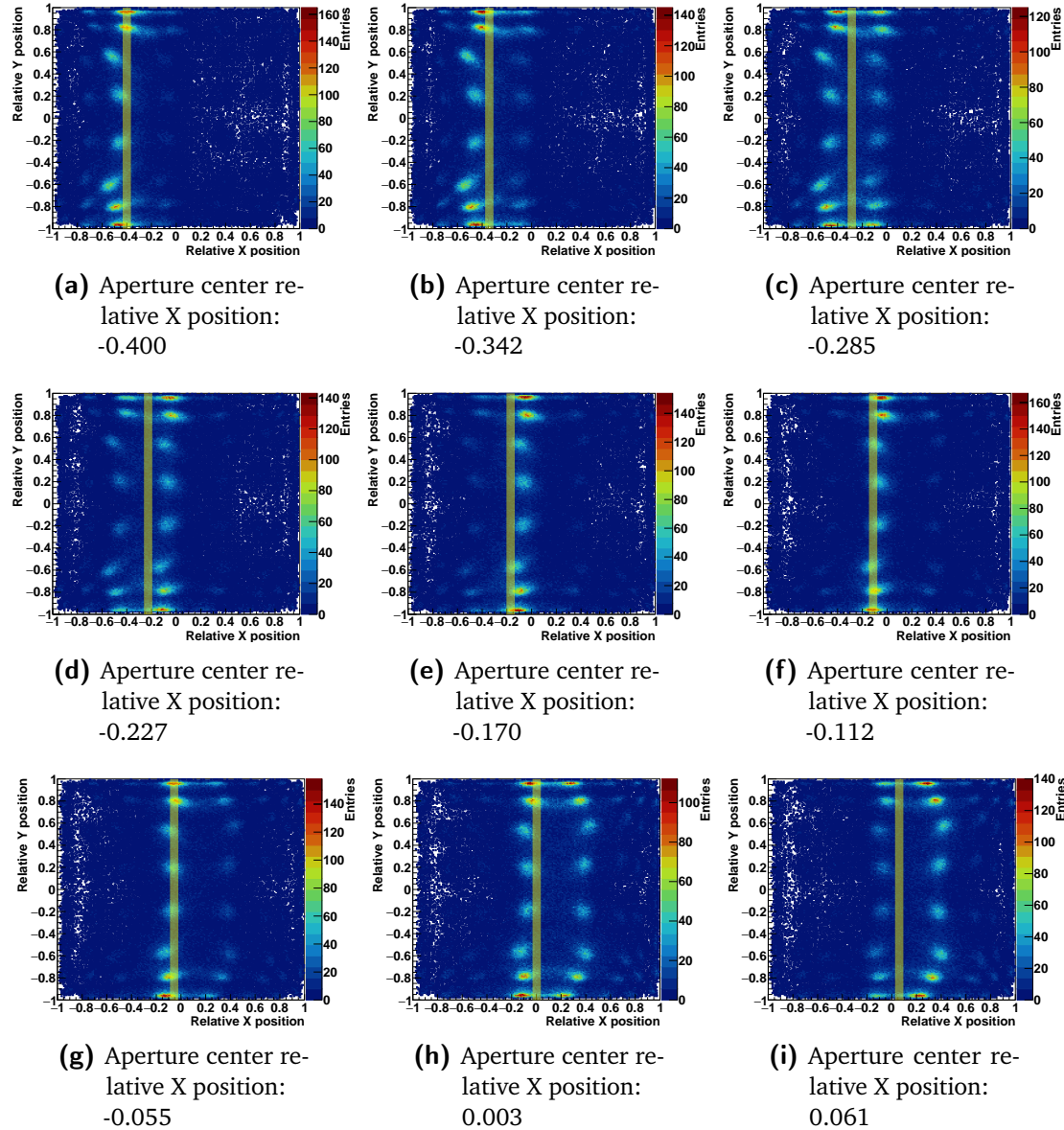


Figure 3.28: 2D reconstructed position maps during a 1-mm step scan performed with the ^{60}Co source with the line aperture. 9 reference measurements points, the position of the aperture is shown by the semi-transparent yellow band.

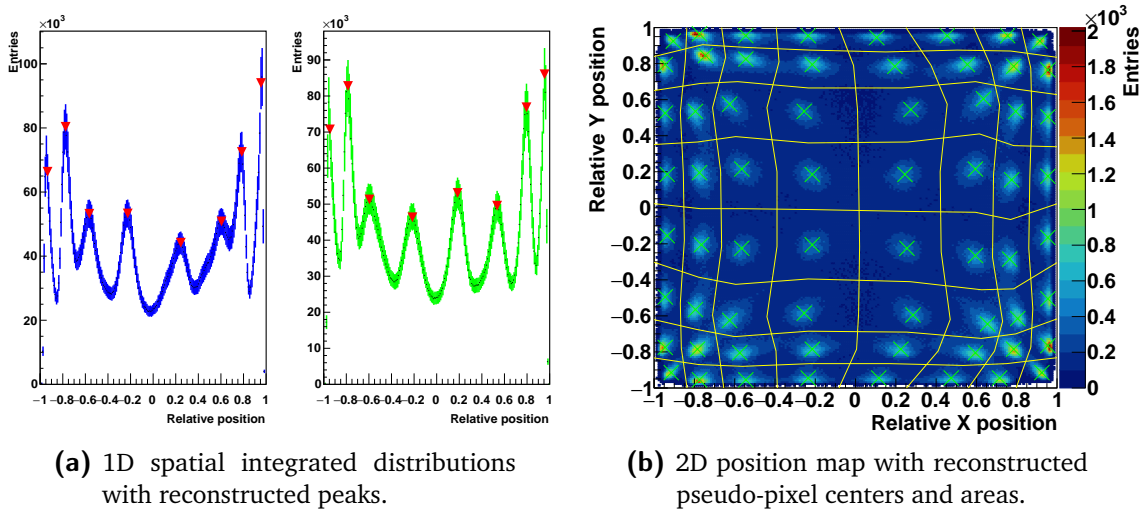


Figure 3.29: 1D integrated position distributions on the two transverse dimensions with the retrieved position of the pseudo-pixel average center (a). Reconstructed 2D map with the identified pseudo-pixels positions and surfaces.

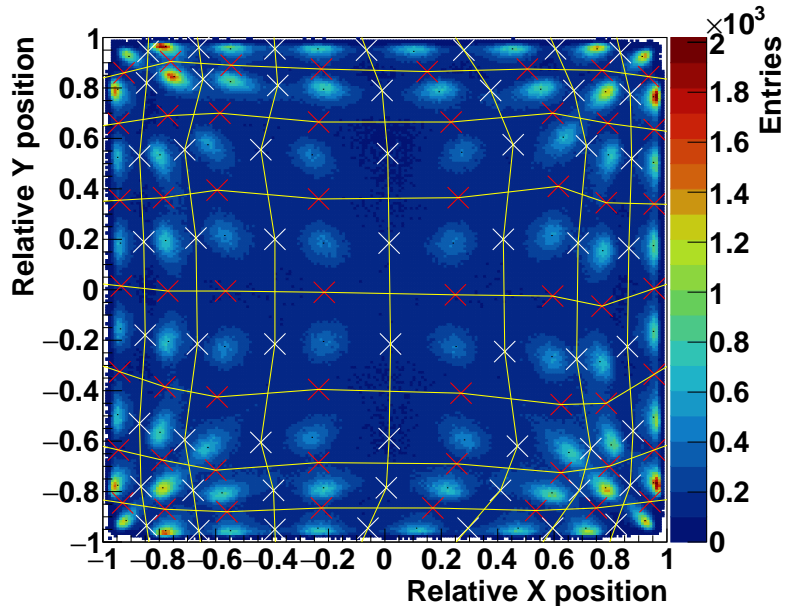


Figure 3.30: Auxiliary position map used for the assignment of the reconstructed events to a single pixel. The highlighted points represent the “valleys” between neighboring pixels on their separation borders.

equalization. The 4 pseudo-pixels on the corners show a very different energy response and are not included in this picture. This is probably due to a not complete light collection. The different response of each pixel to the two energy peaks is clearly visible. For each spectrum the low energy peak is assigned to 511 keV, while the high energy one to 1275 keV. In this way, the spectra are linearly calibrated and equalized, as shown in Figure 3.32a (right). For the 4 corner pseudo-pixels, the calibration is based only on the 1275 keV peak, while the 511 keV reference peak is substituted by the null ADC value.

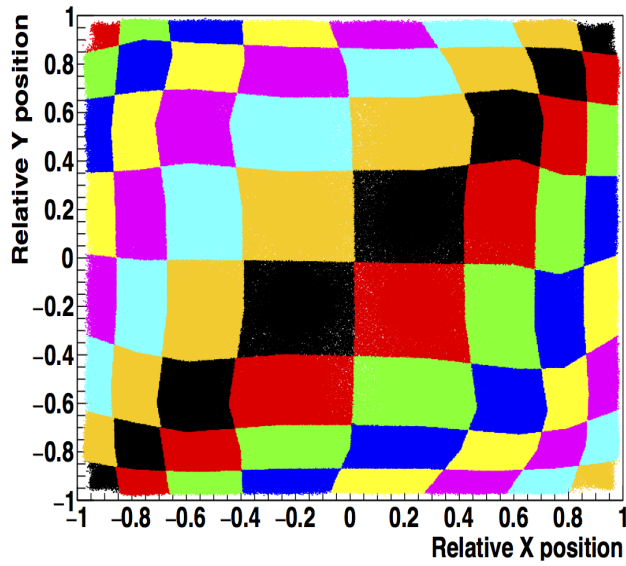


Figure 3.31: 2D map of the reconstructed event assignations to pseudo-pixels.

Once the single pixel energy responses are equalized and calibrated, the whole block energy spectrum can be derived with the sum of the all pixels. In Figure 3.32b (left) the ADC spectrum is shown before the equalization process, while in Figure 3.32b (right) the calibrated energy spectrum is presented. In Figure 3.32b (left) the energy spectra related to three reference position on the block surface are reported: this makes possible to appreciate the different contributions to the non-calibrated spectrum and the behavior of different block sections. The block peripheral pixels show an overall lower light collection and a lower efficiency in detecting high energy photons (reduced peak integral with respect to the center and mid-center pseudo-pixels). Concerning the central pixels, the slight in-homogeneity is probably due to the streaked structure which guides less than on the borders the scintillation photons.

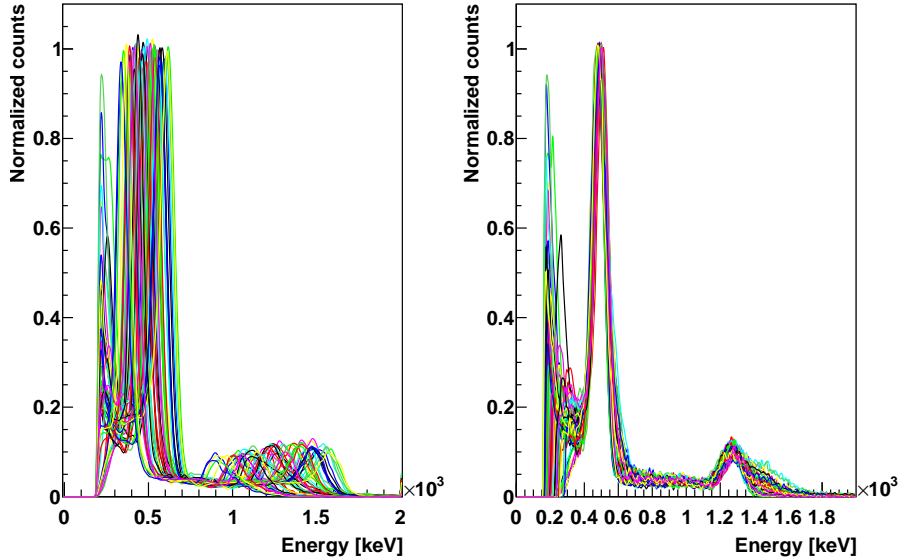
The two spectra are represented in logarithmic scale in order to better appreciate the calibration effect: it allows for the optimization of the energy response on the two spectroscopic lines of the ^{22}Na source. At this stage, the energy resolutions of the block can be defined as the FWHM of the two energy peaks.

In Table 3.1, the energy resolutions derived after the calibration process are compared to the raw ones, obtained by the non-calibrated data.

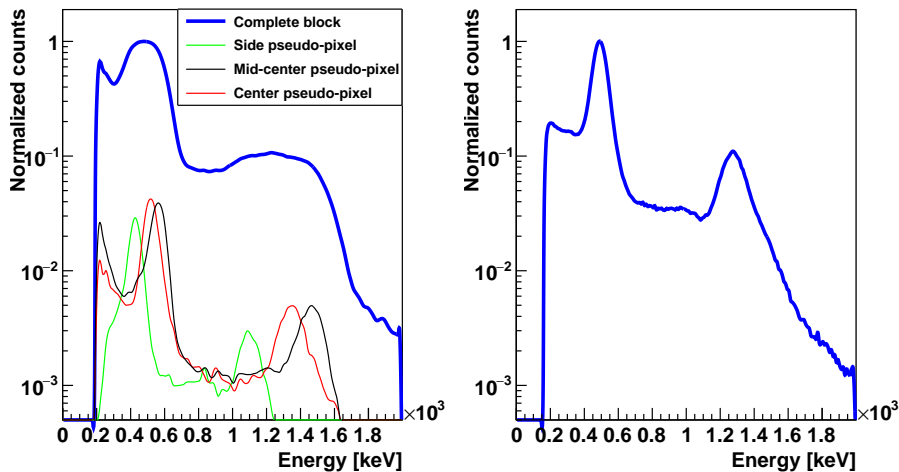
Table 3.1: Comparison of the results obtained with the two pixel-assignment methods.

	Energy resolution @ 511 keV FWHM [%]	Energy resolution @ 1275 keV FWHM [%]
Before equalization	46.12	39.43
After equalization	23.03	18.04

The results reported in Table 3.1 show the need for the implemented calibration process, which allows to optimize the BGO block spatial and energy response.



(a) Single pixel energy spectrum before (left) and after (right) equalization.



(b) Block energy spectrum before (left) and after (right) pixel response equalization.

Figure 3.32: Single pseudo-pixels (a) and whole block (b) energy spectra with the ^{22}Na source before (left) and after (right) the calibration process. The whole block spectra are reported in logarithmic scale. Three non calibrated spectra of pixels in reference positions (border, mid-center and center area) on the block are also reported with the non calibrated spectrum (a normalization factor has been applied for visualization purpose).

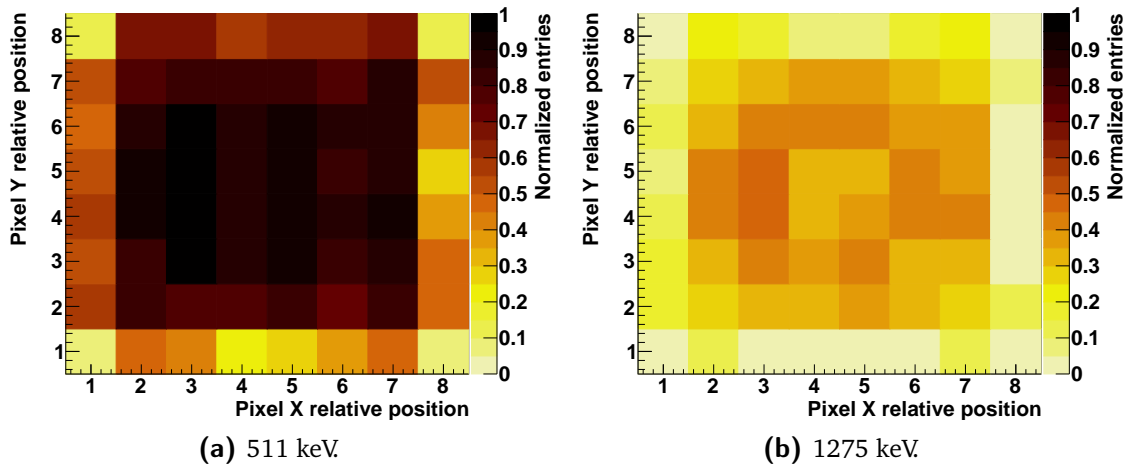


Figure 3.33: Relative number of entries for each pseudo-pixel as a function of the pixel relative position, represented by the row and column numbers (0 to 8 from left to right and bottom to top of the block surface). Figure(a) shows the entries in a selected energy window around 511 keV, Figure(b) in an energy window around 1275 keV. All the entries are normalized to the maximum collected number of entries, corresponding to 511 keV events in the central section of the block.

Thanks to the assignment of each reconstructed event to a single pseudo-pixel, the relative efficiency can be evaluated on a single pseudo-pixel basis. The two color maps in Figure 3.33 show the number of events collected by the 64 pseudo-pixels during the ^{22}Na source homogeneous irradiation, with an energy selection performed on the two photons energy emitted by the source (511 keV events in Figure 3.33a and 1275 keV events in Figure 3.33b). The entries are normalized to the maximum number of entries in a pseudo-pixel, detected for a 511 keV energy selection.

Figures 3.33a and 3.33b show that the expected homogeneous distribution of events over the whole block surface is confirmed for the central pseudo-pixels of central lines (1 to 6), while the block borders present a factor 2-3 lower detection efficiency. In particular, the pseudo-pixels on the 4 corners (line 0 and 7, pseudo-pixels 0 and 7), have an efficiency of a factor between 5 and 6 lower with respect to the center of the block surface. This effect is partially due to geometrical factors, given the fact that the side pseudo-pixels are slightly smaller with respect to the central one (as also shown by the reconstructed 2D map in Figure 3.29b). In addition to this, the light collection is probably less performing in case of photons interacting on the block borders, causing the loss of events. By comparing the two maps, an overall reduced efficiency for the detection of photons beyond 1 MeV is verified. This is expected given the factor ~ 2 difference in the photopeak efficiency of BGO at 511 keV and 1275 keV (Saint Gobain 2016). Moreover, the reduced efficiency in the central block area for 1275 keV photons can be related to the photo-multiplier tubes round geometry, which determines a dead space in the center of the block back surface (Uribe et al. 2003). The effect of the dead area is diminished by the light sharing effect at low energy, but it becomes considerable in case of deep-penetrating higher-energy photons. In order to fully understand the relative and absolute efficiency of each block section, an irradiation with a collimated source scanning the whole active area is foreseen. This will allow one to precisely define the detection rate variations on the block active area.

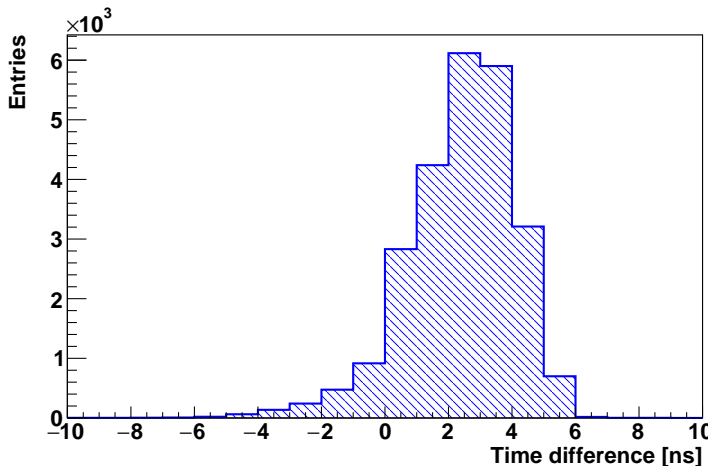


Figure 3.34: Distribution of arrival time differences between reference scintillator and BGO block.

3.2.2.9 Time characterization

Figure 3.34 shows the distribution of arrival time differences between the reference BaF₂ detector and the tested BGO block. The time resolution is defined as the FWHM of this distribution.

3.2.2.10 Results for the 30 blocks

In Table 3.2 the results obtained for the calibration and characterization of a set of 10 blocks are listed. The characterized blocks show very uniform results, with an average energy resolution of 25% FWHM at 511 keV and 20% FWHM at 1275 keV and an average time resolution of 4.42 ns FWHM tested with coincidences of 511 keV photons. Both the energy and time resolution are expected to be improved for the detection of photons in the prompt-gamma energy range, in particular above 1 MeV.

The last five blocks in the list of Table 3.2 showed detection problems, due to very low signal level on the read-out PMs or a poor spatial reconstruction accuracy with one missing pseudo-pixel on the two-dimensional map, probably due to crystal aging. The blocks with PMs issues will not be employed in the final absorber configuration, while the other two will be probably placed in the peripheral area in order to keep a wide active detection surface.

3.2.3 Hodoscope PMs characterization

The beam tagging hodoscope read-out is performed via 8 multi-anode PMs, Hamamatsu H8500 (Hamamatsu 2006), shown in Figure 3.10c. In order to guarantee a uniform response of the whole detector active area, composed of 256 scintillating fibers, the PMs must be previously characterized in terms of gain with a light source of fixed and known wave-length and intensity. The source selected for the measurements is a blue LED (Hewlett-Packard HLMP-CB), installed on the test-bench shown in Figure 3.35a and described in the following. The

Table 3.2: Calibration and characterization results for 10 tested BGO blocks.

BGO block ID	Energy resolution @ 511 keV FWHM [%]	Energy resolution @ 1275 keV FWHM [%]	Time resolution FWHM [ns]
Ref. block			
7627	23	18	4.0
3166	27	24	4.4
3171	23	18	4.4
3184	24	20	4.3
3232	24	20	3.6
3280	24	19	4.3
3322	25	20	4.2
3972	25	21	5.2
4368	25	20	5.3
5243	25	19	3.9
7130	24	21	4.9
7218	25	21	2.1
7240	25	20	6.7
7258	26	19	4.9
7369	23	19	4.3
7424	25	21	4.9
7581	26	23	4.1
7586	26	24	4.4
7601	24	19	4.1
7612	23	19	4.1
7624	22	19	3.9
7651	24	20	3.9
7657	24	19	2.7
14676	25	19	5.1
31210	25	21	4.8
3252	problem with PM 0		
3375	1 pseudo-pixel missing		
6823	1 pseudo-pixel missing		
7644	problem with PM 2		
7653	1 pseudo-pixel missing		
21097	problem with PM 2		
Complete set	25 ± 1	20 ± 2	4.5 ± 0.9

test-bench has been developed by the LPC AVIRM group (see [Gaglione 2013](#)) and adapted at the IPNL to a different acquisition system.

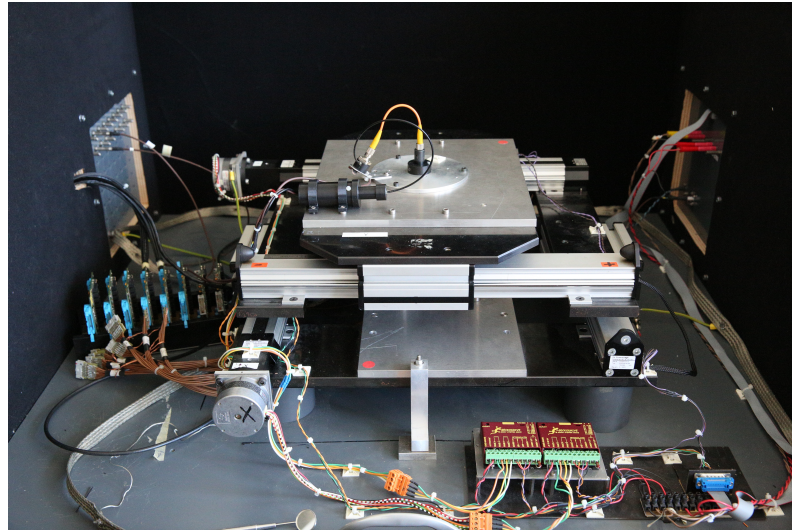
The goal of the characterization measurements is to trace a gain map of the whole PM surface, with the aim of storing calibration data to be used to both tune the PM working parameters (supply voltage and threshold) and correct the collected data. This is achieved by scanning the PM photo-cathode surface with the LED. The LED is so mounted on a motorized double-axis table, controlled by two G203V stepper modules provided by GeckoDrive Motor Controls ([GeckoDrive 2010](#)). The two axes have a total range of 20 cm each, and the step resolution achieved by the controllers is 20 μm . A metal support is set on the table in order to fix the LED. It produces light pulses synchronized with a pulse generator, which is also used as trigger signal for the acquisition system, as detailed later. The light pulse produced by the LED is split into two pulses with a 45°C mirror: one pulse is sent to the H8500 PM to be tested via optical fiber, in order to obtain a light beam perpendicular to the cathode surface (FWHM beam width estimated in 0.5 mm), the second one is detected by an Hamamatsu R5600 PM ([Hamamatsu 1995](#)), used as reference for the correction of temperature fluctuations. The PM under tests is fixed below the optical fiber output with a plastic support, not connected to the moving table. The whole described system is contained in a black box for external light shielding.

The output signals from the H8500 PM are initially amplified by custom pre-amplification cards: 8 cards are available and have been characterized in terms of amplification gain. Once amplified, the signals of the H8500 PM, together with the output of the reference PM, are sent to the acquisition system composed of a National Instrument PXI Express 1082 ([National Instruments 2010](#)) equipped with two 8-channel flash ADC modules (NI PXI-5105) and a two-channel ultra-fast digitizer (NI PXI-5154). The flash ADC modules have a maximum sampling rate of 60 MHz and are used for the read-out of the H8500 PM signals, while the ultra-fast digitizer, able to sample at a frequency up to 1 GHz, is used for the reference PM.

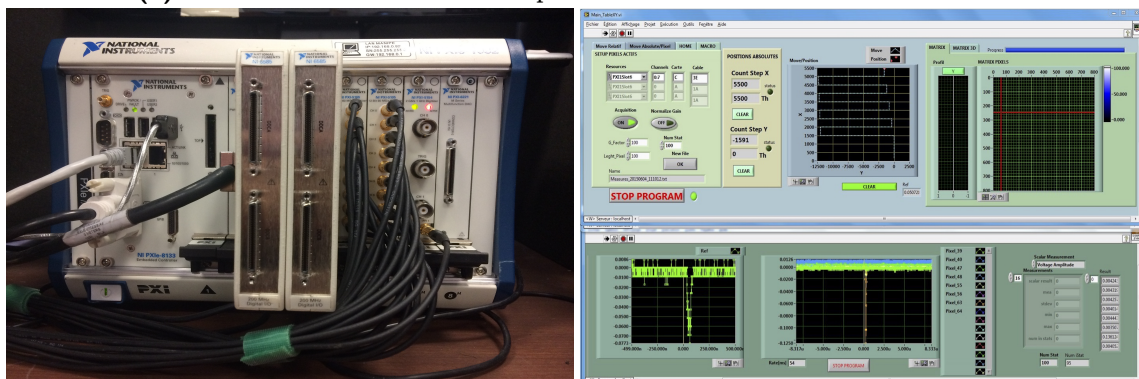
The acquisition and control software is developed with LabVIEW (2009) installed on the PXI; a picture of the software user interface is shown in Figure 3.35c. The PXI receives the signals from the two PMs and is also connected to the table stepper modules, so that the LabVIEW software can handle and synchronize data acquisition and table movements. The table movements can be automatized via LabVIEW macros, where step size, number and direction are stored and then used for the acquisition. The acquisition trigger, as mentioned, is given by the pulse generator which also control the light pulses of the LED; in this way, a fixed number of pulses per table position can be recorded, and the measurement process is completely automatic. During the acquisition, the LabVIEW software automatically corrects the collected data according to the reference PM signal amplitude and to the pre-amplification card gain.

Given the limited number of flash ADC channels, only 16 PM pixels can be characterized per acquisition; four acquisitions are needed to scan the complete PM surface.

Each performed acquisition is set to scan a matrix of 4×4 PM pixels, and safety margins are arranged on the PM sides in order to ensure a complete surface irradiation. As shown in the schematic view of the PM in Figure 3.36a, the total PM size is $52 \times 52 \text{ mm}^2$, for an active area of about $49 \times 49 \text{ mm}^2$. The active area of the pixels on the borders is slightly wider than the central ones. In order to optimize the measurement process, a preliminary analysis has been done for the definition of the needed step length, and the details are reported in [Coudurier 2015](#). A trade-off between measurement accuracy, required time and stored data file size



(a) Overview of the test-bench setup for the Hamamatsu PM characterization.



(b) National Instruments PXIe acquisition system.

(c) Example of LabVIEW software interface for the Hamamatsu PMs characterization.

Figure 3.35: Test-bench and tools for the characterization measurements performed on the Hamamatsu PMs of the beam tagging hodoscope.

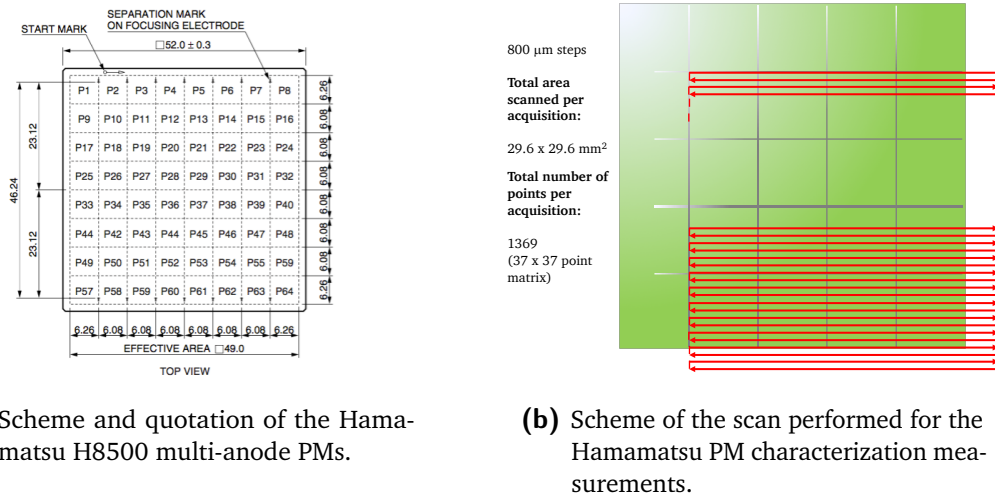


Figure 3.36: Details of the hodoscope PMs and of the performed characterization measurements.

has been found with a step of 800 µm, so that each pixel is scanned with approximately 64 measurement points and the transition between neighboring pixels can be appreciated. A schematic of a table reference movement is presented in Figure 3.36b. To be noticed that for each irradiated point, 100 LED pulses are sent to the detector and the average amplitude value is calculated and collected.

The 8 Hamamatsu PMs have been completely scanned without the optical fiber mask used in the hodoscope and shown in Figure 3.10d, and the results are shown here for one reference PM. Some tests have been also performed with the fiber mask, in order to test the PM response mainly in terms of expected cross-talk between neighboring pixels. A complete result database has been created for calibration purpose.

Figure 3.37a shows the two-dimensional maps of a reference PM response for a complete irradiation, obtained with four separated acquisitions without the plastic fiber mask. Figure 3.37b shows the response of the same PM with the plastic fiber mask fixed on its surface. The reported signal amplitude has been normalized to the reference PM Hamamatsu R5600 for temperature oscillation correction, but the relative difference between the two irradiation is maintained to show the signal attenuation caused by the fiber mask, resulting in a factor 3-4 depending on the pixel.

In Figure 3.38 the two-dimensional response map for the 8 PMs are shown. In order to obtain a visual uniformity, the amplitude values have been normalized to the maximum value of each PM. We can observe response dis-uniformity on each PM surface, estimated in a factor ranging between 2 and 3. The retrieved response of each pixel will be useful for the calibration of the hodoscope final acquisition chain, in particular for what concerns the electronics FE settings (threshold and gain of each channel). In addition to this, these calibration measurements will allow for a proper data correction at the analysis stage.

The irradiation performed with the fiber plastic mask are also used to study the signal cross-talk between neighboring pixels, which is expected to be negligible according to the provider specifications, given for similar measurements and shown in Figure 3.39a. The analysis results for one of the studied PMs are shown in Figure 3.39b as reference.

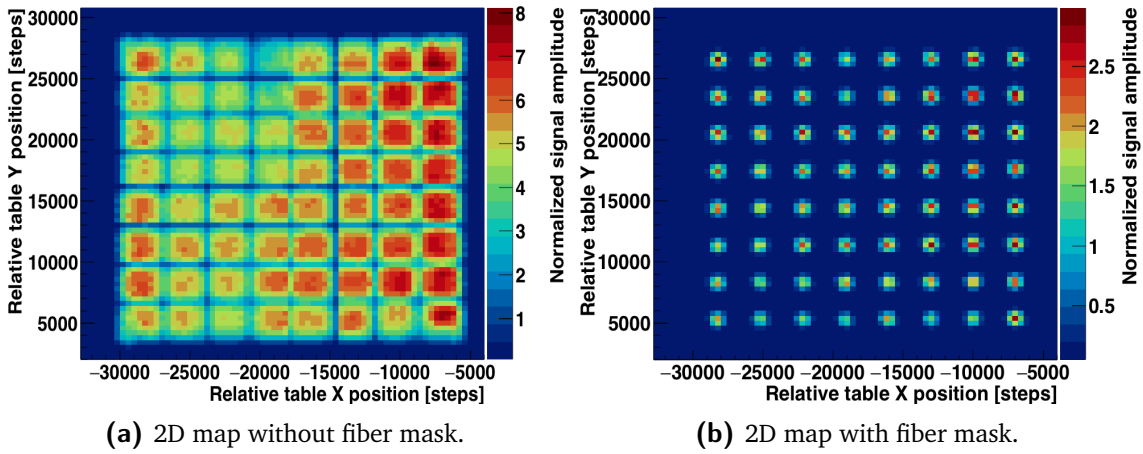


Figure 3.37: Two-dimensional response maps of one of the Hamamatsu PMs for the scintillating fiber hodoscope readout, obtained with the irradiation with a blue LED. The signal amplitude is normalized to the reference PM response.

The retrieved cross-talk is more important with respect to the provider specifications (to be noticed that the measurement conditions are slightly different), but always below 3% for the tested anodes. This cross-talk level is negligible and can be easily suppressed by a proper threshold setting.

3.2.4 Hodoscope fiber test with electron source

After the complete characterization of the Hamamatsu multi-anode PMs, they have been installed in the black boxes connected to the optical fibers of the hodoscope prototype, and the complete detection chain have been qualitatively tested to check the scintillating fiber light transmission to the optical fibers and to the read-out PMs. The observations have been performed by directly checking the pre-amplified PM output signal (with the same custom cards mentioned in the previous section) on an oscilloscope. A mechanical intervention has been necessary to fix some of the optical fibers not properly pasted to the plastic mask on the PM surface. In addition to this, a layer of black silicone has been added on the plastic mask surface to improve the light isolation on the only side where it is impossible to place the isolating black tape.

The hodoscope prototype has been then tested with a beta source (^{90}Sr) for verification, and the obtained signal distributions (retrieved as before with an oscilloscope acquisition after signal pre-amplification) have been compared to simulation study performed by an internship Master 1 student (Vallois 2016). He tested in simulation the irradiation of the whole hodoscope surface with an equivalent ^{90}Sr source to retrieve the deposited energy distribution on the scintillating fibers. This distribution can be compared to the collected signals amplitude distribution obtained with the experimental tests, in order to calibrate the relationship signal amplitude-deposited energy. The distance between the source and the fiber was set to 3 mm in the simulation code, to reproduce the gap created by the plastic box of the real source, which was directly on the fiber for the experimental measurements. In Figure 3.40 the results

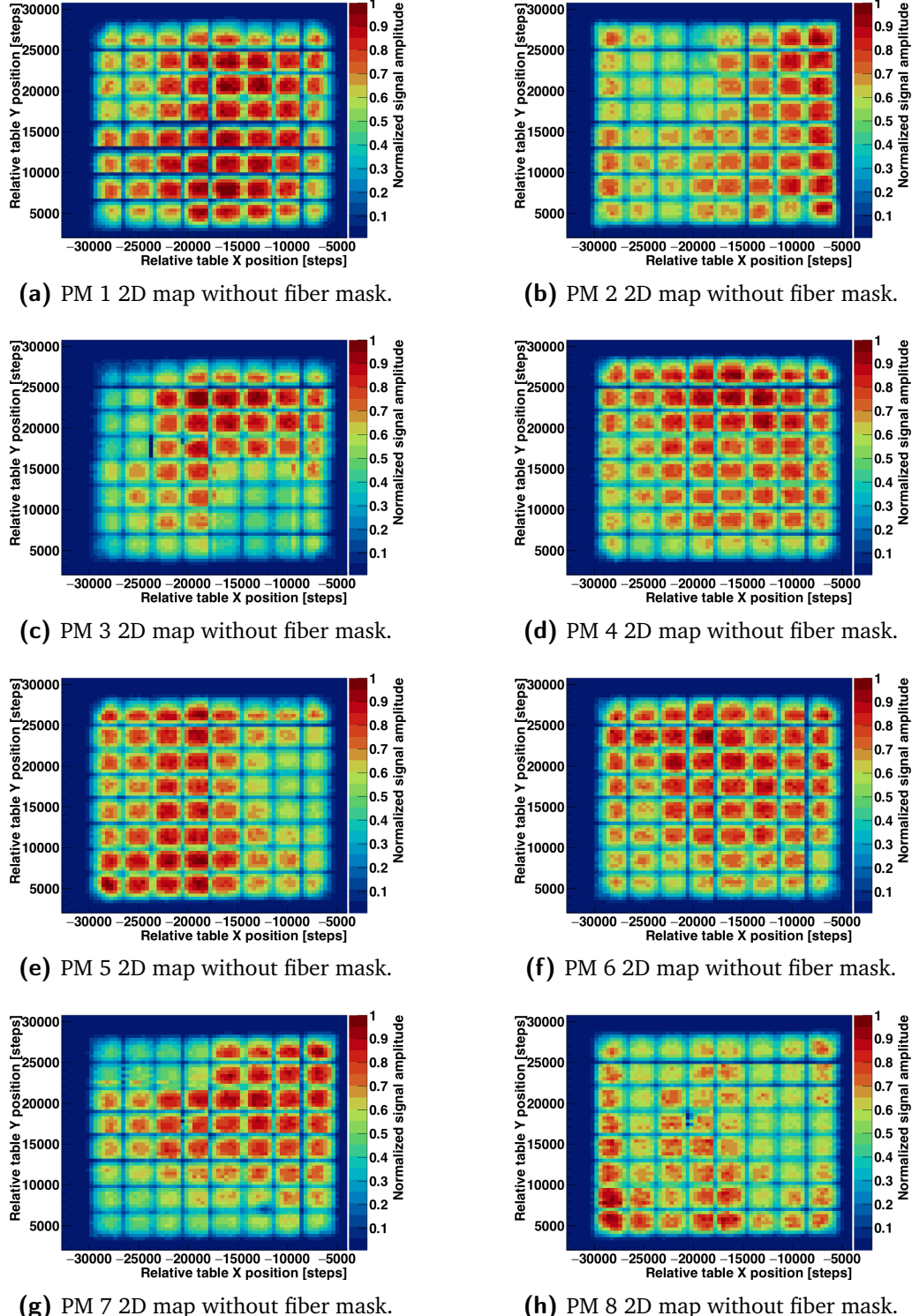
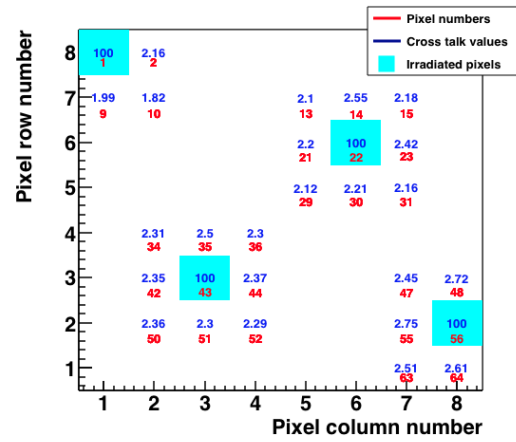


Figure 3.38: Two-dimensional response maps of the Hamamatsu PMs for the scintillating fiber hodoscope readout, obtained with the irradiation with a blue LED. The signal amplitude is normalized to the reference PM response and then to each PM maximum detected amplitude.

●Measured by using a fiber

 FIBER SIZE: 1.0 mm Dia. (Kuraray; Clear Fiber NA=0.72)
 LIGHT SOURCE: W-LAMP (W/BLUE FILTER)

	P1	P2	P3	P4	P5	P6	P7	P8	
P1	100	1.3	—	—	—	—	—	—	P8
P9	1.4	0.3	—	—	—	—	—	—	P16
P17	—	—	0.1	0.8	0.2	—	0.2	1.2	P24
P25	—	—	0.5	100	0.7	—	0.7	100	P32
P33	—	—	0.1	0.9	0.2	—	0.2	1.2	P40
P41	—	—	—	—	—	—	—	—	P48
P49	—	—	—	0.3	1.3	0.3	—	—	P56
P57	—	—	—	2.0	100	2.0	—	—	P64
P57	P58	P59	P60	P61	P62	P63	P64		



- (a) Signal cross-talk provided by Hamamatsu for the PM H8500 (Hamamatsu 2006). The measurements have been performed with a 1 mm diameter optical fiber; the irradiated anode is in the light blue box, and the cross-talk on the neighboring ones is expressed in %.

- (b) Signal cross-talk on a reference PM measured with a blue LED irradiation through the plastic fiber mask. The irradiated anode is in the light blue box, and the cross-talk on the neighboring ones is expressed in %.

Figure 3.39: Cross-talk study on neighboring PM pixels. The experimental results obtained with the irradiation with a blue LED through the plastic fiber mask on a reference PM (right) are compared to the specifications provided by the producer, measured in similar conditions (left). The cross-talk is expressed in % with respect to the irradiated anode, which is represented by the light-blue cell with 100% of the signal.

for a reference fiber are shown. The distribution entries have been normalized to the total number of events for visualization purpose.

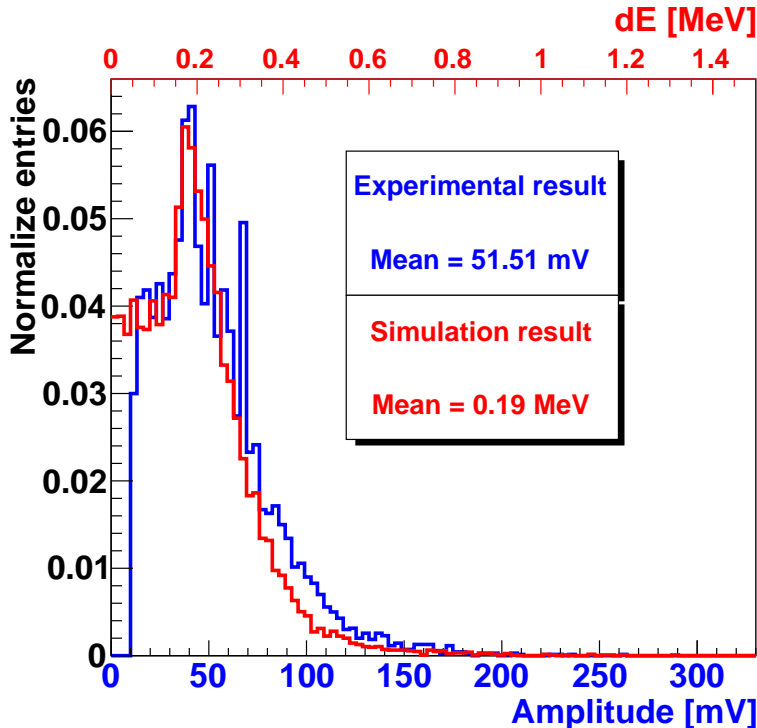


Figure 3.40: Comparison of the simulated distribution of energy deposited by electrons from the ^{90}Sr source on a single hodoscope fiber to the experimental signal amplitude distribution from a scintillating fiber irradiated with the ^{90}Sr source.

The comparison presented in Figure 3.40 can be useful as estimate of the expected signal for a given energy deposited by a ionizing particle (about 50 mV for about 200 keV of energy deposited). Knowing the applied amplification factor (given by the per-amplification card characterization) and the relative gain of each PM pixel, the expected raw signal integral can be estimated.

A complete characterization of the hodoscope acquisition chain will be necessary on proton and carbon beams in order to verify the beam primaries energy deposit on the scintillating fibers and tune the working parameters. In particular, the increased energy deposit expected for proton and carbons with respect to electrons should allow for a reduction of the high voltage applied to the PM. With reduced voltage, the detection rate capability would be improved. All these assumption will be tested on beam in the next future.

ADD HERE THE RESULTS OF THE SUMMER ABOUT THE ASIC GAIN AND THRESHOLD CHARACTERIZATION, AND COMMENT LINKING TO CHAPTER 6 FOR THE BEAM TESTS.

3.3 Summary and perspectives

The CLaRyS collaboration is developing in parallel two gamma cameras for ion beam therapy monitoring and nuclear medicine applications. At present, the detector components are be-

ing tested separately for characterization purposes at the IPNL. I presented in this chapter a complete description of the detector components with the related FE electronics, mechanical support, acquisition system and software tools, together with the all the characterization measurements I performed on the various detector sections. In the following, in addition to a short summary of the present status of the instrumental development of each camera component, I list the main task to be accomplished for the final integration a complete operation of the whole camera.

3.3.1 Silicon scatterer

Among the 10 DSSD layer provided by the seller, only 7 respected the design requirements and have been selected for the use in the Compton camera prototype. The 7 selected layer have been characterized in terms of leakage current with an acquisition system specifically developed for this purpose. Temperature cycles have been performed in order to precisely define the cooling performance needed to obtained the required noise level. These measurements allow to fix the working temperature to -20°C and lead to the conception and production of a thermal regulated box, working with cold air and so adapted to the clinical use. A modular mechanical support has been fixed inside the camera to sustain the silicon layers with their FE cards. The FE card has been designed and tested at the IPNL, and includes a custom ASIC which have been optimized with three different developed versions. The final version of the whole board have been produced in 7 copies in 2017 and they are now available for the next test stages.

The development of the FE board firmware is at present ongoing at the IPNL, and the first tests of data collection with a temporary acquisition system and injected charges have been performed. A further verification and optimization of the code will be carried out in the next future, and the silicon layers will be tested with their FE cards by the end 2018 with the μ -TCA acquisition system. The present AMC40 firmware performance has never been tested with the scatterer detectors before; some modifications can then be foreseen to optimize the data taking process, for what concerns both the stand-alone test mode and the operation within the complete system.

Moving to the thermal regulated box, its cooling performance has been tested without the detectors, so that a test with the power consumption of the seven operational detectors and boards has still to be performed. Additionally, the box has to be adapted to arrange the incoming and outgoing cables (power supply and data). Outside the box, a patch-panel will be also realized in order to properly set all the needed connections. The patch panel will be conceived to be integral to the box and adapted to the camera moving table, where the box will be installed for the final camera integration.

Once the acquisition will be fully operational, laboratory measurements with gamma sources are foreseen to characterize the detector response. Low energy gammas will be employed to test the DSSD energy resolution with full gamma absorption on a single strip basis, on p and n sides, while higher energy gamma irradiation is foreseen to study realistic detection conditions and verify efficiency, time and spatial performance (time resolution, average cluster size as a function of the energy). Once a full characterization of each channel of the 7 layer will be achieved, tests on beam with prompt-gammas are planned in stand-alone operation and, finally, with the complete Compton camera.

3.3.2 BGO absorber

As mentioned in the detector description section, the original camera design included 96 BGO blocks recovered from a dismantled SIEMENS PET system. The reconditioning process aimed to re-polish the crystal surfaces, tests the PMs with a light source and group them in quartets with compatible gains. As reported, the reconditioned block prototypes tested didn't show the expected improved performance, but on the contrary an overall signal degradation has been observed, probably due to a worsened light collection. Several configurations have been tested with non satisfactory results, so that the present camera is set up with 30 original blocks, which have been deeply studied and characterized at the IPNL, as detailed in section 3.2.2. The calibration and characterization method developed for the BGO block can be applied to similar detectors and represents an extension of previous studies (Golnik 2015; Hueso-González et al. 2015; Rogers et al. 1994; Tornai et al. 1994). Some of the features developed for the characterization tests, as the automatic research of the pseudo-pixel position and the pseudo-pixel assignation algorithm, will be used in the final camera at the data analysis stage, with simple adaptation to the camera acquisition system and data format. The complete set of characterization measurements described in this chapter have been performed with commercial acquisition systems and the required raw data treatment was performed with commercial NIM modules. The ASM red-out boards are at present under test at the IPNL, and their firmware must be optimized for the μ -TCA acquisition. Once ready, the complete acquisition chain will be tested, including the pre-trigger logic with the THOR board, the μ -TCA data collection and communication to the acquisition PC.

With a fully operational absorber, test with prompt-gammas (and so on proton and carbon beams) will be performed to test the block behavior in the prompt-gamma energy range, where an overall performance improvement is foreseen (in terms of space, time and energy resolution). Some tests performed at the GANIL in 2014, with an original block and an acquisition similar to the one employed for the characterization tests, showed promising results: in particular, a 2 ns FWHM time resolution was achieved with prompt-gammas (see Ley 2015). These results have to be verified with all the camera BGO blocks. Moreover, a first prototype of multi-slit collimated camera will be tested on beam with the final acquisition, and the coupling to the hodoscope is foreseen to perform the first TOF measurements. In addition to this, with proton and carbon beams the absorber geometry (in terms of block arrangement in the mechanical support) will be tested to obtain the optimal configuration with the minimization of dead areas between the blocks. To be noticed that different geometrical setup can be foreseen for Compton and multi-collimated camera, and for the peculiar desired measurement (detection of the all ion range, test of prompt-gamma distribution in the plane parallel to the beam line, etc.).

Concerning the mechanical support, it is finalized and already prepared for the integration on the moving table. As for the scatterer, a patch panel will be realized to arrange all the cables which have to be connected between FE and ASM cards. The 5 needed ASM cards will be placed in a dedicated VME crate, which will be integral to the table. Its setup will be fixed in order to minimize the interference with the table movements.

MODIFY HERE ACCORDING TO THE SEPTEMBER TEST! LINK TO CHAPTER 6

3.3.2.1 Absorber upgrade

One of the already identified main limitations of the Compton camera for the application in ion beam therapy monitoring at clinical beam intensity is the relevant background due to random coincidences. As already mentioned, the random coincidences can be created by secondary particles different from prompt-gammas, or, less likely, by two prompt-gammas in the same time window. The TOF solution has been verified to be efficient in reducing the first kind of random coincidences, and the background subtraction performance ensured by this method strongly relies on the detector time resolution. An improvement in the camera component time resolution would allow for a reduction of the coincidence window, further increasing the amount of rejected random coincidences.

A possible upgrade of the absorber detector has already been considered for a second version of the Compton camera prototype, and involves a commercial detector provided by Damavan Imaging, called Temporal Delta Compton. It is based on a scintillation LYSO or CeBr₃ crystals coupled to very fast Philips DPC3200 Tile sensors, with a SPTR of the order of 100 ps (Brunner et al. 2016). This excellent time resolution allows for a direct measurement of the scintillation light shower development within the crystal, resulting in the possibility to retrieve a 3D spatial information in parallel to a time resolution in the hundred of ps scale. This solution will be further discussed in the future and can be applied for a second prototype of the Compton camera.

3.3.3 Scintillating fiber hodoscope

Three prototype of scintillating fiber hodoscope are available at the IPNL: 1×1 fiber, 32×32 fibers and the large size version with two planes of 128 fibers. The 1×1 fiber has been studied at the beginning of the development process as proof of concept, and the employed technology has been transferred to the two final prototypes with the required improvements. The increased size of the 128×128 fiber one lead to the addition of the two-sied fiber read-out, for efficiency optimization and improved timing performance. All the other features are common to the two, including the installed multi-anode PMs (Hamamatsu H8500) and the related FE card. The advantage of the 32×32 hodoscope is the possibility to perform a complete read-out of the active surface with a single FE card, so that no synchronization features are required in the card and acquisition firmwares. This is the main reason why the first beam test performed on the hodoscope have been carried out with the small version (see chapter 6 for the description and the results of the beam tests). The FE card firmware is at present at the optimization stage, and the performed test allowed to define the needed improvements, mainly connected to the time measurements capabilities. In addition to this, the synchronization of the 8 cards used for the read-out of the 128×128 fiber prototype must still be achieved. The first acquisition tests performed during the proton beam exposure allowed to validate the acquisition software and the μ-TCA firmware in a simple version, but additional trigger features must still be added to integrate the hodoscope in the final camera configuration. Concerning the detector performance, the optimization of the working parameters (gain and threshold of each read-out channel) required the development of an automatic measurement system, which will be employed on beam to perform similar characterization in presence of proton induced signals. Finally, the mechanical support is fully operational: the motor steering must be integrated in the slow-control software.

The overall development is at the final stage, and the integration of the hodoscope in a first multi-slit collimated camera configuration is foreseen, as mentioned, in order to perform preliminary test of TOF background rejection capabilities.

MODIFY HERE ACCORDING TO THE SUMMER RESULTS AND SEPTEMBER TEST

3.3.3.1 Hodoscope upgrade

As already explained concerning the absorber possible upgrade, the main direction for an improved camera prototype is the optimization of the detector timing capability. The LPSC group in Grenoble is developing high time resolution diamond detectors, which can be considered for a new version of the beam tagging hodoscope. The so-called MoniDiam project aims to develop a diamond based hodoscope prototype with the related fast electronics to enable a time resolution of a few tens of ps. In addition to this, the diamond based detectors are intrinsically affected by a very low noise level and allow to overcome the radiation hardness limitation imposed by the present scintillating fiber prototype, together with further extending the rate capabilities to an expected 100 MHz acquisition rate. Some tests of small diamond detector prototypes have already been performed with pulsed beams at the ESRF in Grenoble and with 95 MeV/u carbon beam at the GANIL, with promising results: a polycrystalline detector, $5 \times 5 \times 0.3$ mm³, exposed to the 95 MeV/u GANIL carbon beam, showed a time resolution of 37 ps RMS coupled to an energy resolution of the order of 7% RMS for 25 MeV of deposited energy (see [Gallin-Martel et al. 2016](#)). Similar measurements performed with diamond crystal with different sizes showed compatible results, with a time resolution between 20 and 90 ps RMS and an energy resolution between 7 and 9 % RMS ([Gallin-Martel, M.-L. et al. 2018](#)). A large area prototype of 15×15 cm² is expected to be tested in 2019 and is a good candidate for a improved versions of the Compton and multi-collimated cameras.

3.3.4 Acquisition and software

The acquisition μ -TCA based system development is managed by the CPPM research group, and frequent tests has been performed at the IPNL to verify and integrated its functionality to the read-out detector cards. As reported in the description, it should be able to receive and treat the trigger signal generated by the absorber for the multi-collimated camera or by the silicon scatterer for Compton one, collect the data flow from all the detectors, group them into UDP packets with the proper format and send them to the acquisition PC. The main tasks (data collection, packet creation and communication to the PC) have been already verified on beam for a single detector and a single FE board, so that now the trigger treatment capabilities and the ability to handle all the detectors components have to be developed in the AMC40 firmware and tested with the final system. Moreover, the μ -TCA must also be able to transfer the slow control signals sent by the LabVIEW software to the selected read-out cards; this feature is still at the debug stage.

Concerning the acquisition software, it has already been tested and validated with a data simulator, with a maximum achieved acquisition rate of about 300 Mb/s, sufficient to manage the data from the complete camera (see appendix A). It will be tested step by step with the increasing number of FE boards involved in the measurements. In parallel, the monitoring software is

now available and operational for each single detection section, but an optimize version allowing for an on-line visualization of the whole camera acquisition must still be studied. Finally, the slow control software development is ongoing; all the required working parameters can already be controlled by different pieces of software, which must be integrated in a complete user interface and tested with the μ -TCA for what concerns the FE cards configuration. All the parameters related to the moving table motors (for camera and hodoscope), detector and card low and high voltage, have already been tested and do not require the μ -TCA intervention.

3.4 Conclusion

During the three years of my PhD thesis, the instrumental development of the single detector components, as well as of the two cameras, saw an important advancement, thanks to the synchronized effort of the whole collaboration. The project is now reaching the final stage, where all the performed laboratory test and development studies will be transferred to the multi-collimated and, even most, to the Compton camera, which is foreseen to be tested on beam before the end of 2019. The next two years will be fundamental to estimate the potential of the developed detectors in realistic conditions and to plan the first clinical tests, final goal of the entire project.

4

Compton camera application for ion beam therapy monitoring

5

Compton camera application in nuclear medicine

Most of the results presented in this chapter have been published in (Fontana et al. 2017a) and (Fontana et al. 2017b).

Contents

5.1	Introduction	80
5.2	Material and methods	81
5.2.1	Radioactive sources	81
5.2.2	Compton camera simulation and data analysis	81
5.2.3	Anger camera simulation and data analysis	85
5.2.4	Figures of merit for the comparison study	89
5.3	Results: Compton camera study for SPECT application	92
5.3.1	Influence of Compton camera scatterer detector energy resolution	92
5.3.2	Compton camera coincidence study	93
5.3.3	Compton camera desing study	94
5.4	Results: Benchmark of Compton camera and Anger camera performance	95
5.5	Summary and discussion	98

5.1 Introduction

SPECT is one of the most widespread techniques for nuclear medicine diagnostics examinations. In most of the clinical cases, a radiotracer is injected in the patient and the emitted γ -rays are collected by scintillating detectors coupled to physical collimation systems. This process leads to the reconstruction of a planar transmission image. Such a kind of imaging tool relies on the first idea proposed by Hal Anger ([Anger 1958, 1964](#)), and it is now commercially available in different variants with peculiar features and applications. A complete system is often composed of at least two rotating detection heads, allowing a tomographic data acquisition and the reconstruction of a three-dimensional image of the radio-tracer distribution (see chapter 1 for further details).

The main consequence of the collimation system is a forced trade-off between sensitivity and spatial resolution: The spatial resolution is completely determined by the collimator geometry, and it can only be increased by reducing the collimator hole size, at the expense of a reduction in the detector sensitivity since fewer photons survive the mechanical selection. Moreover, the collimator thickness and septa limit the primary energy acceptance, and the performance of Anger cameras generally downgrades as the energy increases.

In order to overcome this mechanical collimator limitation, it is natural to move towards an “electronic collimation”, where the emitted photons are tracked and the emission point is reconstructed via Compton kinematics, and so to the application of Compton cameras in this field ([Everett et al. 1977; Singh 1983](#)).

L. Han and colleagues ([Han et al. 2008](#)) have performed a simulation work comparing a standard Anger camera and a Compton camera prototype for a fixed source energy of 364 keV (^{131}I gamma ray emission). The expected enhanced detection efficiency associated to the Compton camera with respect to the Anger system was estimated to a factor 20 at the tested energy, while the spatial resolution was compared for equal imaging time.

Starting from the results of Han and colleagues, we tested in simulation the performance of the CLaRyS Compton camera prototype (see chapter 3) for the application in SPECT. The aim of this simulation work consists in extending the aforementioned study to a wide energy range, with simplified analysis methods. The CLaRyS prototype is compared to the Infinia Anger camera delivered by General Electrics Healthcare ([GE Healthcare 2006](#)). The detector performances are compared in terms of efficiency and spatial response with the exposure to mono-energetic point-like radioactive sources at different energies, ranging from 245 keV to 2.614 MeV. The noise components related to the target (patient), such as photon attenuation, photon diffusion, patient movements, are common for both detectors and not considered in this context.

It should be noticed that the Compton detection principle requires coincidences between the two detector sections (scatterer and absorber), so that the random coincidence rate plays a fundamental role in the complete system performance, like in PET machines. The effect of these random coincidences will therefore be investigated. Moreover, a reliable Compton scattering cone reconstruction requires a precise energy resolution for the scatterer section of the detector. The influence of this parameter will be studied. Finally, the Doppler broadening effect will be quantified to give the physical limits of the Compton imaging technique knowing

that silicon corresponds to the lowest Z material available for gamma detection with precise energy resolution. A comparison with a different possible scatterer material is also performed for verification.

All the obtained results are discussed with direct reference to (Han et al. 2008), focusing on the possible advantages offered by the use of a Compton camera (in particular the CLaRyS prototype), which intrinsically introduce the possibility to update the clinical standards in terms of source kinds, energies and activities, examination duration, patient dose, imaging techniques.

5.2 Material and methods

In this section, the sources of gamma rays simulated for the study are presented and discussed and the two simulated systems are described in detail, as well as the proposed analysis techniques. In addition to this, some comments are given about the criteria chosen to represent a relevant comparison between the two investigated detectors.

5.2.1 Radioactive sources

Both simulated systems have been exposed to monochromatic point-like gamma sources in air. The performance of the two cameras has been studied in terms of spatial resolution and detection efficiency as a function of the gamma source energy, related to actual radioemitters, already used in clinical practice or suggested for this kind of application in previous works (Nurdan et al. 2015). The explored energy range was chosen having in mind the possible clinical usage of Compton systems like the one developed by the CLaRyS collaboration, to extend the present field of application of SPECT imaging.

In Table 5.1, the characteristics of the considered radioactive sources are given. Most of the sources do not emit gamma rays at a single energy, but only the ones selected for this study are presented in the table, together with the related branching ratio.

5.2.2 Compton camera simulation and data analysis

5.2.2.1 Simulation settings

The simulation code for the Compton camera was developed with GEANT4 v.9.6 and the camera design is based on the specifications of the prototype at present under development by the CLaRyS collaboration, detailed in chapter 3. It should be noticed that the real size of the detector components slightly differs from the ones reproduced in simulation, which have been used in the code for simplicity. The geometric setting of the camera has initially been optimized for the application in ion therapy monitoring via prompt-gamma emission (see chapter 4) and has been adapted for SPECT for this study in order to maximize the similarities between the two systems (Compton and Anger camera) in terms of detector acceptance, as

Table 5.1: Radioactive sources used in the comparison study. Decay mode list: EC for electron capture, $\beta-$ for electron emission, $\beta+$ for positron emission, IT for isomeric transition. Half-life expressed in days (d), hours (h) or minutes (m). Data extracted using the National Nuclear Data Center On-Line Data Service from the Evaluated Nuclear Structure Data File database, file revised as of (2017-05-17) (Bhat 1992).

Isotope	Gamma energy [keV]	Branching ratio [%]	Decay mode	Half-life
Indium 111	245	94.1	EC	2.8 d
Iodine 131	364	81.5	$\beta-$	8 d
Yttrium 91m	555	95.0	IT	50 m
Bismuth 212	727	6.7	$\beta-$	60 m
Iodine 132	773	75.6	$\beta-$	2.3 h
Iron 59	1099 - 1292	56.5 - 43.2	$\beta-$	45 d
Zinc 65	1116	50.0	EC / $\beta+$	244 d
Calcium 47	1297	67.0	$\beta-$	4.5 d
Magnesium 28	1342	54.0	$\beta-$	21 h
Sodium 24	1368	100.0	$\beta-$	25 h
Potassium 42	1524	18.1	$\beta-$	12 h
Thallium 208	2614	99.8	$\beta-$	3 m

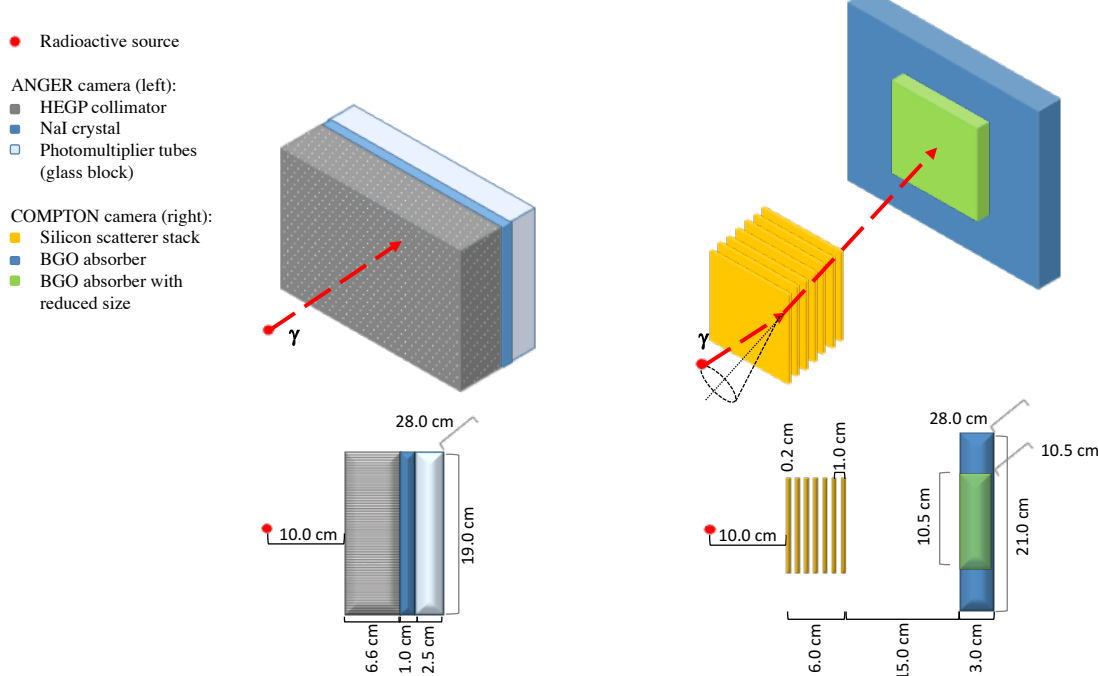


Figure 5.1: Sketch of the simulated geometry of the two systems: Anger camera (left) and Compton camera (right), in 3 dimensions (top line) and side projection (bottom line).

detailed in the following. A SPECT specific optimization would depend on the choice of the particular gamma energy and it has not been studied yet.

The distance between the last silicon plane (center) and the center of the absorber is set to 15 cm (see Figure 5.1). Moreover, the absorber size has been adapted to be as close as possible to the Anger camera detector, maintaining the real BGO block size. As a result, a matrix of 8×6 blocks has been arranged, for a total surface of $28 \times 21 \text{ cm}^2$. In the work of Han and colleagues (Han et al. 2008) a Philips camera was described in GATE as Anger system and the same NaI absorber detector was adapted for the simulation of the Compton system with the introduction of silicon pad detectors as scatterer part. The two geometries compared in this study are slightly different but the common absorber size strategy has been maintained.

The values for energy and spatial resolution of the silicon and BGO detectors used in the simulation were derived from the first tests performed on the detector prototypes (see chapter 3). For the silicon planes, the energy resolution is obtained from the ENC:

$$\sigma_E = W_{Si} \sqrt{\text{ENC}^2 + F_{Si} \frac{E_{dep}}{W_{Si}}}, \quad (5.1)$$

where $F_{Si} = 0.115$ is the silicon Fano factor, E_{dep} is the energy released in the detector (in eV) and W_{Si} is the energy required to create an electron-hole pair in silicon (3.6 eV). The ENC strongly affects the detector performance and it will be analyzed in the following.

The spatial resolution was set according to the geometric parameters considering that the employed DSSDs have a total of 64 strips per side, with a pitch of 1.4 mm. The position of each interaction is set in the center of the strip where it is recorded in both detection planes. Charge sharing on neighbor strips can in principle allow for sub-pitch resolution, but according to preliminary characterization measurements the probability of such a kind of events is less than 10%, and will be so neglected. The interaction depth is set as the center of the involved detector slab. The time resolution has been set to 20.0 ns FWHM based on characterization measurements performed at the GANIL accelerator in France and in the lab at IPNL (see chapter 3 and Ley 2015).

The energy and timing resolution in the BGO blocks are set to 21% FWHM and 3.0 ns FWHM respectively, also based on characterization measurements performed with a cesium-137 source (662 keV gamma ray emission) and at the GANIL with prototype blocks. Concerning the spatial resolution, it has been verified that a sub-pixel resolution is not achievable on a single event basis, it is therefore fixed to the size of a single pixel (see chapter 3). Each block surface is streaked with an 8×8 pixel matrix, 4.4 mm side, not reproduced in the simulation code. Each interaction is assigned to the center of the pixel where it is localized at the analysis stage, while the interaction depth is set at the center of the involved block.

5.2.2.2 Data collection and analysis

The radioactive source is placed at 10 cm distance from the first silicon detector, in the center of the scatterer stack transverse surface, and the number of simulated primaries is set to 10^7 gammas per energy step. To speed up the simulation, the primary gammas are emitted in a

direction within the acceptance cone defined by the first Compton camera silicon plane. All results are then normalized to the full solid angle.

All the events with at least one interaction in a silicon plane or at least one interaction in a BGO block are stored during the simulation process in two data sets, one per detector section. A small fraction of events presents interactions in more than one scatterer plane (< 1% at 245 keV) and/or in more than one BGO block (~8% at 245 keV). This kind of events leads to ambiguities in the cone reconstruction, because the cone vertex and axis are not univocally defined, and it is not treatable via LM-MLEM reconstruction. Alternative reconstruction algorithms (such as the one included in the MEGAlib ([Zoglauer et al. 2006](#))) are able to estimate the most likely scenario for multiple interactions, at the expense of larger uncertainties and longer calculation time. The multiple interaction events, representing approximately 8% of the total at 245 keV, are then refused in this study for simplicity. This choice reduces the detection efficiency, so that the value obtained here could be seen as the lower limit for this kind of detection system. Once the two lists of events are built, the time coincidences are defined according to the source activity, the detector geometry and the single detection section time resolution. Finally, the emission points are reconstructed with a LM-MLEM algorithm developed by the CREATIS institute in Lyon ([Lojacono et al. 2013](#)). The iterative algorithm reconstructs the Compton cones from the position and energy deposited in the scatterer stack and in the absorber blocks. A reconstruction volume must be defined, as well as a voxel 3 dimensional matrix in this volume. For this study the reconstruction volume has been fixed to $5 \times 5 \times 5 \text{ cm}^3$ around the source, with a matrix of $51 \times 51 \times 51$ voxels, and 15 algorithm iterations: this number is a compromise between reconstruction performance and calculation time.

5.2.2.3 Compton camera study for SPECT application

As already mentioned in the introduction, a critical parameter in the Compton camera performances is the scatterer detector energy resolution. The goal of the instrumental development is to obtain an energy resolution as close to 1 keV (σ_E) as possible. The silicon detectors composing the stack have been tested at various temperatures in order to understand the behavior of the electronic noise and of the leakage current, and the read-out electronics is being developed with the aim to reduce the electronic noise (see chapter 3). The first laboratory tests showed an energy resolution at 25°C of approximately 10-15 keV FWHM with a first read-out card prototype. The new card has been tested with simulated signals and gives a noise level closer to the expectations. No data are yet available to determine the detector energy resolution at different temperatures and with the final card version. In the simulation two different resolutions have been considered in order to verify the influence of this parameter on the final reconstructed image. The two chosen values are $\sigma_E = 2 \text{ keV}$ and $\sigma_E = 4 \text{ keV}$, corresponding to about 5 keV and 9.5 keV FWHM, respectively, both calculated at 200 keV of released energy using equation 5.1. The influence of Doppler broadening has also been studied by disabling the Doppler effect in the simulation with the energy resolution set to $\sigma_E = 2 \text{ keV}$. Finally, a different possible scatterer material, CdTe, has been tested at the same resolution in order to verify the expected advantage given by the choice of silicon.

A coincidence study is mandatory to define the source activity to be used in the simulations dedicated to the benchmark with the Anger camera. Timing information is not included in the simulation code and a time structure must be assigned to the simulated primaries at the data

analysis stage. A reference time is chosen randomly from an uniform distribution between 0 s and the data acquisition time and assigned to a primary photon. The data acquisition time (T_{DAQ}) is calculated as the expected time needed for the emission of the desired number of primaries ($N_{primaries}$) according to the source activity A_{source} :

$$T_{DAQ} = \frac{N_{primaries}}{A_{source}}. \quad (5.2)$$

The source activity is not fixed at the simulation stage but only during data analysis afterwards. It can therefore be easily modified to perform a study of the camera performance with different kinds of sources. The scatterer and absorber interaction times are calculated with respect to the reference primary emission and included in the related data sets for the analysis.

Two sets of data are produced as output of this analysis, one for the scatterer and one for the absorber: Each element in the two sets corresponds to an interaction in the detector and includes the interaction 3 dimensional position, energy released, time with respect to the total data acquisition time and primary reference index provided by the simulation. The elements in the two data lists are ordered for increasing time. The detectors time resolution specified in section 5.2.2 and a time window set to 20 ns, corresponding to a 3σ acceptance, are then used for the coincidence definition for different source activities. The time of each element in the absorber data set is compared to the time of the elements in the scatterer data set. A coincidence is defined when the scatterer event time is within the time window centered in the absorber event time. Each element is used one time only, and the analysis continues until the end of the absorber data list. If the two elements (one from the scatterer data set and one from the absorber one) forming a coincidence have the same reference index, they correspond to interactions of the same primary photons and the coincidence is then a true one. If the reference index is different for the two elements, the coincidence is random. The number of true and random coincidences has been studied as a function of the source activity in a range of clinical interest between 1 MBq and 500 MBq, for a fixed energy value of 555 keV. The variation of the influence of random coincidences as a function of the energy was also investigated at a fixed source activity of 200 MBq.

The scatterer energy resolution and the source activity have been fixed for the benchmark study. The choice of their values is discussed in section 5.3.

Finally, with the same scatterer energy resolution and the source activity, the design of the Compton camera has been tested for this specific application, in particular for what concerns the number of employed scatterer planes. In addition to the original design configuration with seven DSSDs, additional sets of simulations have been performed at four reference primary gamma energy reducing the number of layers in each set, in order to assess the camera optimal configuration as a function of the gamma energy. The results are shown in section 5.3.3 and are expressed according to the figures of merit used for the benchmark study (see section 5.2.4).

5.2.3 Anger camera simulation and data analysis

5.2.3.1 Simulation settings

The Anger camera system is simulated with GATE v.7.1 and it is based on the General Electrics Healthcare Infinia SPECT system ([GE Healthcare 2006](#)), a commercial clinical camera with parallel hole collimator and NaI(Tl) scintillator. A single detection head is simulated in order to obtain a direct performance comparison to the Compton system.

The chosen configuration includes a HEGP lead collimator, 6.6 cm thick, with a surface of $28 \times 19 \text{ cm}^2$ (see Figure 5.1). The parallel hole grid is composed of hexagonal shaped holes, 0.2 cm radius, arranged in a quincunx structure, with a septal thickness of 1.8 mm. This collimator is optimized for energies below 364 keV, corresponding to the main gamma emission energy of ^{131}I . The NaI(Tl) crystal is simulated as a single block of $28 \times 19 \times 1 \text{ cm}^3$, in contact with the collimator back surface and read out by photo-multiplier tubes. The photo-multiplier grid is represented with a glass block of 2.5 cm thickness behind the crystal, with the same transverse surface (see Figure 5.1). The spatial and energy resolutions have been set according to the manufacturer specifications. Unless otherwise stated, their values correspond to one standard deviation. A lower detection energy threshold has been set to 80 keV.

The source is placed at 10 cm distance from the collimator surface (the distance chosen in the Infinia data sheet), as for the Compton camera with respect to the first silicon layer, and its transverse position corresponds to the center of the central collimator hole. For each source energy, 10^8 primary photons are simulated in 4π . An event corresponds to single or multiple interaction of a photon (or secondary particle produced by the photon interaction in the collimator) in the NaI(Tl) crystal. All the detected interactions are computed and the gamma interaction position is calculated during the simulation as the center of gravity of the positions of all the hits (energy transfers of secondary electrons), with the deposited energy as weight for the calculation. The deposited energy corresponds to the sum of the energies released during each hit. A set of interaction points and energy deposited is then stored.

5.2.3.2 Data analysis

Four source primary energies have been chosen as references of the studied energy range and are used in the following to show the analysis method and the study results. The low energy range is represented by the ^{111}In emission at 245 keV, the first energy above the Anger camera construction limit has been set to 555 keV ^{91m}Y , while ^{59}Fe at 1099 keV and ^{42}K at 1524 keV have been chosen to represent the medium and high energy range respectively.

Figure 5.2 presents the raw radial event distributions for the four reference energies. Each distribution bin content is normalized according to the surface of the circular region corresponding to each radius. The first distribution bin always corresponds to the radius of the central collimator hole, with the partial inclusion of the surrounding septa. This choice is determined by the detector and collimator geometry and by the source position. It is possible to list three different kinds of events contributing to the radial distributions:

1. photons passing through the collimator holes without interactions,
2. photons traversing the collimator septa without interactions,

3. photons interacting in the collimator septa.

Only the first listed contribution transports true spatial information about the source location, and these photons generate the signal. All other kinds of events contribute to the background, which rapidly increases with the primary photon energy.

A background rejection is performed in order to extract the distribution corresponding to the signal. The complex background contribution cannot be determined analytically, we therefore approximated the background profile as a linear fit to the tail of the radial distribution. The fit limits have been defined as follows:

- the lower limit is calculated as the radial distance where the photon flux on the NaI(Tl) detector is reduced to a fraction $\frac{1}{e}$ by absorption effect in the collimator septa;
- the upper limit has been fixed to the half of the collimator smaller lateral side (95 mm), in order to avoid any kind of geometric effect due the binning choice or the normalization surface selection. The bin size creates artifacts in the radial distribution corresponding to the collimator limits, because three different geometries are involved: the circular surface covered by each distribution bin, the hexagonal shape of the collimator holes and the rectangular collimator geometry.

The estimated background profile is subtracted from the raw distribution and the result is used as reference of the image signal (Figure 5.2).

Three validation tests have been performed in order to check this analysis method.

First, according to the geometry of the collimator and to the mass attenuation coefficient of NaI(Tl) (Hubbell et al. 1987), we evaluated the expected number of entries in the first distribution bin (before normalization), corresponding to the central collimator hole in front of the source. The calculation is performed with the attenuation law of photons in 1 cm of NaI(Tl). A dedicated set of simulations has been performed equivalent to the ones for the Anger camera described in section 5.2.3.1, but using an ideal detector and a reduced number of photons of 10^7 . No uncertainties are applied on the position of photon interactions to avoid resolution effects and the background is estimated via a linear fit as described above. The obtained entries in the first distribution bin after the fit selection are compared to the ones obtained with the theoretical calculation. In Figure 5.3 the results are shown as a function of the source energy.

There is a good agreement between the values calculated with the attenuation law and the simulation data selected with the fit-based background subtraction, and the detected variations from the ideal trend are within the statistical fluctuations. A slight overall effect of under-detection is observed (about 10% on average), while the single value at 245 keV shows an opposite behavior (with a difference of less than 20%). This is related to the chosen fit function.

As a second validation, an additional set of simulations has been performed with the same settings as defined in section 5.2.3.1 but with an infinitely dense collimator. This configuration removes the background contribution given by the photons deflected via Compton interaction on the collimator septa. The raw radial distributions obtained with this set of simulation is

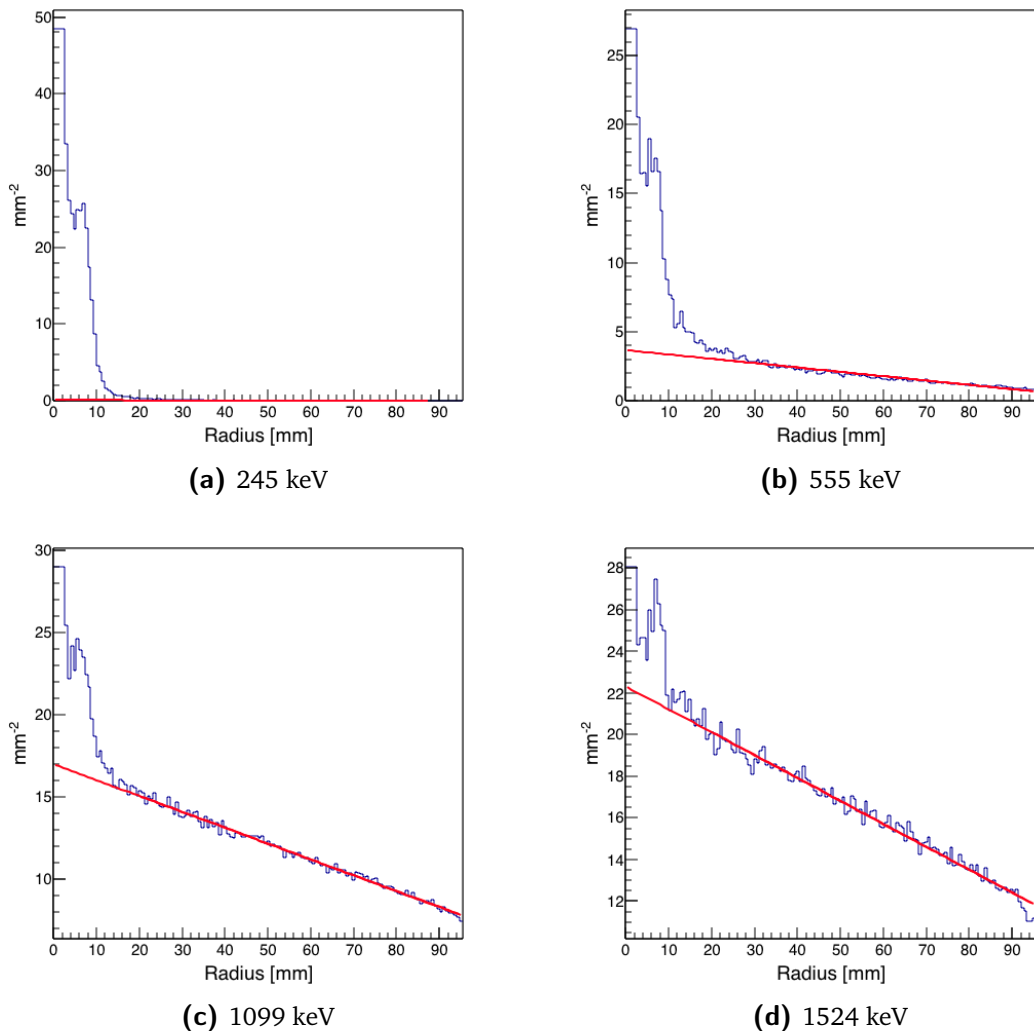


Figure 5.2: Radial event distribution normalized by the circular surface corresponding to each bin for 4 representative source energies, with the linear fit performed for background rejection. The total number of simulated primaries for each data set is 10^8 .

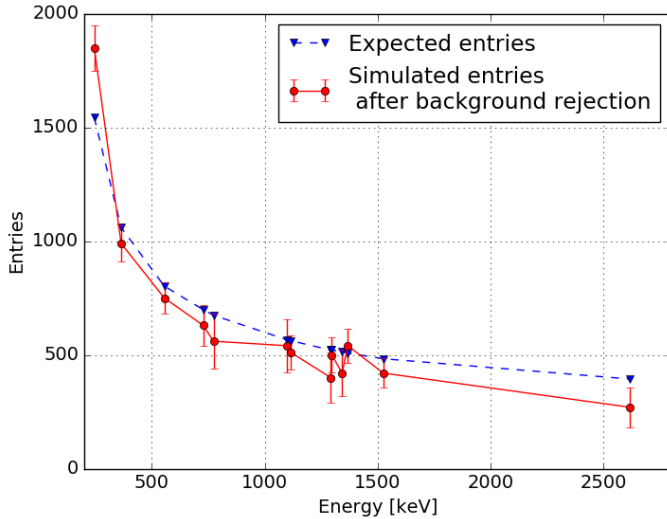


Figure 5.3: Comparison between expected entries in the central collimator hole (blue dashed curve) calculated according to pure geometrical factors and detector interaction cross section and simulated detected entries after background rejection (red solid curve) with null spatial resolution (ideal detector) to avoid resolution effects and lower energy threshold set to 80 keV.

compared to the radial distribution “derived” by the simulations with nominal settings after the application of the fit-based background subtraction. The results are shown in Figure 5.4.

It can be noticed that the distribution overall trend is reproduced by the fit-based background rejection method, the main source of difference being probably the contribution of the scattering in the hole grid surrounding the central one.

The third validation test consisted in a set of simulation with a full lead collimator, with no holes. This configuration allows to estimate the distribution of events traversing the collimator with no interaction, with the aim of demonstrating the efficiency of the selection method to remove their contribution to the final image. Figure 5.5 shows the comparison between the raw distributions (no event selection is applied) obtained with the standard configuration and with the full collimator. The amount of photons able to traverse the lead block at low energy (245 and 555 keV) is totally negligible, while at higher energies this kind of events creates an offset which follows the raw event distribution. Anyway, by observing the selection functions obtained by the linear fit in Figure 5.2, the efficiency of the background employed rejection method in removing this contribution results clear.

The linear fit appears to be a robust way to select the signal transporting spatial information from the source and is applied with no modification for the entire energy range, giving to the analysis method the desired consistency.

5.2.4 Figures of merit for the comparison study

The two cameras are studied and compared according to three figures of merit which refer to their main detection parameters: spatial resolution, detection efficiency, and signal-to-

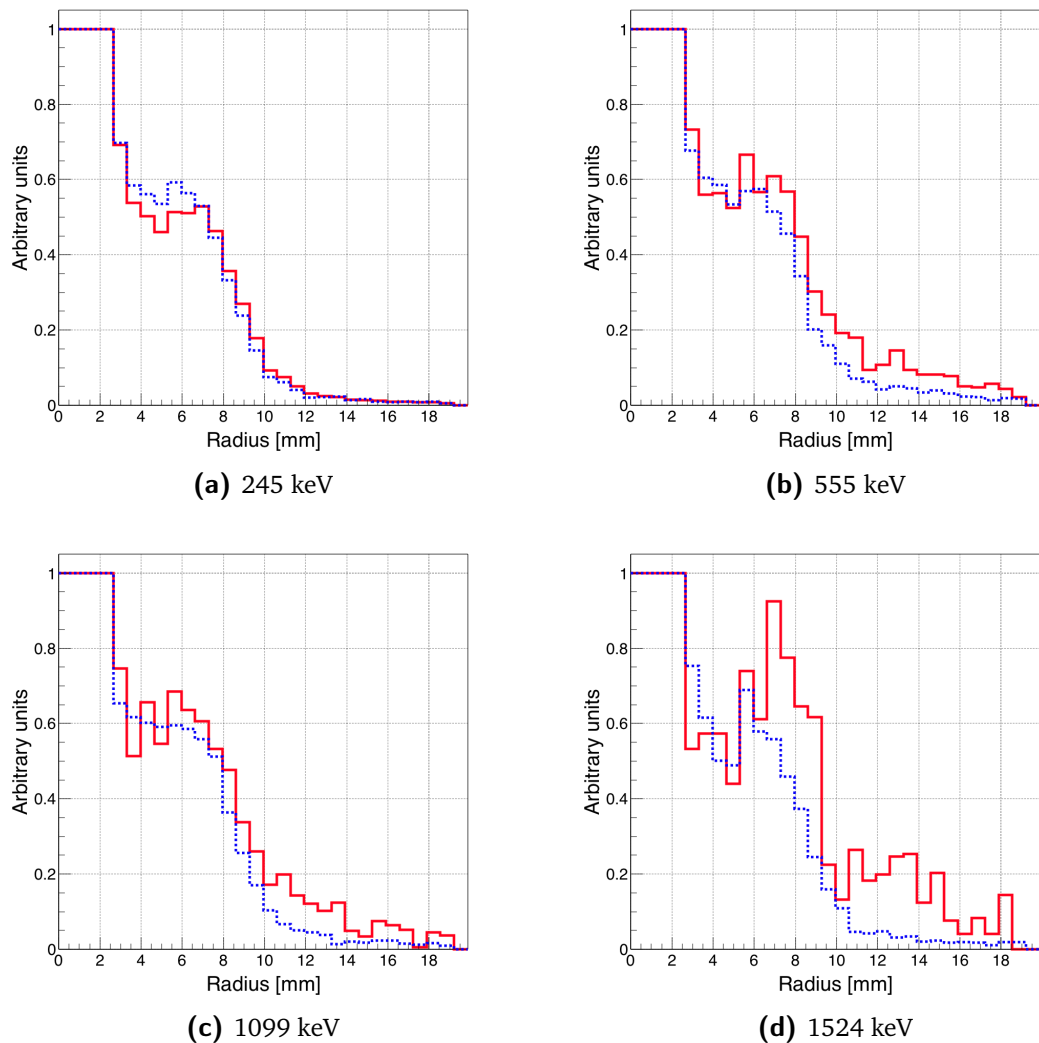


Figure 5.4: Normalized radial distribution with background rejection (red solid lines) compared to normalized radial distribution for infinite density collimator (blue dashed lines).

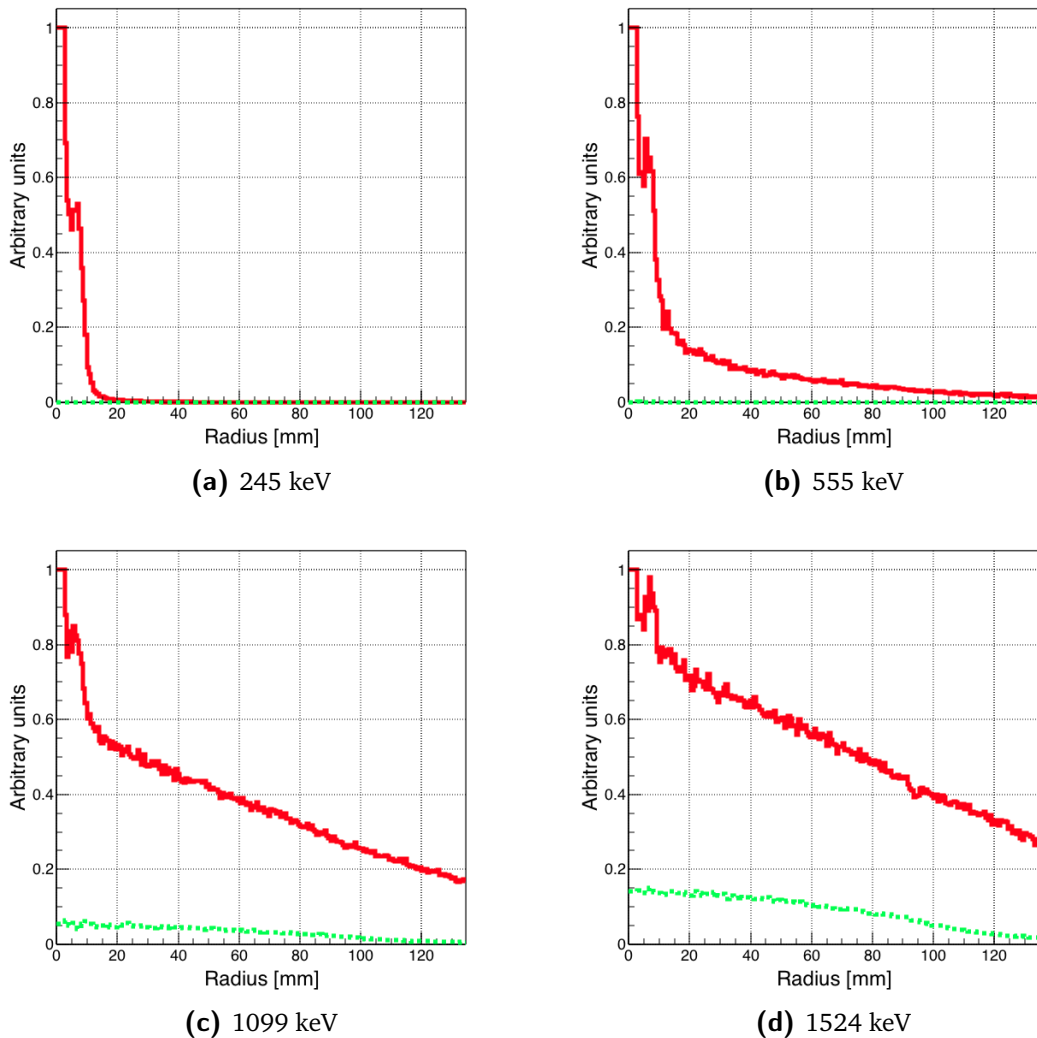


Figure 5.5: Normalized radial distribution with no event selection (red solid lines) compared to normalized radial distribution for full collimator (green dashed lines). Both curves are normalized to the maximum of the raw radial distribution.

background ratio. The definition of these three values must be adapted to the two detectors, keeping in mind their differences: on one side the Anger camera provides a transmission image through a mechanical collimator, with no need for a reconstruction process and with a single detector component; on the other side, the Compton camera relies on event time-coincidences and needs a reconstruction algorithm to obtain the final spatial distribution.

In this study, the imaging process of a point source was simulated. The three figures of merit are therefore evaluated based on the radial event distribution, in order to profit of the radial symmetry of the simulated system.

For the Compton camera, the standard deviation of the radial distribution is used to express the detector spatial resolution, the detection efficiency is defined as the ratio between reconstructed events (via LM-MLEM algorithm) and total simulated primaries, and the signal-to-background ratio corresponds to the ratio between the number of reconstructed events and the total number of coincidences selected before the reconstruction with the coincidence analysis.

For the Anger camera, it is difficult to define the spatial resolution, as shown in (Cecchin et al. 2015). Here, we use the standard deviation of the signal radial distribution in order to be consistent with the Compton camera definition already proposed (the “signal” substantive means entries after background rejection). The detection efficiency is defined as the ratio between the number of signal events and the total number of simulated primaries. Finally, the signal-to-background ratio is evaluated as the ratio between the signal events (the entries in the radial distribution after the fit-based background rejection) and the total number of events recorded by the detector (the entries in the raw radial distribution).

5.3 Results: Compton camera study for SPECT application

The results of the characterization of the CLaRyS Compton camera prototype for the application in SPECT are presented in the following sections, dedicated to the study of the scatterer detector energy resolution and of the Doppler broadening effect, and to the analysis of the rate of random coincidences, respectively.

5.3.1 Influence of Compton camera scatterer detector energy resolution

Figure 5.6 shows the standard deviation of the radial distribution obtained after the LM-MLEM reconstruction (see section 5.2.2.2) as a function of the source energy for the two different analyzed noise levels ($\text{ENC} = 500 \text{ e}^-$, corresponding to $\sigma_E = 2 \text{ keV}$, and $\text{ENC} = 1100 \text{ e}^-$, corresponding to $\sigma_E = 4 \text{ keV}$). The maximum detected difference is about 35%, but the influence of the silicon detectors’ energy resolution rapidly reduces at increasing energy. In the same figure, the results for the simulation without the Doppler broadening for the lowest energy resolution are shown. It is clear that this parameter has a strong influence for the Compton camera spatial resolution, at least for energies below 2.5 MeV. This result justifies the choice of silicon as scatterer material, because it is the lowest Z available detector and therefore minimizes the Doppler contribution. This is underlined by the black curve corresponding to a CdTe

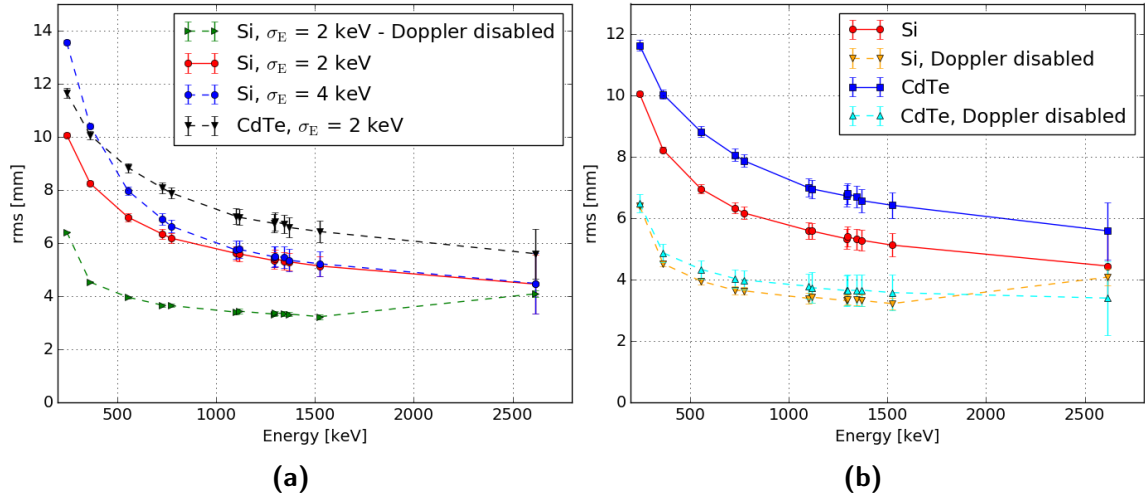


Figure 5.6: Reconstructed radial distribution standard deviation as a function of the source energy. Two energy resolution values are set to the silicon detectors ($\sigma_E = 2 \text{ keV}$ - red dots solid line - and $\sigma_E = 4 \text{ keV}$ - blue dots dashed line), the Doppler broadening effect has been removed (green horizontal triangles dashed line) and the scatterer material has been changed with CdTe solid state detectors (black vertical triangles dashed line), for a fixed energy resolution of $\sigma_E = 2 \text{ keV}$.

detector, i.e. a higher Z material than silicon. For this last study, the electronic noise level has been set for CdTe in order to have the same intrinsic resolution as for silicon ($\sigma_E = 2 \text{ keV}$ obtained with equation 5.1).

For the benchmark with the Anger camera, the ENC value of the Compton camera scatterer components has been fixed to 500 e^- , which corresponds to the expected average level of noise affecting the silicon detectors between -20°C (identified as the ideal working temperature) and 0°C (the silicon detectors are cooled down with a thermal-regulated box, see chapter 3 for a detailed description) and with the final acquisition card (about $2 \text{ keV } \sigma_E$). This value has to be experimentally verified.

5.3.2 Compton camera coincidence study

Figure 5.7 (left) shows the numbers of true and random coincidences as a function of the source activity, ranging between 1 and 500 MBq in order to explore the whole range potentially employed in real examinations. The energy is set to 555 keV.

At 200 MBq source activity, the same amount of true and random coincidences is observed at 555 keV gamma energy. With activities above this value, the ratio between true and random coincidences is less than one. In principle the reconstruction LM-MLEM program can partially reject this kind of events and if we consider the expected important increase in detection efficiency guaranteed by the “electronic collimation”, it results clearly that it is not worth to employ high activity sources (or that a smaller camera can be considered at the expense of the examination time).

For the further analysis and the final detector comparison, the source activity has been then

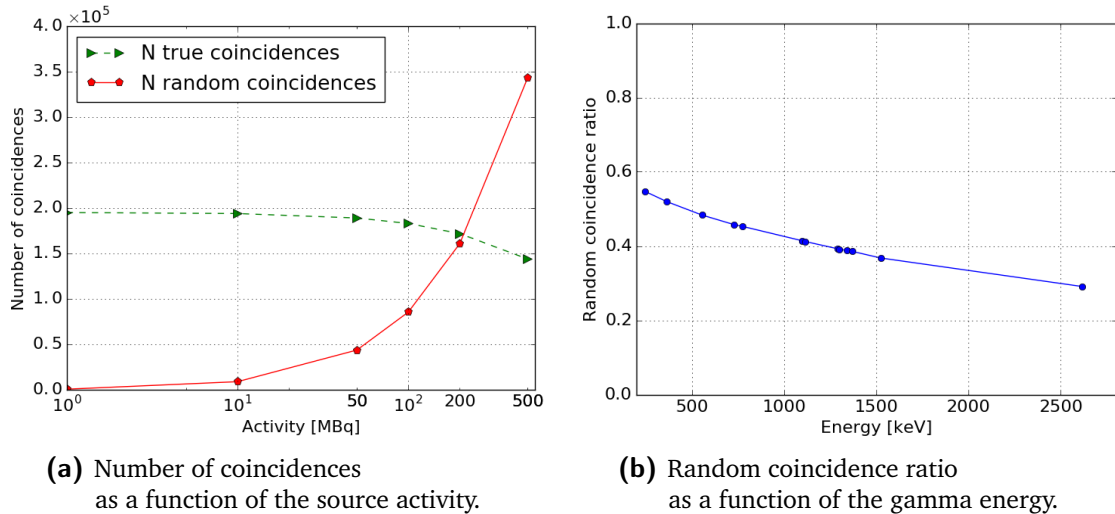


Figure 5.7: (a): number of true (green) and random (red) coincidences as a function of the source activity in the range 1-500 MBq, for the reference energy of 555 keV. (b): Percentage of random coincidences as a function of the source energy, with a fixed source activity of 200 MBq. Compton camera parameters: time resolution FWHM of 20 ns for silicon detectors, 3 ns for BGO and a coincidence window of 40 ns. The source branching ratio has been set to 100% for all sources for simplicity in the comparison of results.

set to 200 MBq, and the number of random coincidences is studied as a function of the source energy. Figure 5.7 (right) shows the ratio of detected random coincidences over the total number of reconstructed coincidences (see Section 5.2.2.2) as a function of energy for a fixed activity of 200 MBq. The ratio decreases for increasing energies, because the product of independent interaction probabilities in two detectors decreases faster than the true coincidence one. Therefore, an increasing reconstruction efficiency with LM-MLEM is verified (see Section 5.4).

5.3.3 Compton camera desing study

The reconstructed events efficiency for four reference primary gamma energies is shown in figure 5.8a for five different scatterer configurations: starting from the original design with seven silicon layers, one layer has been removed for each simulation set, until a minimal scatterer stack composed of only three layers. Figure 5.8b shows the results of the same sets of simulations for what concerns the reconstructed event radial distribution RMS.

Concerning the reconstructed events efficiency, an overall efficiency drop is observed for the scatterer configurations with more than four layers at 245 keV photon energy: this probably reveals an effect of total gamma absorption in the scatterer detector section, in parallel to an increased number of events deflected with large Compton angles which escape the absorber field of view. This effect is not confirmed at increasing gamma energy, already at 555 keV. In this energy range, the expected reduction of the overall efficiency for reduced number of scatterer layers (due to the diminished Compton effect probability) is verified. The radial distribution standard deviation shows minimal variations for the different tested configurations.

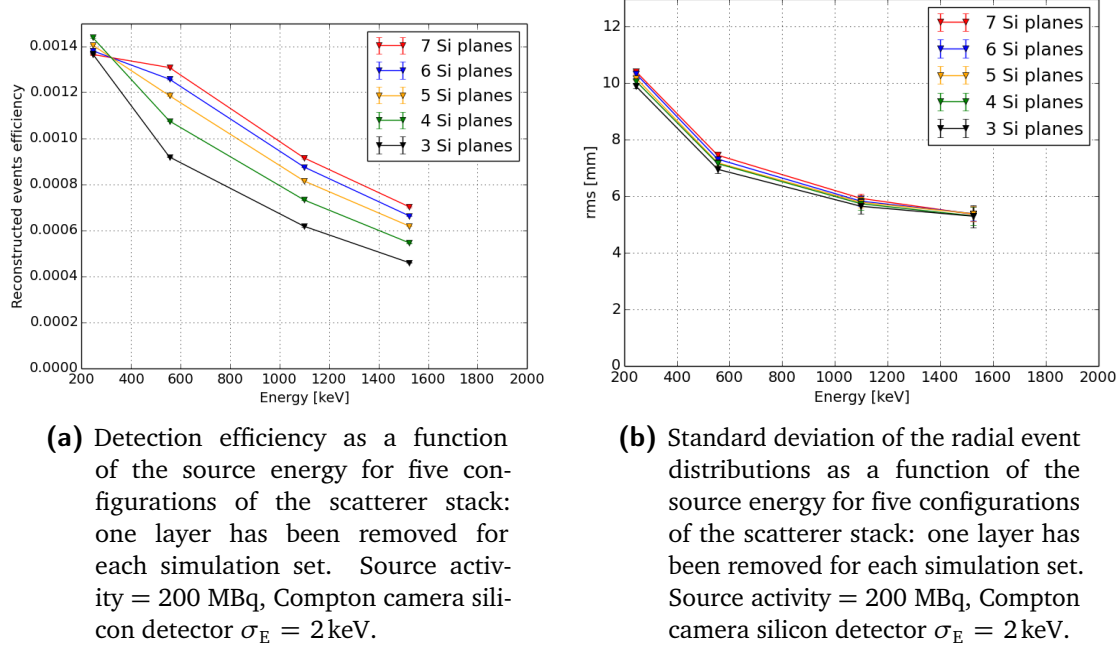


Figure 5.8: Results of the Compton camera design study: reconstructed events efficiency (left) and standard deviation of the radial event distribution (right) as a function of the primary gamma energies for four reference energies and five scatterer stack configurations, with seven, six, five, four and three layers.

At very low gamma energy a scatterer configuration with four silicon scatterer planes appears to be the optimal solution. This is the energy range for which the Compton camera advantages with respect to the commercial Anger cameras are expected to be less remarkable, as explained and verified in the next sessions. At increasing energy, relevant to profit of the Compton camera advantageous features, the original CLaRyS camera design is verified to be the best configuration; this setup has been implemented for the benchmark study.

5.4 Results: Benchmark of Compton camera and Anger camera performance

The analysis methods presented in section 5.2.2.2 and section 5.2.3.2 for the Compton and Anger camera, respectively, have been applied to the simulated data sets of the two cameras at all energies.

The radial distributions for Anger and Compton camera at the different reference source energies and a source activity of 200 MBq are shown in Figure 5.9. The same reference energies selected in section 5.2.3.2 are included here. The radial range is limited to the smaller collimator lateral size (95 mm), according to the fit limits imposed on the Anger camera data (see Section 5.2.3.2). The curves are normalized to 1 for an easier visual comparison.

In Figures 5.10, 5.11, and 5.12, the detection efficiency, the radial distribution standard deviation and the signal-over-noise ratio are respectively shown as a function of the source energy

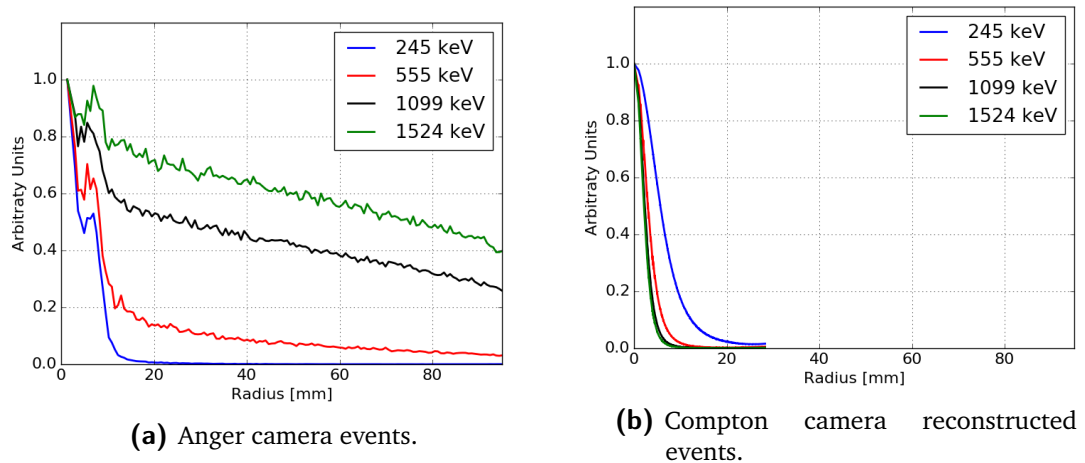


Figure 5.9: Overlap of the normalized radial distributions for 4 selected source energies.

for the two sets of data. Uncertainties (one standard deviation) are reported for all the values and included in the data points when not visible.

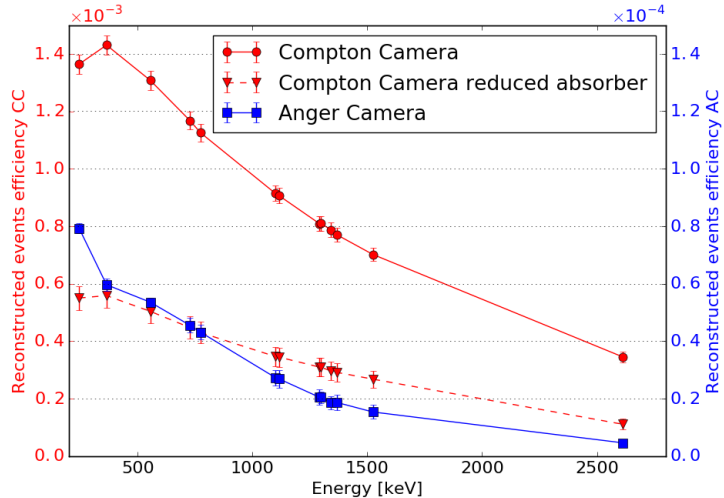


Figure 5.10: Detection efficiency as a function of the source energy. Source activity = 200 MBq, Compton camera silicon detector σ_E = 2 keV.

From Figure 5.10 one can point out the advantage provided by the absence of a physical collimation system in terms of detector efficiency. It should be noticed that two different scales are applied to Figure 5.10 in order to show the two plots on the same figure and appreciate the variations with respect to the energy. The detection efficiency of the Compton camera is always more than a factor 20 higher than the one of the Anger camera. Although the images of the Anger and Compton cameras are based on different kinds of spatial information (a line and a cone, respectively), the Compton camera efficiency should allow a substantial reduction of the injected source activity and/or of the acquisition time. The efficiency of both cameras constantly decreases with increasing energy, because of the decreasing photon interaction probability. The only exception is found at the lowest considered energy of 245 keV in the Compton camera, due to an increased probability of photon absorption in the scatterer and,

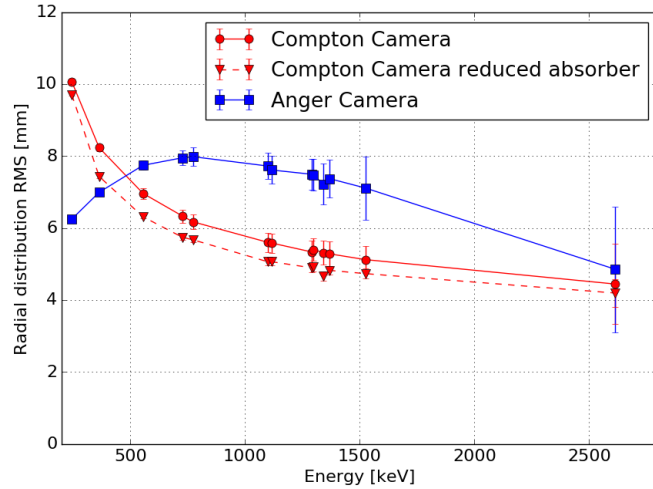


Figure 5.11: Standard deviation of the radial event distributions as a function of the source energy. Source activity = 200 MBq, Compton camera silicon detector $\sigma_E = 2$ keV.

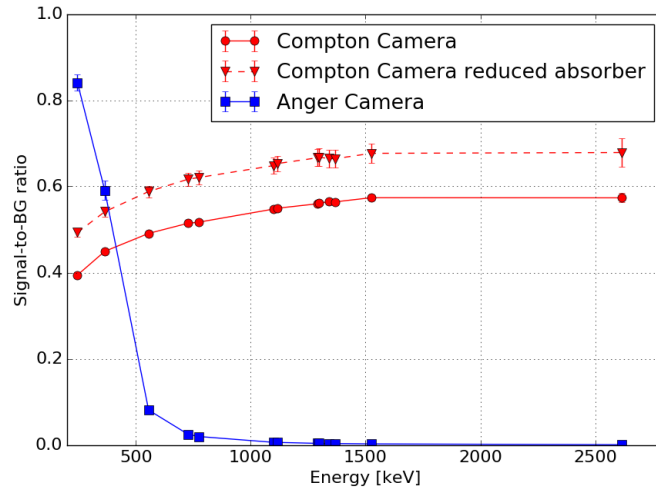


Figure 5.12: Signal-to-background ratio as a function of the source energy. Source activity = 200 MBq, Compton camera silicon detector $\sigma_E = 2$ keV.

in parallel, a larger fraction of events with wide Compton scattering angles at low gamma energy.

The standard deviation of the radial distribution, shown in Figure 5.11, confirms the optimization of the chosen collimator for the Anger camera for low energies (below 364 keV). With the ad-hoc background subtraction operated here, which is not realistic for an extended source, the Anger camera outperforms the Compton one in terms of spatial resolution at low energies (by > 3 mm at 245 keV and about 1.3 mm at 364 keV). However, above 500 keV, the Compton camera can provide a better spatial resolution with a difference ranging between a fraction of millimeter up to about 2 mm. For energies above 1.5 MeV, the two curves of standard deviation for the two cameras reach similar values (< 0.5 mm difference at 2614 keV), but Figure 5.12 shows how the background rejection for the Anger camera and the MLEM reconstruction for the Compton system (see Sections 5.2.3.2 and 5.2.2.2) affect this result. Above 364 keV, the

selection for the background rejection of the Anger camera data drastically reduces the number of events contributing to the final image (the ratio between selected and detected events approaches zero). With an extreme selection, at very high energy the only events contributing to the final image are the events traversing the central hole of the collimator, resulting in an enhanced spatial resolution (see Figure 5.4d). The signal-to-background ratio of the Compton camera confirms the expectations concerning the reconstruction algorithm performance: if compared to Figure 5.7 (right), the curve in Figure 5.12 shows how the rejected events correspond approximately to the amount of random coincidences.

5.5 Summary and discussion

The Compton camera under development by the CLaRyS collaboration is now at the characterization stage. Originally designed and optimized for the application in ion beam therapy monitoring for the detection of prompt-gamma rays in a wide energy range (between some hundreds of keV until about 10 MeV), it is here studied as SPECT detector in comparison to a commercial system based on the Anger gamma camera design.

The expected significant enhancement in terms of detection efficiency, for comparable imaging performance in terms of spatial accuracy, has been already proven in simulation in (Han et al. 2008) with a silicon-sodium iodide based Compton camera prototype at a single primary energy of 364 keV. A factor 20 efficiency gain has been reported.

First of all, the present simulation study aimed to extend these results by testing the two detectors at increasing primary gamma energies, ranging from 245 keV to 2614 keV. A common analysis method has been defined in order to obtain comparable results, always keeping as reference the final image. The results were directly compared in terms of detection efficiency, spatial resolution (standard deviation of the radial event distribution) and event selection (background rejection for the Anger camera and LM-MLEM algorithm selection for the Compton camera) via the definition of three figures of merit.

A preliminary study has been performed on the simulated Compton camera data in order to fix the main parameters of the camera simulations, namely the energy resolution of the silicon scatterer detectors and the source activity determining the coincidence rate. Two ENC values have been studied, resulting in a maximum difference in spatial resolution of 35% at the lowest energies, rapidly decreasing at increasing primary energy. A value of $\text{ENC} = 500 \text{ e}^-$ has been chosen as the closest to the instrumental development expectations and first tests. The influence of the Doppler broadening on the spatial resolution has been also estimated in a factor $\sim 1/3$ at 500 keV, then reduced up to ~ 0 at 2.5 MeV of primary gamma energy, with fixed energy resolution ($\sigma_E = 2 \text{ keV}$ - $\text{ENC} = 500 \text{ e}^-$) in the silicon detectors. Moving to the coincidence rate analysis, at the reference energy of 555 keV and with detector time resolution set according to first characterization results, the simulated data have been analyzed by reproducing a source activity in the range 1-500 MBq. The result shows the expected increase in the random coincidence rate at increasing source activity, with a ratio between true and random coincidences close to one at 200 MBq. This value has been chosen as clinical reference for the comparison analysis. In addition to this, the geometrical configuration of the scatterer stack has been studied in order to check alternative setups with reduced number of DSSDs; this study confirmed the choice of seven planes, implemented for the benchmark analysis.

The results discussed in section 5.4 confirm the conclusion of Han et al. about the advantage given by the usage of a Compton system and show how the gain factor in the detector efficiency is maintained at increasing energy. Concerning the detector spatial resolution, the Compton camera outperforms the Anger system at energies above about 500 keV. The Anger camera spatial resolution can be boosted by aggressive background subtraction in the considered case (point-like source image), at the expense of a drastic signal suppression. However, this approach is not reproducible and exploitable in actual clinical conditions and the obtained results are not comparable to the Compton camera performance at the same energy.

The results of this work clearly show the potential of the Compton camera for the application in nuclear medicine examination, opening new possibilities for the clinical implementation. The studied detector has originally been designed and optimized for another application, and it has only been adapted for SPECT here, but not yet optimized in terms of detector geometry (size, position, and inter-detector distances). For an optimized detector, performance is therefore expected to be improved with respect to the presented results. In future development, the reconstruction LM-MLEM algorithm should be adapted to this application and the reconstruction parameters should be studied to further enhance the final performance, in particular for what concerns random coincidence rejection.

Anyway, these first evidences already allow one to investigate the possible modifications introduced by the clinical set of Compton detection systems. The enhanced detection efficiency in parallel with comparable spatial performances paves the way to the diffused usage of less active sources, or alternatively allows a substantial reduction of examination time: as a result, the dose delivered to the patient would be reduced. On the other side, the possible introduction of sources with higher primary emission energy will reduce the effect of photon attenuation in the patient (not studied in this simulation work), improving by definition the spatial information and further reducing the effective dose delivered to the patient. Simple analytic calculations can show how a photon attenuation of about 66% is foreseen for 364 keV photons in 10 cm of water, while the effect is reduced, for example, to 49 % at photon energy of 1099 keV (Hubbell et al. 1987). Higher energies can be employed also with Anger cameras, at the expense of introducing thicker collimators with reduced holes size, with the result of a reduced efficiency with respect to the analyzed HEGP collimator. Furthermore, a possible implementation of Compton cameras is also foreseen for targeted radionuclide therapy, where the radionuclides used in clinics often have gamma radiation emission at relatively high energy. This signal is difficult to be detected and treated with conventional SPECT cameras, while the Compton detection technique could make it quantitatively exploitable in clinical practice, for both pre- and per- treatment images.

Even though Compton cameras intrinsically lead to 3 dimensional images with a single detector head, the spatial resolution associated to the direction normal to the detector planes has to be more deeply studied, but this feature is an additional point in favor of the introduction of Compton systems in the clinical environment, moving beyond the tomographic concept and towards more compact detector solutions. Several studies are ongoing in order to improve the image reconstruction algorithms and, so, the 3 dimensional imaging performance (Kuchment et al. 2016). Different detection approaches can also, in principle, lead to improved image quality in 3 dimensions, such as the Compton electron tracking (Kabuki et al. 2007; Sonoda et al. 2015). Moreover, a further enhancement in image reconstruction should be given by the measurement of the photon depth of interaction: the photon is assumed to interact in the center of the detector components for our prototype, while perpendicularly segmented

5 Compton camera application in nuclear medicine

detectors can ensure an improved resolution in the third dimension and a resulting enhanced reconstruction accuracy, also involving better 3 dimensional imaging capabilities.

The advantages of the Compton detection principle are here shown thanks to a first detector prototype, but there is still wide room for improvement.

Once the CLaRyS Compton camera will be completed and characterized, tests in clinical environment are foreseen in the field of medical imaging. The actual potential of such a kind of detector will be then quantified with experimental data.

6

Beam tests

Contents

6.1	Hodoscope: december 2017	102
6.2	Hodoscope: may 2018	102
6.3	Collimated camera: august 2018	102
6.4	Collimated camera: september 2018	102

6.1 Hodoscope: december 2017

6.2 Hodoscope: may 2018

6.3 Collimated camera: august 2018

6.4 Collimated camera: september 2018

7

Conclusions and discussion

Appendices

A

Compton camera data format

A.1 Introduction

This document aims to formalize and fix the Compton camera data format. The structure of the data sent by each detector section (scatterer, absorber and beam hodoscope) to the acquisition card is detailed, as well as the structure of the events sent to the acquisition PC.

A.2 General features

A.2.1 Common information

The detector FE cards are connected to the μ -TCA via optical links, with a speed of 3.0 Gbit/s. The transfer frequency is 150 MHz.

All the FE card TDCs share the same synchronized clock, at a 40 MHz frequency, which is sent to the cards through an external link.

Every data packet sent to the μ -TCA by the Front End cards starts with the following information:

- N° Front End (8 bits);
- N° Trigger (24 bits);
- N° Mode (8 bits);
- N° of element in the packet (8 bits).

A.2.1.1 Front End number

The FE number is the identification code of each FE card. A mechanical switch on the card defines the ID which is sent in the data packet header.

In Table A.1 the FE number IDs are listed with the corresponding cards.

Table A.1: Front End number associated to each Front End card.

FE number	FE card
0	All detectors
1	Silicon 1
2	Silicon 2
3	Silicon 3
4	Silicon 4
5	Silicon 5
6	Silicon 6
7	Silicon 7
8	Silicon 8
9	Silicon 9
10	Silicon 10
11	ASM 1
12	ASM 2
13	ASM 3
14	ASM 4
15	ASM 5
16	ASM 6
17	ASM 7
18	ASM 8
19	ASM 9
20	ASM 10
21	ASM 11
22	ASM 12
23	ASM 13
24	ASM 14
25	ASM 15
26	ASM 16
27	Hodoscope 1
28	Hodoscope 2
29	Hodoscope 3
30	Hodoscope 4
31	Hodoscope 5
32	Hodoscope 6
33	Hodoscope 7
34	Hodoscope 8
99	μ -TCA

A.2.1.2 Pre-trigger and trigger

The trigger number identifies each event, where an event is generated every time a coincidence is detected between a BGO block and a silicon layer. Once an interaction is detected in a BGO block, the associated ASM card generates a pre-trigger signal which is sent to the THOR card. This intermediate card shares the pre-trigger signal with the silicon FE cards; if an interaction with a compatible time stamp is found in one of the silicon layer, a trigger signal is generated and sent to all the silicon FE card, as well as to the ASM and hodoscope cards via the THOR card. The trigger signal validates the event, and each FE card sends the collected data to the μ -TCA system. The trigger number allows for a complete event reconstruction by the event builder on the acquisition PC. In Figure ?? the trigger generation process is sketched.

To be noticed that each FE cards sends the collected data independently from the others.

Trigger and pre-trigger encoding

Pre-trigger and trigger signals are used by all the detectors to select the collected data to be sent to the acquisition system. The data selection and transfer must be as fast as possible in order to minimize the trigger latency and camera dead time. In order to reduce the transmission time, pre-trigger and trigger signals have been encoded on 24 bits.

This same trigger number is sent at the beginning of each data packet and is used by the event builder to associate the interactions collected by the three detector sections. With a 24-bit encoding, the trigger number is reset every $1 \text{ ns} \times 2^{24} = 16,78 \text{ ms}$. This time window is short for the event builder, so that for the physical data it is extended to 32 bits for all the FE cards in order to have a reset every $1 \text{ ns} \times 2^{32} = 4,2 \text{ s}$, which is enough for the reconstruction of the events.

A.2.1.3 Mode number

The Compton camera detector components can work in different mode, according to the application requirements. At least two working modes are possible for every detector section: an “optimal” mode, corresponding to the final camera configuration; a “test” mode, allowing for the collection of more raw information. Every operating mode presents a peculiar data format, so that the data packets size is not fixed. In order to fix the acquisition tuning, the mode number is defined before its beginning.

The operating mode are identified as following:

- N° Mode = 1 : 1st mode for silicon
- N° Mode = 2 : 2nd mode for silicon
- N° Mode = 3 : 3rd mode for silicon
- N° Mode = 4 : 4th mode for silicon

A Compton camera data format

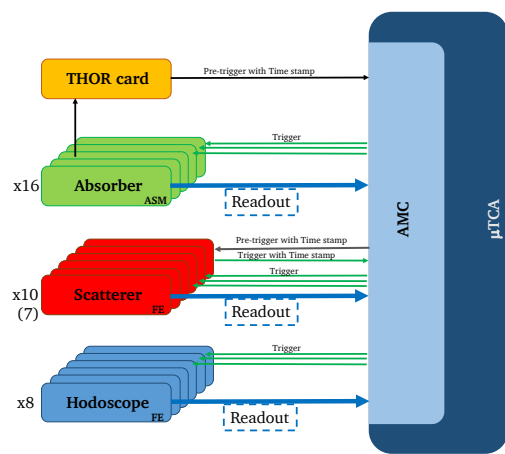
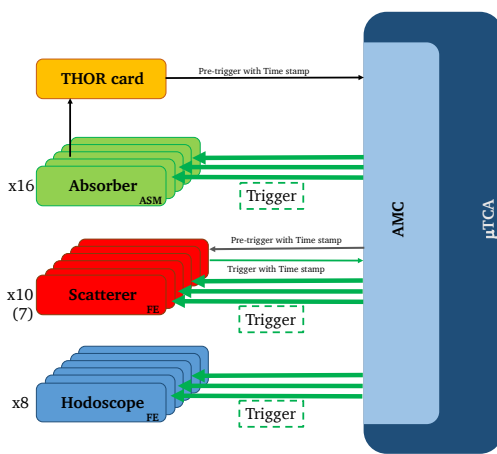
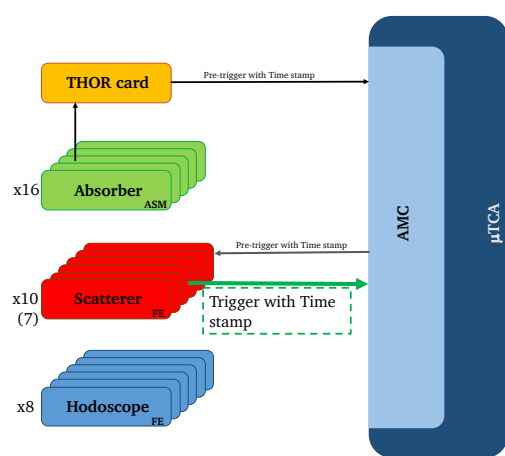
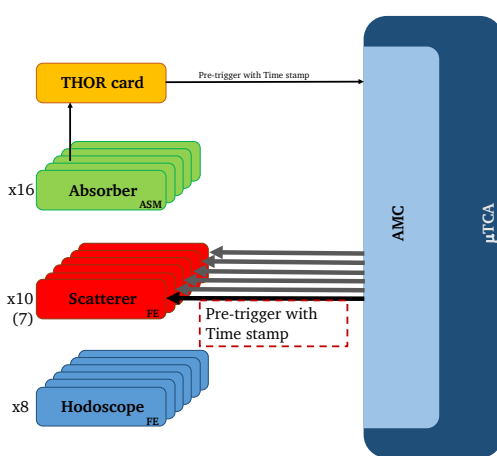
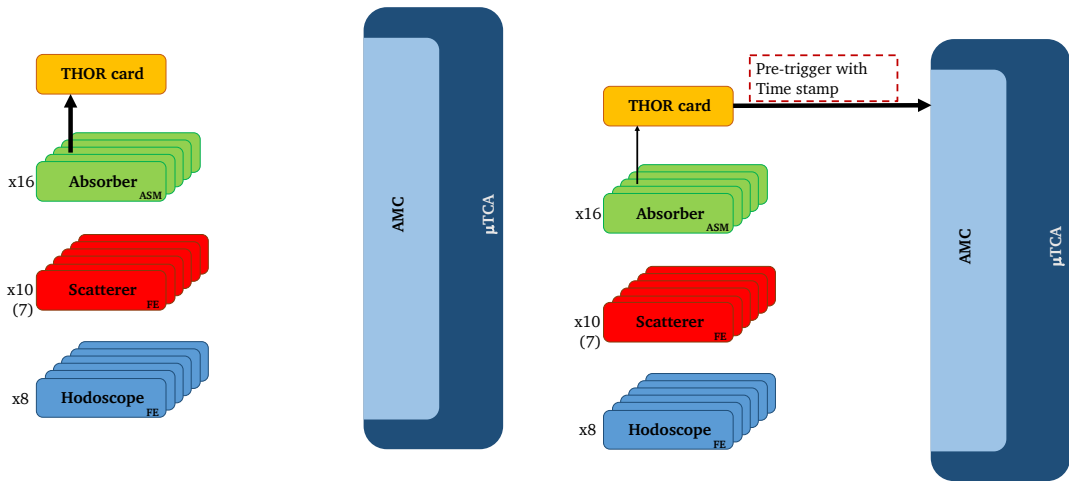


Figure A.1: Data acquisition logic: pre-trigger and trigger generation and readout process.

- N° Mode = 5 : 1st mode for BGO
- N° Mode = 6 : 2nd mode for BGO
- N° Mode = 7 : 1st mode for hodoscope
- N° Mode = 8 : 2nd mode for hodoscope.

A.3 Physical data format

A.3.1 Scatterer detector data format

Four different data formats, corresponding to four working modes, have been defined for the silicon scatterer operation (Figure A.2). For mode 1 and 2, the collected total charge is directly evaluated on the FE card via the slow shaper output and one ASIC, while for mode 3 and 4 the ASIC pre-amplifier output directly sends a sampling of the raw signal. In this last case, the number of samples can be tuned and each sample corresponds to 10 ns. The complete sampling is stored in a dedicated buffer.

Modes 1 and 3

In mode 1 and 3, for each detector strip involved in the interaction, the strip ID, total collected charge and time are stored. The interaction position will be calculated via a center of gravity algorithm at the analysis stage. The raw information about the number of involved strips is useful for the evaluation of the signal dispersion in the detector.

Modes 2 and 4

In mode 2 and 4, the interaction is calculated on the FE card and the number of involved strip is then not stored.

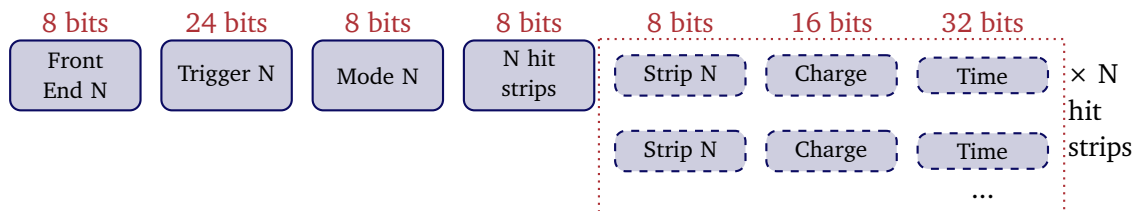
A.3.2 Absorber detector data format

The BGO block readout is performed via the ASM cards. Each card is equipped with 24 input ports (signal PM), corresponding to 6 BGO blocks. Two possible working modes have been defined for the BGO absorber: the collected total charge and time are evaluated on the card, or the PM raw signals are sampled and the sampling is sent to the acquisition (Figure A.3). Charge and time are then calculated at the analysis stage. This second operating mode can be useful in the test phase but it determines a low acquisition rate, so that it can be used only at low beam intensity.

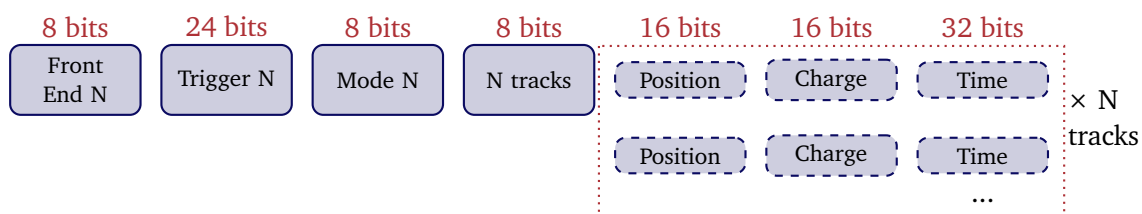
The complete sampling is stored in a dedicated buffer.

A Compton camera data format

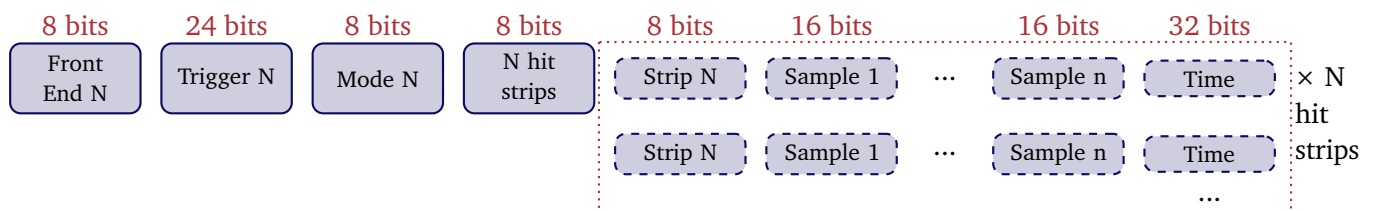
Mode 1



Mode 2



Mode 3



Mode 4

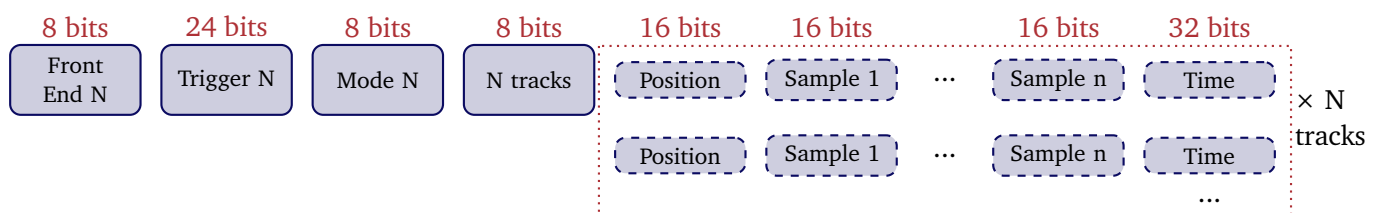
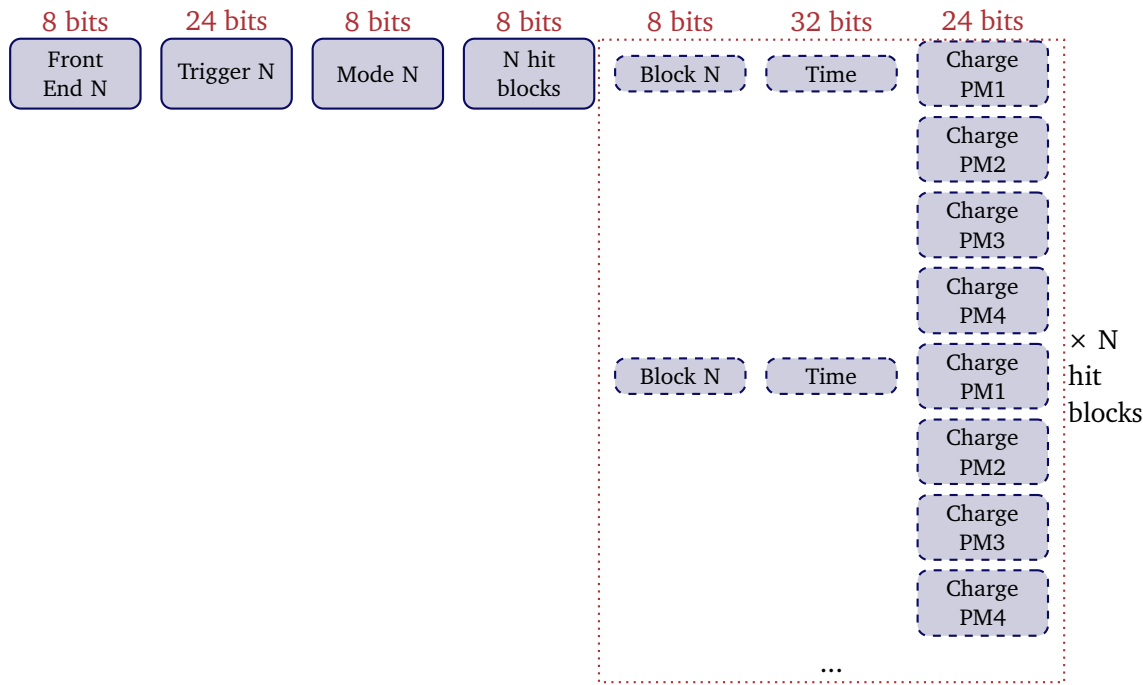


Figure A.2: Scatterer detector data format.

Mode 1



Mode 2

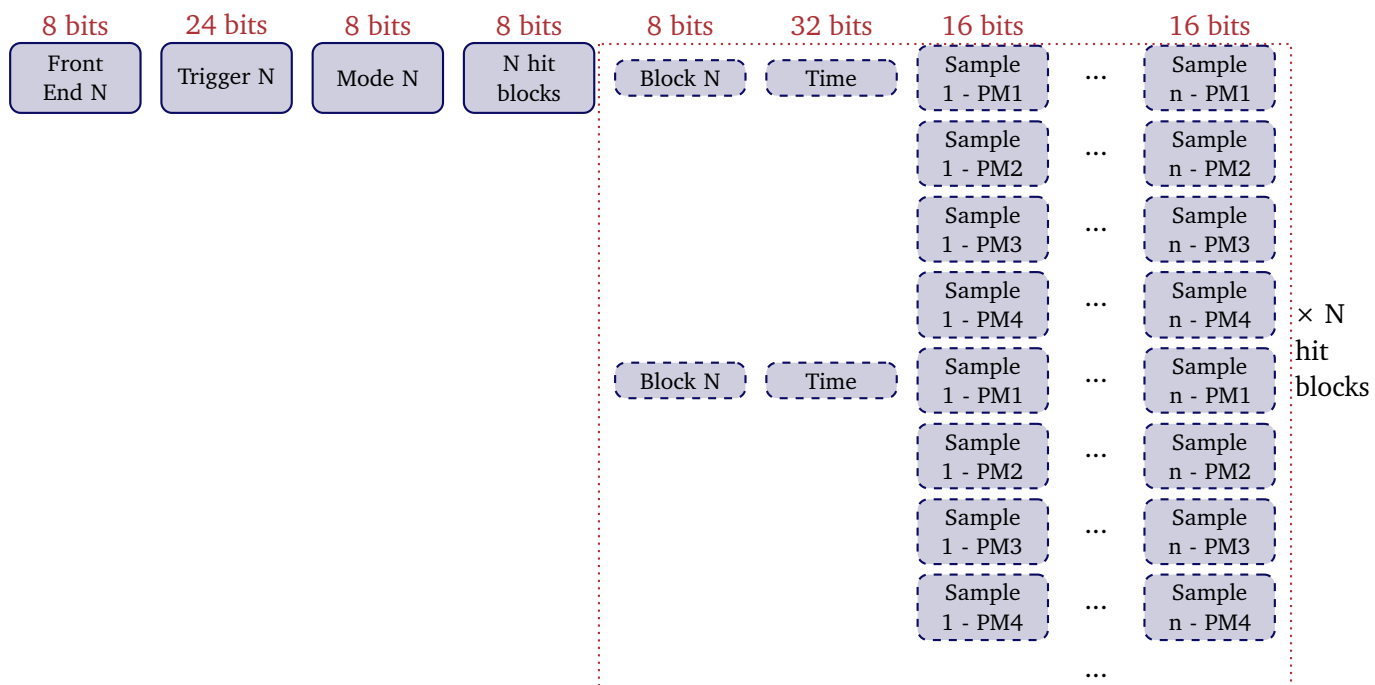


Figure A.3: Absorber detector data format.

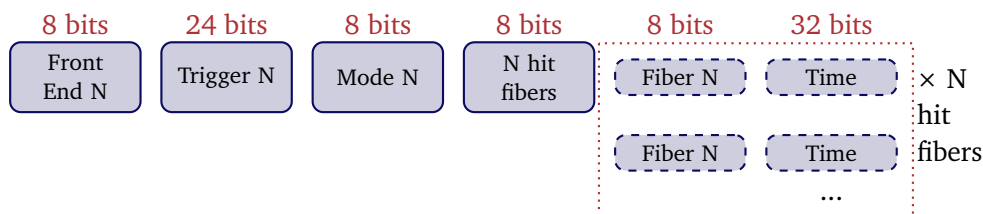
A.3.3 Beam hodoscope data format

The beam tagging hodoscope is composed of two perpendicular planes of 128 scintillating fibers each. Each fiber is read-out on the two sides, for a total of 512 read-out channels. The output signals are send via optical fibers to 8 64-channel PMs H8500 by Hamamatsu. 8 FE cards have been developed for the signal collection, one per PM, and are equipped with two custom ASICs (32 channels each) and one FPGA.

Concerning the “optimal” mode (1st operating mode for the hodoscope), the only collected information are the ID of the involved fibers and the interaction time. The ASICs allow for a minimum time resolution of 10 ns; this means that if two particles interacts in the hodoscope within a 10 ns window, they will be considered as part of a single event.

In test mode, the total collected charge can be calculated. This feature is useful to evaluate the detector aging effect due to radiation exposure. The charge measurement is anyway limited to a single channel per ASIC, so to two channels per PM. The ASIC channel able to measure the charge is identified as “N° Fiber charge 1” and “N° Fiber charge 2”.

Mode 1



Mode 2

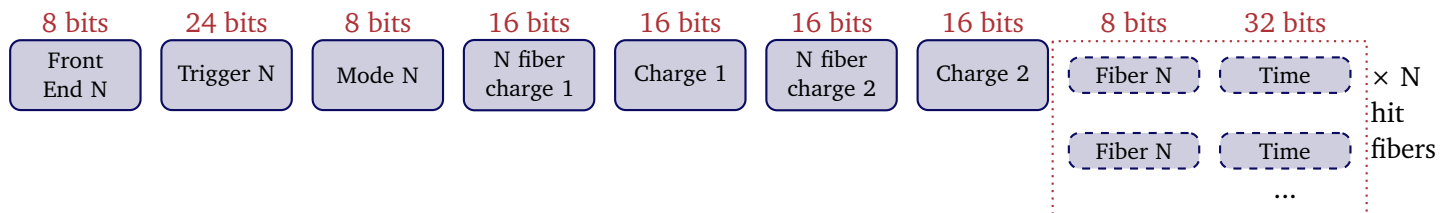


Figure A.4: Beam hodoscope data format.

A.4 Slow control, trigger and monitoring data format

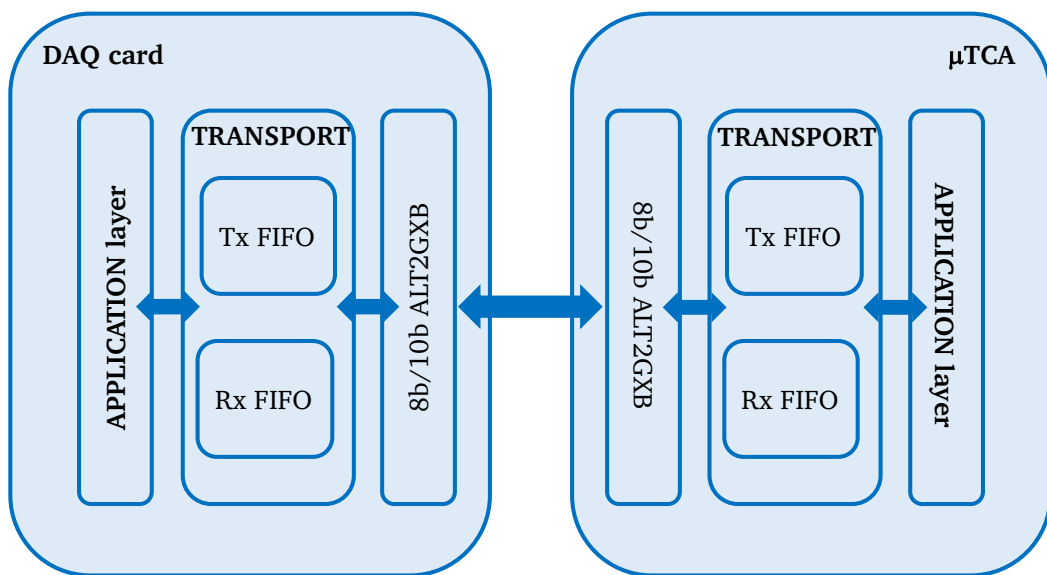
A.4.1 Communication architecture

The Endpoint architecture is composed of three layers:

- application layer

- mac (or transport) layer/processor packet
- physical layer

Figure A.5: Architecture of communication between DAQ cards and μ-TCA.



A.4.2 Transport protocol and processor packets

A.4.2.1 Definitions

It is worth to define some useful terms for the following part of the document:

- byte : 8 bits
- word : 16 bits
- K : control byte
- D : data byte
- cargo : data group
- terminator : packet end

- CRC : cyclic redundancy code

The CRC allows one to detect the transmission errors and the data transfer issues. A specific algorithm must be used, as CRC-16 : $X^{16} + X^{15} + X^2 + 1$. In the present protocol, a “parity pattern of 16 bits” have been used.

The transport layer ensures a proper packets exchange between two terminals via the data encapsulation. The data come from the application layer and are then sent to the physical layer.

A.4.2.2 Data encoding

For the transport layer, the data structure is created via the addition of a packet header, corresponding to a parity bit, of a 16 bit parity pattern and a bit for the end of the packet. The data are 8 bits/10 bits encoded. This standard 8 bits/10 bits encoding ensures sufficient data transitions for clock recovery.

A.4.2.3 Packets format

All the data packets have the same structure. A K byte (control symbol) is followed by the cargo to be sent. The end of the packets changes according to the cargo parity.
If the cargo contains an even number of bytes, the packet ends with K.28.6.

Table A.2: Packet with an even byte number cargo.

Item	Packet beginning	Cargo	Packet end
1	One K byte	0 - N D-bytes	K.28.6

If the cargo contains an odd number of bytes, the packet ends without any control symbol.

Table A.3: Packet with an odd byte number cargo.

Item	Packet beginning	Cargo	Packet end
1	One K byte	0 - N D-bytes	Beginning of a new packet

Remark :

- SYN packet is a special kind of packet starting with K.28.6 and ending with K.28.5. It is only composed of these two bytes (16 bits). It allows the receiver to find the beginning

and the end of the transmitted bytes with the aim to reconstruct the events in parallel. The synchronization speed is 44 Hz (defined by Carlos Abellan).

- In order to optimize the throughput, the control symbol at the beginning of the packet can probably be removed (further study needed).

A.4.2.4 Possible control symbols

In Table A.4, all the possible control symbols are listed (defined by Carlos Abellan).

Table A.4: Control symbol definition.

Item	Name	Control code	Comment
1	K.28.0	0x1C	Acknowledgement
2	K.28.1	0x3C	Ask for writing registers
3	K.28.2	0x5C	Ask for reading registers
4	K.28.3	0x7C	Special command
5	K.28.4	0x9C	Monitoring
6	K.28.5	0xBC	Default synchronization
7	K.28.6	0xDC	IDLE (default) and packet end
8	K.28.7	0xFC	Pre-trigger
9	K.23.7	0xF7	Trigger
10	K.27.7	0xFB	
11	K.29.7	0xFD	
12	K.30.7	0xFE	Physical data

A.4.3 Transport layer

A.4.3.1 Control packet

This kind of packet is used to check the link and for the control/command operations.

- For the link check, two kinds of packets are used: synchronization packet and IDLE packet.
- For the control/command operations, here are some examples: register configuration, FPGA dynamical programming, monitoring, etc.

Control symbol for control :

Acknowledgement packet (Front End cards → μ-TCA)

Table A.5: Control symbol definition.

Item	Name	Control code	Comment
1	K.28.0	0x1C	Acknowledgement
2	K.28.1	0x3C	Ask for writing registers
3	K.28.2	0x5C	Ask for reading registers
4	K.28.3	0x7C	Special command
5	K.28.4	0x9C	Monitoring
6	K.28.5	0xBC	Synchronization
7	K.28.6	0xDC	IDLE (default) and end of packet

This packet is sent by the FE cards and interpreted as an acknowledgement by the μ -TCA. If a part is missing, it is set to zero.

- If 0 = validation
- If 1 = problem detected

Table A.6: Definition of the acknowledgement packet.

Word	1 st byte	2 nd byte							
		7b	6b	5b	4b	3b	2b	1b	0b
1	K.28.0	0	Pb Front End num- ber	Pb with packet begin- ning	Pb with packet end	Pb with CRC	Pb with number of re- ceived words	Pb with parity bit of parity bit of bit of byte 2	parity bit of the ac- knowl- edge- ment packet
2		Front End number							

A.4.3.2 Configuration packets

Writing register process (μ -TCA → Front End cards)

The process starts with a packet sent by the μ -TCA asking for the register writing. The receiver (FE card) sends back an acknowledgement packet to finish the process. In Table A.7 the format of this writing register packet is reported.

Reading register process (μ -TCA → Front End cards)

The process starts with a packet sent by the μ -TCA asking for the register reading. The receiver

Table A.7: Writing register packet.

Word	1 st byte	2 nd byte	Comment
1	K.28.1	Front End number + 1 parity bit	N/A
2	2 bytes with the number of words to be written		The length is word-based: max $2^{16} - 1 = 65535$ words
3	Register address		Address where the writing process starts
4..N+3	Data to be written		0000 0000
N+4	CRC composed of the “xor” of all bits in the same position, from word 2 to word (N+3)		

(FE card) sends back the “measure packet” if the command is correct, an acknowledgement packet if it is not.

At the beginning of the slow control, the physical addresses on the FE cards are read at the address 0.

In Table A.8 the format of this reading register packet is reported.

Table A.8: Reading register packet.

Word	1 st byte	2 nd byte	Comment
1	K.28.2	Front End number + 1 parity bit	N/A
2	2 bytes with the number of words to be read		The length is word-based: max $2^{16} - 1 = 65535$ words
3	Address of 1 st data to be read		Address where the reading process starts
4	CRC composed of the “xor” of all bits in the same position, from word 2 to word 3		/

A.4.3.3 Monitoring process (Front End cards → μ-TCA)

In case of issues, for example when the temperature of a card go beyond a fixed threshold, the DAQ card sends a “monitoring” packet to the μ-TCA. There is not a corresponding acknowledgement from the μ-TCA.

A Compton camera data format

Table A.9: Two special registers(μ -TCA → Front End cards)

Register address	Details	Comment
0	Front End number	No writing rights: register in read-only mode. Hard coded on DAQ card.
1	It defines the working modes	Optimal mode, test mode, collimated camera mode, Compton camera mode, individual detector section test. It is possible to write in the register.
2	It defines the detector to test (in single detector test mode)	Scatterer, absorber, hodoscope.
3	BGO number of sampling	For test mode with the BGO blocks signal sampling.
4	Silicon number of sampling	For test mode with the silicon layers signal sampling.

Table A.10: Measurement packet (Front End cards → μ -TCA)

Word	1 st byte	2 nd byte	Comment
1	K.28.1	Front End number + 1 parity bit	
2	2 bytes for the number of data words to send		The length is word-based: max $2^{16} - 1 = 65535$ words
3	Register address		Address where the writing process starts
4..N+3	Read data		0000 0000
N+4	CRC composed of the “xor” of all bits in the same position, from word 2 to word (N+3)		/

Table A.11: Monitoring packet.

Word	1 st byte	2 nd byte	Comment
1	K.28.4.	Front End number + 1 parity bit	Message in Table A.12.
2	15 bits for the message + 1 parity bit		Message in Table A.12.

Table A.12: Monitoring messages.

Item	Message	Bit[15]	...	Bit[7]	Bit[6]	Bit[5]	Bit[4]	Bit[3]	Bit[2]	Bit[1]	Comment
		Message type						Further information			
1	FPGA recon-figuration error	0	0	0	0	0	1	0	0	0	N/A
2	Tempe- rature alarm	0	0	0	0	1	0	x	x	x	Bit “x” is 1 if the corresponding detector goes beyond the threshold (0 elsewhere)
3	Busy	0	0	0	1	0	0	0	0	0	Front End is not able to send data
...											

A.4.3.4 Special command process (μ -TCA \rightarrow Front End cards)

This process is designed to allow the μ -TCA to send special commands to the FE cards.

Table A.13: Special command packets

Word	1 st byte	2 nd byte
1	K.28.3	Front End number + 1 parity bit
2	15 bits for the special command + 1 parity bit	

A register database (containing the operating mode identification) must be fixed and shared between all the detectors.

A.4.4 Data packets (Front End card \rightarrow μ -TCA)

In the section the packets concerning trigger, pre-trigger and physical data are described. No acknowledgement is demanded for this kind of packets.

Pre-trigger format

This packet is sent to the μ -TCA by the THOR card. The μ -TCA then shares it with all the

Table A.14: Special commands examples

Item	Command name	Bit[15..1] of 2 nd word	Comment
1	System reset	"0000 0000 0001 001"	Acknowledgement packet missing
2	Counter reset	"0000 0000 0001 000"	Acknowledgement packet needed
3	Start run	"0000 0000 0000 100"	Acknowledgement packet needed
4	Stop run	"0000 0000 0000 101"	Acknowledgement packet needed
5	Dynamical FPGA configuration	"0000 0000 0000 010"	Acknowledgement packet needed
6	Veto	"0000 0000 0000 011"	Example: μ -TCA cannot receive the data. Acknowledgement packet needed

Table A.15: Control symbol for pre-trigger, trigger and physical data.

Item	Name	Control code	Comment
1	K.28.7	0xFC	The pre-trigger is generated by the THOR card and sent to the μ -TCA who shares it with the silicon layers cards.
2	K.23.7	0xF7	The trigger is generated by a single silicon layer card and sent to the μ -TCA who shares it with all the FE cards.
5	K.30.7	0xFE	The FE cards send the data.

silicon FE cards.

Table A.16: Pre-trigger packet

Item	1 st byte	2 nd - 4 th bytes
1	K.28.7	24 bits for the trigger number

Trigger format

This packet is sent back to the μ -TCA if a silicon FE card finds an interaction in coincidence after the reception of the pre-trigger packet. The trigger is always sent before the physical data packets. The μ -TCA then sends the trigger packet to all the FE cards (scatterer, absorber, hodoscope).

Table A.17: Trigger packet

Item	1 st byte	2 nd - 4 th bytes
1	K.23.7	24 bits for the trigger number

Physical data packet format

This packet sends the “useful” data to the μ -TCA. The data format (cargo) is defined in chapter 3.

Table A.18: Physical data packet

Item	1 st byte	Cargo	End of packet
1	K.30.7.	From 0 to Nbr-1 words of D characters	K.28.6 or the beginning of a new packet.

A.5 UDP packets format

Once the μ -TCA receives the data from the FE cards, a physical event is generated and stored in dedicated buffers. The buffers are then sent to the acquisition PC via UDP packets. Each detector section has its own UDP socket, and three receiving ports are used for the three data fluxes: 60001 for the hodoscope, 60002 for the absorber, 60003 for the scatterer. The content of the data buffers are sent in order to avoid to divide events in different packets, so that each UDP packet is completely independent from the others and contains complete events. The maximum size of a packet is set to 1500 (UDP data = 1472), or to 9000 for the so called “jumbo frames”, used for high speed acquisitions.

Each UDP packet has a custom defined header, composed of:

- 32 bits: packet number, starting from 0;

- 16 bits: number of data structures in the packet;

The data structures are then in a list one after the other with the already described format.

A.6 Data throughput expected in clinical conditions

A.6.1 Clinical intensities

In clinical standards, the beam maximum intensity is:

- protons : 10^{10} protons/s
- carbon ions : 5×10^7 C ions/s

The Compton camera must be designed in order to be able to handle the whole range of clinical intensities. The design reference is then the maximum intensity, about 3.2 nA (2×10^{10} protons/s) delivered by the cyclotron C230 by IBA. The number of proton delivered per second is higher than the maximum considered rate (10^{10} protons/s).

As shown by the simulation results, the Compton camera can not be used for an online monitoring at the maximum beam intensity for both proton and carbon ion beams. The main limitation comes from the amount of random coincidences detected by the camera for high intensity beams. One possible solution is to deliver a lower intensity beam for the range monitoring before the beginning of the treatment. The results shown here relates to a reduced intensity, corresponding to the one selected via the simulation studies.

A.6.1.1 Review: detector and target sizes

Detectors sizes:

- Silicon scatterer : 7 silicon layers, $9.6 \times 9.6 \times 0.2 \text{ cm}^3$ (first layer 20 cm far from the beam line)
- BGO absorber: BGO block $3.5 \times 3.8 \times 3.0 \text{ cm}^3$ (67.5 cm far from the beam line - center of the block)

PMMA target size: cylindrical shape, diameter 15 cm, 20 cm length along the beam direction.

A.6.2 Coincidence rate

In Table A.19 the coincidence and single (pre-trigger) rates expected for the different detector section are listed according to the beam kind and intensity. These values correspond to the Compton camera, while for the collimated camera a reduced rate is expected for the absorber due to the presence of the physical collimator.

Table A.19: Coincidence and single rate as a function of the beam intensity. The BGO single rate corresponds to the pre-trigger rate.

	Clinical intensity		Reduced intensity		Collimated camera	
	Protons	Carbon ions	Protons	Carbon ions	Protons	Carbon ions
Intensity(ions/s)	2×10^{10}	5×10^7	1×10^8	5×10^6	2×10^{10}	5×10^7
Coincidence rate per incident ion	9×10^{-4}	8×10^{-4}	9×10^{-4}	8×10^{-4}	/	/
Coincidence rate (Hz)	$1,8 \times 10^7$	4×10^4	9×10^4	4×10^3	/	/
Single rate BGO (Hz) - 96 blocks	$7,8 \times 10^7$	$1,4 \times 10^6$	$3,9 \times 10^5$	$1,4 \times 10^5$	/	/
Single rate BGO (Hz) - 1 block	$8,1 \times 10^5$	$1,5 \times 10^4$	4×10^3	$1,5 \times 10^3$	/	/
Single rate BGO (Hz) - 1 ASM card (6 blocks)	$6,5 \times 10^6$	$1,2 \times 10^5$	$3,2 \times 10^4$	$1,2 \times 10^4$	/	/

The application of the Compton camera at clinical intensity seems not feasible. The camera distance with respect to the beam line should be increased to lower the rate to 1×10^5 Hz (which means to put the 1st silicon layer 1 m far from the beam line). For a carbon ion beam at 5×10^7 Hz, the estimated coincidence rate is 4×10^4 Hz, with 1.4×10^6 single rate on the absorber (measurements of coincidence rate on the HIT accelerator adapted to a real camera size with a 40 ns coincidence window, Krimmer ANIMMA 2013). The data flow between the μ-TCA and the acquisition PC corresponds to the coincidence rate, due to the fact that only coincidence events are stored.

A.6.3 Data flow (Front End cards → μ-TCA)

The data format previously described has been used to evaluate the data flow between each FE card and the μ-TCA. The calculation is performed according to the “optimal” mode of each detector. For the BGO, we only consider events where the 4 PMs are involved. For the silicon layers, two cases are considered:

- Case 1 : one single layer with 6 involved strips;
- Case 2 : all the 7 layers involved with 6 hit strips per layer.

A Compton camera data format

Concerning the hodoscope, we considered an event with one hit fiber readout on the two sides.

The 8bits/10bits encoding is included in the calculation.

Table A.20: Data flux between FE cards and μ -TCA.

	Clinical intensity	Reduced intensity		
	<u>Protons</u>	<u>Carbon ions</u>	<u>Protons</u>	<u>Carbon ions</u>
Intensity (ions/s)	2×10^{10}	5×10^7	1×10^8	5×10^6
Pre-trigger flux (Mbits/s)	$2,5 \times 10^3$	47,6	13,3	4,76
Trigger flux (Mbits/s)	612	1,4	3,1	0,1
BGO data flux (Mbits/s) - 96 blocks	$1,7 \times 10^5$	373	873	37,3
BGO data flux (Mbits/s)- 1 block	$1,7 \times 10^3$	3,88	8,73	0,3
BGO data flux (Mbits/s) - 1 carte ASM	$1,4 \times 10^4$	31,1	69,9	3,1
Silicon data flux (Mbits/s) - case 1	$2,3 \times 10^5$	522	$1,2 \times 10^3$	52,2
Silicon data flux (Mbits/s) - case 2	$1,6 \times 10^6$	$3,7 \times 10^3$	$8,2 \times 10^3$	366
Hodoscope data flux (Mbits/s)	$8,1 \times 10^4$	180	404	18

A.6.4 Acquisition data flow (μ -TCA \rightarrow Acquisition PC)

The data flow from the μ -TCA to the acquisition PC is detailed here. The UDP encoding is included in the calculation.

Table A.21: Data flow between μ -TCA and acquisition PC.

	Clinical intensity	Reduced intensity		
	<u>Protons</u>	<u>Carbon ions</u>	<u>Protons</u>	<u>Carbon ions</u>
Intensity (ions/s)	2×10^{10}	5×10^7	1×10^8	5×10^6
Coincidence rate per incident ion	9×10^{-4}	8×10^{-4}	9×10^{-4}	8×10^{-4}
Coincidence rate (Hz)	$1,8 \times 10^7$	4×10^4	9×10^4	4×10^3
Data flow (Mbits/s) - case 1	$2,2 \times 10^4$	46,7	112	5,0
Data flow (Mbits/s) - case 2	6×10^4	133	300	13,3

A.6.5 Conclusions

As already mentioned, the Compton camera application is not feasible at clinical beam intensities.

In order to have an online monitoring of the beam range, a reduced intensity must be foreseen. The main limitation is the rate of random coincidences detected at high intensity, while from the technological point of view no limitations are highlighted by this study. In the collimated camera configuration, where no coincidences are required and the random coincidences limitation is removed, we can then expect to be able to work at real clinical intensity.

Table 7.22: Acquisition format of the Compton camera data.

COMPTON CAMERA ACQUISITION DATA FORMAT				
	Description	Size (bytes)	Size (bits)	Details
Beginning of file (10 bytes)	File start ID	2	16	FOFO (hex) fixed ID
	Run number	4	32	Automatically increasing in DAQ software - it can be manually fixed
	Total number of events	4	32	Fixed at the beginning of the acquisition, it defines the file size
Event header (11 bytes) x total number of events	Event start ID	2	16	ABCD (hex) fixed ID
	Event number	4	32	Automatically increasing in μ-TCA data format
	Trigger number	3	24	Automatically increasing in μ-TCA data format
	Number of hits in trigger	2	16	
Data header (7 bytes) x number of hits in trigger	Hit start ID	1	8	EB (hex) fixed ID
	FE number	1	8	see Table A.1
	Trigger number	3	24	repeated from Event Header
	Mode number	1	8	see figure A.4 (7 or 8 for the hodoscope - 7 = optimal, 8 = test)
	Number of involved fibers	1	8	
Hit structure scatterer (7 bytes - mode 1, 9 bytes - mode 2, mode 3 and 4 with signal sampling) x number of involved strips (mode 1 and 3) or tracks (mode 2 and 4)	Strip number	1	8	mode 1 and 3
	Position	2	16	mode 2 and 4
	Time	4	32	all modes
	Charge	2	16	mode 1 and 2
	Signal samples	2	16	mode 3 and 4 - size per sample - n samples, with n selected in acquisition code
Hit structure absorber (17 bytes - mode 5, mode 6 with signal sampling) x number of involved blocks	Block number	1	8	both modes
	Time	4	32	both modes
	Charge PM 1-4	3	24	mode 5 - size per PM - 4 PMs per block
	Signal samples	2	16	mode 6 - size per sample per PM - n samples, with n selected in acquisition code, 4 PMs per block
Hit structure hodoscope (5 bytes - mode 7, 7 bytes - mode 8) x number of involved fibers	Fiber number	1	8	ranges from 0 to 128
	Time	4	32	in both modes 7 and 8
	Charge	2	16	only for mode 8
End of file (10 bytes)	File end ID	2	16	F1F1 (hex) fixed ID
	Number of events in file	4	32	for verification and debugging
	Number of octets in file	4	32	for verification and debugging

List of abbreviations

[¹¹¹ In]	Indium-111	see p. 86
[¹³¹ I]	Iodine-131	see p. 80, 86
[¹³¹ In]	Indium-131	see p. 4
[²² Na]	Sodium-22	see p. viii, 45–51, 53, 59–61
[⁴² K]	Potassium-42	see p. 86
[⁵⁷ Co]	Cobalt-57	see p. 45
[⁵⁹ Fe]	Iron-59	see p. 86
[⁶⁰ Co]	Cobalt-60	see p. viii, 46, 48, 49, 53–55, 57
[^{91m} Y]	Yttrium-91m	see p. 86
[μ -TCA]	Micro Advanced Telecommunications Computing Architecture	see p. v, vii, x, xi, 30, 36–38, 40, 71–75, 107–110, 115, 117–123, 125, 126, 128
[ADC]	Analog-to-Digital Converter	see p. 24, 29, 33, 46–48, 51, 58, 59, 64
[AMC]	Advanced Mezzanine Card	see p. vii, 37–39, 71, 74
[ASIC]	Application-Specific Integrated Circuit	see p. 24, 32, 33, 35, 40, 45, 71, 111, 114
[ASM]	Analog Sampling Module	see p. vii, 29, 30, 37, 72, 108–111, 125, 126
[ATCA]	Advanced Telecommunications Computing Architecture	see p. 36
[AVIRM]	Application et Valorisation des Interactions Rayonnements-Matière	see p. 28–30, 64
[BaF ₂]	Barium Fluoride	see p. 50, 51, 62
[BGO]	Bismuth Germanium Oxide - Bi ₁₂ GeO ₂₀	see p. i, iv, vii, viii, x, xi, 19, 26–31, 36, 43, 44, 46–48, 50, 51, 59, 61–63, 72, 83, 84, 94, 109, 111, 120, 124–126
[BNCT]	Boron Neutron Capture Therapy	see p. 12
[CAL]	Centre Antoine Lacassagne, Nice, France	see p. 39

List of abbreviations

[CdTe]	Cadmium Telluride	see p. ix, 84, 92, 93
[CeBr ₃]	Cerium Bromide	see p. 73
[CERN]	Conseil Européen pour la Recherche Nucléaire, Geneva, Switzerland	see p. 37
[CLaRyS]	Contrôle en Ligne de l'hadronthérapie par Rayonnements Secondaires	see p. i, ii, 20, 22, 31, 36, 43, 44, 70, 80, 81, 92, 95, 98, 100
[CPPM]	Centre de Physique des Particules de Marseille, France	see p. 20, 37, 74
[CR-RC]	Capacitor Resistor - Resistor Capacitor	see p. 24
[CREATIS]	Centre de Recherche en Acquisition et Traitement de l'Image pour la Santé, Lyon, France	see p. 20, 43, 84
[CSA]	Charge Sensitive Amplifier	see p. 24
[CSDA]	Continuous Slowing Down Approach	see p. 7
[CT]	Computed Tomography	see p. i
[DLL]	Delay Locked Loop	see p. 33
[DPGA]	Détecteur Pixélisé de Grande Acceptance	see p. 20, 29
[DRS]	Domino Ring Sampler	see p. 29
[DSSD]	Double-sided Silicon Strip Detector	see p. i, 22–24, 44, 45, 71, 83, 85, 98
[ENC]	Equivalent Noise Charge	see p. 24, 83, 92, 93, 98
[ESRF]	European Synchrotron Radiation Facility, Grenoble, France	see p. 74
[FE]	Front-End	see p. vii, xi, 23–26, 29, 31, 32, 34–37, 45, 46, 66, 71–75, 107–111, 114, 118, 119, 121–123, 125, 126, 128
[FPGA]	Field Programmable Gate Array	see p. 24, 25, 29, 30, 33, 35, 37, 114, 117, 121, 122
[FWHM]	Full Width at Half Maximum	see p. x, 24, 36, 45, 51, 59, 62–64, 72, 83, 84, 94
[GANIL]	Grand Accelerateur National d'Ions Lourds, Caen, France	see p. 33, 36, 72, 74, 83
[GATE]	GEANT4 Application for Tomographic Emission	see p. 86

[GEANT4]	GEometry And Tracking 4	see p. 81
[GSPS]	Giga Sample Per Second	see p. 29
[HEGP]	High Energy General Purpose	see p. 86, 99
[HIT]	Heidelberg Ion Therapy Center, Germany	see p. 5, 33, 36
[HSMC]	High-Speed Mezzanine Card	see p. 30
[IPNL]	Institut de Physique Nucléaire de Lyon, France	see p. 20, 23–25, 30, 32, 37, 40, 44, 46, 47, 64, 71–74, 83
[IPNO]	Institut de Physique Nucléaire d'Orsay, France	see p. 36
[IRFU]	Institut de Recherche sur les lois Fondamentales de l'Univers, Paris, France	see p. 47
[LaBr₃]	Lanthanum Bromide	see p. 45
[LAL]	Laboratoire de l'Accélérateur Linéaire, Paris, France	see p. 47
[LED]	Light Emitting Diode	see p. ix, 62, 64, 66–69
[LET]	Linear Energy Transfer	see p. 13
[LHCb]	Large Hadron Collider beauty	see p. 37
[LM-MLEM]	List Mode-Maximum Likelihood Expectation Maximization	see p. 43, 84, 92–94, 98, 99
[LPC]	Laboratoire de Physique de Clermont, France	see p. 20, 28–30, 37, 64
[LPSC]	Laboratoire de Physique Subatomique et Corpusculaire, Grenoble, France	see p. 20, 74
[LSO]	Cerium-doped Lutetium Oxyorthosilicate - $\text{Lu}_{2(1-x)}\text{Ce}_{2x}\text{SiO}_4$	see p. 27
[LVDS]	Low-Voltage Differential Signaling	see p. 24
[LYSO]	Lutetium-Yttrium OxyorthoSilicate - $\text{Lu}_{2(1-x)}\text{Y}_{2x}\text{SiO}_5$	see p. 27, 29, 73
[MCH]	μ -TCA Carrier HUB	see p. 37
[MCS]	Multiple Coulomb Scattering	see p. 8
[MEGAlib]	Medium-Energy Gamma-ray Astronomy library	see p. 84

List of abbreviations

[MICRHAU]	Micro-électronique RHône AUvergne	see p. 32
[MRI]	Magnetic Resonance Imaging	see p. 4
[MSPS]	Mega Sample Per Second	see p. 24
[NaI(Tl)]	Sodium Iodide doped with Thallium	see p. 86, 87
[NIM]	Nuclear Instrumentation Module	see p. 44–47, 50, 51, 72
[PET]	Positron Emission Tomography	see p. i, 4, 14, 20, 26, 29, 31, 46, 72, 80
[PM]	Photo-Multiplier	see p. iv, viii, ix, 19, 27–30, 32–36, 46–48, 51–53, 62–70, 72, 73, 111, 114, 125, 128
[PMMA]	Poly Methyl Metacrylate	see p. 30, 124
[PSI]	Paul Scherrer Institut, Villigen, Switzerland	see p. 29
[RAM]	Random Access Memory	see p. 39
[RBE]	Relative Biological Effectiveness	see p. 13
[RMS]	Root Mean Square	see p. 24, 33, 74, 94
[SHS]	Slow Shaper	see p. 24
[SPECT]	Single Photon Emission Computed Tomography	see p. i, 80, 81, 83, 86, 92, 98, 99
[SPTR]	Single Photon Time Resolution	see p. 73
[TCP]	Transmission Control Protocol	see p. 37, 40
[TDC]	Time-to-Digital Converter	see p. 24, 33, 107
[THOR]	Trigger et HORloge	see p. vii, 29, 37, 38, 72, 109, 110, 121, 122
[TOF]	Time-Of-Flight	see p. 20–22, 31, 36, 44, 72–74
[UDP]	User Datagram Protocol	see p. 37, 40, 74
[USB]	Universal Serial Bus	see p. 47

[VME] VERSABUS Module Eurocard see p. 29, 37, 45, 72

Bibliography

- Abellan, C., J.-. P Cachemiche, F. Réthoré, and C. Morel (June 2013). “A data acquisition system for medical imaging”. In: *2013 3rd International Conference on Advancements in Nuclear Instrumentation, Measurement Methods and their Applications (ANIMMA)*, pp. 1–7. DOI: 10.1109/ANIMMA.2013.6728028 (cit. on p. 37).
- Adam, L. E., J. Zaers, H. Ostertag, H. Trojan, M. E. Bellemann, and G. Brix (June 1997). “Performance evaluation of the whole-body PET scanner ECAT EXACT HR + following the IEC standard”. In: *IEEE Transactions on Nuclear Science* 44.3, pp. 1172–1179. ISSN: 0018-9499. DOI: 10.1109/23.596983 (cit. on p. 26).
- Altera (2009). *Stratix II GX Device Handbook*. Volume 1. Altera Corporation (cit. on pp. 24, 35).
- Altera (2012). *Cyclone III Device Handbook*. Volume 1. Altera Corporation (cit. on pp. 24, 33).
- Altera (2015). *Stratix V Device Handbook*. Volume 3. Altera Corporation (cit. on p. 29).
- Altera (2016). *Cyclone IV Device Handbook*. Volume 1. Altera Corporation (cit. on p. 37).
- Anger, H. O. (1958). “Scintillation Camera”. In: *Review of Scientific Instruments* 29.1, pp. 27–33. DOI: 10.1063/1.1715998. eprint: <http://dx.doi.org/10.1063/1.1715998>. URL: <http://dx.doi.org/10.1063/1.1715998> (cit. on p. 80).
- Anger, H. O. (1964). “Scintillation Camera with Multichannel Collimators”. In: *Journal of Nuclear Medicine* 5.7, pp. 515–531. eprint: <http://jnm.snmjournals.org/content/5/7/515.full.pdf+html>. URL: <http://jnm.snmjournals.org/content/5/7/515.short> (cit. on p. 80).
- Aspen Aerogels (2011). *Spaceloft® - High performance Insulation for building envelopes. Data Sheet*. Aspen Aerogels Inc. (cit. on p. 25).
- Barth, R. F., J. A. Coderre, M. G. H. Vicente, and T. E. Blue (2005). “Boron Neutron Capture Therapy of Cancer: Current Status and Future Prospects”. In: *Clinical Cancer Research* 11.11, pp. 3987–4002. DOI: 10.1158/1078-0432.CCR-05-0035. eprint: <http://clincancerres.aacrjournals.org/content/11/11/3987.full.pdf>. URL: <http://clincancerres.aacrjournals.org/content/11/11/3987> (cit. on p. 12).
- Baskar, R., K. A. Lee, R. Yeo, and K.-W. Yeoh (2012). “Cancer and radiation therapy: current advances and future directions.” eng. In: *Int J Med Sci* 9.3, pp. 193–199. DOI: 10.7150/ijms.3635 (cit. on p. 5).
- Basko, R., G. L. Zeng, and G. T. Gullberg (1998). “Application of spherical harmonics to image reconstruction for the Compton camera”. In: *Physics in Medicine and Biology* 43.4, p. 887. URL: <http://stacks.iop.org/0031-9155/43/i=4/a=016> (cit. on p. 18).
- Bauer, J., D. Unholtz, F. Sommerer, C. Kurz, T. Haberer, K. Herfarth, T. Welzel, S. E. Combs, J. Debus, and K. Parodi (2013). “Implementation and initial clinical experience of offline

- PET/CT-based verification of scanned carbon ion treatment". In: *Radiotherapy and Oncology* 107.2, pp. 218–226. ISSN: 0167-8140. DOI: <https://doi.org/10.1016/j.radonc.2013.02.018>. URL: <http://www.sciencedirect.com/science/article/pii/S0167814013001606> (cit. on p. 14).
- Bentzen, S. M. (2006). "Preventing or reducing late side effects of radiation therapy: radiobiology meets molecular pathology." eng. In: *Nat Rev Cancer* 6.9, pp. 702–713. DOI: 10.1038/nrc1950 (cit. on p. 5).
- Bethe, H. (1930). "Zur Theorie des Durchgangs schneller Korpuskularstrahlen durch Materie". In: *Annalen der Physik* 397.3, pp. 325–400. DOI: 10.1002/andp.19303970303. eprint: <https://onlinelibrary.wiley.com/doi/pdf/10.1002/andp.19303970303>. URL: <https://onlinelibrary.wiley.com/doi/abs/10.1002/andp.19303970303> (cit. on p. 7).
- Bhat, M. R. (1992). *Evaluated Nuclear Structure Data File (ENSDF), Nuclear Data for Science and Technology, page 817, edited by S. M. Qaim* (SpringerVerlag, Berlin, Germany, 1992). URL: <https://www.nndc.bnl.gov/> (visited on 03/27/2017) (cit. on p. 82).
- Blakely, E. A. and P. Y. Chang (2009). "Biology of charged particles." eng. In: *Cancer J* 15.4, pp. 271–284. DOI: 10.1097/PPO.0b013e3181b666c5 (cit. on p. 5).
- Bloch, F. (1933). "Zur Bremsung rasch bewegter Teilchen beim Durchgang durch Materie". In: *Annalen der Physik* 408.3, pp. 285–320. DOI: 10.1002/andp.19334080303. eprint: <https://onlinelibrary.wiley.com/doi/pdf/10.1002/andp.19334080303>. URL: <https://onlinelibrary.wiley.com/doi/abs/10.1002/andp.19334080303> (cit. on p. 7).
- Bohr, N. (1915). "On the decrease of velocity of swiftly moving electrified particles in passing through matter". In: *The London, Edinburgh, and Dublin Philosophical Magazine and Journal of Science* 30.178, pp. 581–612. DOI: 10.1080/14786441008635432. eprint: <https://doi.org/10.1080/14786441008635432>. URL: <https://doi.org/10.1080/14786441008635432> (cit. on p. 7).
- Bothe, W. (Jan. 1921). "Das allgemeine Fehlergesetz, die Schwankungen der Feldstärke in einem Dielektrikum und die Zerstreuung dera α -Strahlen". In: *Zeitschrift für Physik* 5.1, pp. 63–69. DOI: 10.1007/BF01349687. URL: <https://doi.org/10.1007/BF01349687> (cit. on p. 8).
- Braccini, S. (2010). "Scientific and technological development of hadrontherapy". In: *Astroparticle, Particle and Space Physics, Detectors and Medical Physics Applications*, pp. 598–609. DOI: 10.1142/9789814307529_0099. eprint: https://www.worldscientific.com/doi/pdf/10.1142/9789814307529_0099. URL: https://www.worldscientific.com/doi/abs/10.1142/9789814307529_0099 (cit. on p. 11).
- Bragg, W. H. M. A. and R. Kleeman (1904). "On the ionization curves of radium". In: *The London, Edinburgh, and Dublin Philosophical Magazine and Journal of Science* 8.48, pp. 726–738. DOI: 10.1080/14786440409463246. eprint: <https://doi.org/10.1080/14786440409463246>. URL: <https://doi.org/10.1080/14786440409463246> (cit. on p. 6).
- Bragg, W. H. M. A. and R. Kleeman (1905). "On the α particles of radium, and their loss of range in passing through various atoms and molecules". In: *The London, Edinburgh, and*

- Dublin Philosophical Magazine and Journal of Science* 10.57, pp. 318–340. DOI: 10.1080/14786440509463378. eprint: <https://doi.org/10.1080/14786440509463378>. URL: <https://doi.org/10.1080/14786440509463378> (cit. on pp. 6, 7).
- Brahme, A. (2004). “Recent advances in light ion radiation therapy”. In: *International Journal of Radiation Oncology Biology Physics* 58.2, pp. 603–616. DOI: 10.1016/j.ijrobp.2003.09.034. URL: <http://dx.doi.org/10.1016/j.ijrobp.2003.09.034> (cit. on p. 5).
- Breton, D., E. Delagnes, J. Maalmi, and P. Rusquart (May 2014). “The WaveCatcher family of SCA-based 12-bit 3.2-GS/s fast digitizers”. In: *2014 19th IEEE-NPSS Real Time Conference*, pp. 1–8. DOI: 10.1109/RTC.2014.7097545 (cit. on p. 47).
- Brix, G., J. Zaers, L.-E. Adam, M. E. Bellemann, H. Ostertag, H. Trojan, U. Haberkorn, J. Doll, F. Oberdorfer, and W. Lorenz (1997). “Performance Evaluation of a Whole-Body PET Scanner Using the NEMA Protocol”. In: *Journal of Nuclear Medicine* 38.10, pp. 1614–1623. eprint: <http://jnm.snmjournals.org/content/38/10/1614.full.pdf+html>. URL: <http://jnm.snmjournals.org/content/38/10/1614.short> (cit. on p. 26).
- Brun, R. and F. Rademakers (1997). “ROOT: An object oriented data analysis framework”. In: *Nucl. Instrum. Meth.* A389, pp. 81–86. DOI: 10.1016/S0168-9002(97)00048-X (cit. on pp. 39–41, 49).
- Brunner, S. E., L. Gruber, A. Hirtl, K. Suzuki, J. Marton, and D. R. Schaart (2016). “A comprehensive characterization of the time resolution of the Philips Digital Photon Counter”. In: *Journal of Instrumentation* 11.11, P11004. URL: <http://stacks.iop.org/1748-0221/11/i=11/a=P11004> (cit. on p. 73).
- Cachemiche, J.-P., P. Y. Duval, F. Hachon, R. Le Gac, and F. Réthoré (Sept. 2012). “xTCA developments in Marseille for the LHCb Readout”. In: *TWEPP 2012 Topical Workshop on Electronics for Particle Physics*. Oxford, United Kingdom. URL: <http://hal.in2p3.fr/in2p3-00757616> (cit. on p. 37).
- Cantor, D. (Apr. 1988). “Pioneers and early years. A history of British radiology”. In: *Medical History* 32.2, pp. 224–224. URL: <http://www.ncbi.nlm.nih.gov/pmc/articles/PMC1139872/> (cit. on p. 4).
- Catterall, M., C. Rogers, R. H. Thomlinson, and S. B. Field (1971). “An investigation into the clinical effects of fast neutrons”. In: *The British Journal of Radiology* 44.524. PMID: 4997649, pp. 603–611. DOI: 10.1259/0007-1285-44-524-603. eprint: <https://doi.org/10.1259/0007-1285-44-524-603>. URL: <https://doi.org/10.1259/0007-1285-44-524-603> (cit. on p. 12).
- Cecchin, D., D. Poggiali, L. Riccardin, P. Turco, F. Bui, and S. De Marchi (2015). “Analytical and experimental FWHM of a gamma camera: theoretical and practical issues.” In: *PeerJ* 3:e722 (cit. on p. 92).
- Chen, X. (2017). “Développement de cartes Front-End avec leur firmware associé pour un hodoscope de faisceau et un diffuseur silicium utilisées pour le contrôle de dose en ligne en hadronthérapie.” Mémoire for CNAM engineer degree in Electronic Systems (cit. on pp. 25, 35).

- Coudurier, V. (2015). “Caractérisation d'un hodoscope de faisceau pour l'hadronthérapie”. Master internship report (cit. on p. 64).
- Cree, M. J. and P. J. Bones (June 1994). “Towards direct reconstruction from a gamma camera based on Compton scattering”. In: *IEEE Transactions on Medical Imaging* 13.2, pp. 398–407. DOI: 10.1109/42.293932 (cit. on p. 18).
- Dahoumane, M., D. Dauvergne, J. Krimmer, J.-L. Ley, É. Testa, and Y. Zoccarato (Nov. 2014). “A low noise and high dynamic range CMOS integrated Electronics associated with double sided Silicon Strip Detectors for a Compton camera gamma-ray detecting system”. In: *2014 IEEE Nuclear Science Symposium and Medical Imaging Conference (NSS/MIC)*, pp. 1–6. DOI: 10.1109/NSSMIC.2014.7431122 (cit. on p. 24).
- Dahoumane, M., D. Dauvergne, J. Krimmer, H. Mathez, C. Ray, É. Testa, A. H. Walenta, and Y. Zoccarato (Oct. 2012). “A low noise and high dynamic charge sensitive amplifier-shaper associated with Silicon Strip Detector for compton camera in hadrontherapy”. In: *2012 IEEE Nuclear Science Symposium and Medical Imaging Conference Record (NSS/MIC)*, pp. 1445–1451. DOI: 10.1109/NSSMIC.2012.6551351 (cit. on p. 25).
- Degiovanni, A. and U. Amaldi (2015). “History of hadron therapy accelerators”. In: *Physica Medica* 31.4, pp. 322–332. ISSN: 1120-1797. DOI: <https://doi.org/10.1016/j.ejmp.2015.03.002>. URL: <http://www.sciencedirect.com/science/article/pii/S1120179715000629> (cit. on p. 11).
- Deng, S.-M. (2012). “Etude de conception d'ASICs de lecture et d'étiquetage en temps associés à des photomultiplicateurs pour un hodoscope de faisceau en hadronthérapie”. PhD thesis. École Doctorale EEA (Électronique, Électrotechnique et Automatique), Université Claude Bernard - Lyon 1 (cit. on p. 33).
- Deng, S.-M., H. Mathez, D. Dauvergne, G.-N. Lu, and Y. Zoccarato (2012). “Front-end multi-channel PMT-associated readout chip for hodoscope application”. In: *Nuclear Instruments and Methods in Physics Research Section A: Accelerators, Spectrometers, Detectors and Associated Equipment* 695. New Developments in Photodetection NDIP11, pp. 390–393. ISSN: 0168-9002. DOI: <https://doi.org/10.1016/j.nima.2011.11.042>. URL: <http://www.sciencedirect.com/science/article/pii/S0168900211020845> (cit. on p. 33).
- Deng, S.-M., H. Mathez, D. Dauvergne, Y. Zoccarato, and G.-N. Lu (Jan. 2013). “Very fast front end ASIC associated with multi-anode PMTs for a scintillating-fibre beam hodoscope”. In: *Journal of Instrumentation* 8, p. C01047. DOI: 10.1088/1748-0221/8/01/C01047. URL: <https://hal.archives-ouvertes.fr/hal-00990850> (cit. on p. 33).
- Despeignes, V. (1896). “Observations on a case of cancer of the stomach treated by Röntgen rays.” In: *Lyon Medical Journal* 82, p. 428 (cit. on p. 4).
- Duck, F. A. (June 2014). “The origins of medical physics”. In: *Physica Medica: European Journal of Medical Physics* 30.4, pp. 397–402. DOI: 10.1016/j.ejmp.2014.03.005. URL: <http://dx.doi.org/10.1016/j.ejmp.2014.03.005> (cit. on p. 4).

- Durante, M. and J. S. Loeffler (Dec. 2009). "Charged particles in radiation oncology". In: *Nature Reviews Clinical Oncology* 7, p. 37. URL: <http://dx.doi.org/10.1038/nrclinonc.2009.183> (cit. on p. 5).
- Durante, M. and H. Paganetti (2016). "Nuclear physics in particle therapy: a review". In: *Reports on Progress in Physics* 79.9, p. 096702. URL: <http://stacks.iop.org/0034-4885/79/i=9/a=096702> (cit. on pp. 5, 7–10).
- Elftmann, R., J. Tammen, S. R. Kulkarni, C. Martin, S. Böttcher, and R. Wimmer-Schweingruber (2015). "Characterization of an LSO scintillator for space applications". In: *Journal of Physics: Conference Series* 632.1, p. 012006. URL: <http://stacks.iop.org/1742-6596/632/i=1/a=012006> (cit. on p. 27).
- Enghardt, W., P. Crespo, F. Fiedler, R. Hinz, K. Parodi, J. Pawelke, and F. Pönisch (2004). "Charged hadron tumour therapy monitoring by means of PET". In: *Nuclear Instruments and Methods in Physics Research Section A: Accelerators, Spectrometers, Detectors and Associated Equipment* 525.1. Proceedings of the International Conference on Imaging Techniques in Subatomic Physics, Astrophysics, Medicine, Biology and Industry, pp. 284–288. ISSN: 0168-9002. DOI: <https://doi.org/10.1016/j.nima.2004.03.128>. URL: <http://www.sciencedirect.com/science/article/pii/S0168900204004218> (cit. on p. 14).
- Evans, T. C. (1951). "X-Ray Treatment-Its Origin, Birth and Early History. Emil H. Grubbe". In: *The Quarterly Review of Biology* 26.2, pp. 223–223. DOI: 10.1086/398163. eprint: <https://doi.org/10.1086/398163>. URL: <https://doi.org/10.1086/398163> (cit. on p. 4).
- Everett, D. B., J. S. Fleming, R. W. Todd, and J. M. Nightingale (1977). "Gamma-radiation imaging system based on the Compton effect". In: *Proceedings of the Institution of Electrical Engineers* 124.11, p. 995. ISSN: 0020-3270. DOI: 10.1049/piee.1977.0203 (cit. on p. 80).
- Fontana, M., D. Dauvergne, J. M. Létang, J.-L. Ley, and É. Testa (2017a). "Compton camera study for high efficiency SPECT and benchmark with Anger system". In: *Physics in Medicine and Biology* 62.23, p. 8794. URL: <http://stacks.iop.org/0031-9155/62/i=23/a=8794> (cit. on p. 79).
- Fontana, M., D. Dauvergne, J.-L. Ley, J. M. Létang, V. Maxim, and É. Testa (2017b). "Versatile Compton camera for high energy gamma rays: Monte Carlo comparison with Anger camera for medical imaging". In: *2nd Jagiellonian Symposium on Fundamental and Applied Subatomic Physics*. Vol. 48. Krakow, Poland, pp. 1639–1645. DOI: 10.5506/APhysPolB.48.1639. URL: <https://hal.archives-ouvertes.fr/hal-01609541> (cit. on p. 79).
- Foray, N. (Nov. 2016). "Victor Despeignes, the Forgotten Pioneer of Radiation Oncology." eng. In: *Int J Radiat Oncol Biol Phys* 96.4, pp. 717–721. DOI: 10.1016/j.ijrobp.2016.07.019 (cit. on p. 4).
- Friedrich, T., U. Scholz, T. Elsässer, M. Durante, and M. Scholz (2012). "Calculation of the biological effects of ion beams based on the microscopic spatial damage distribution pattern". In: *International Journal of Radiation Biology* 88.1-2, pp. 103–107. DOI: 10.3109/09553002.2011.611213. eprint: <https://doi.org/10.3109/09553002.2011.611213>. URL: <https://doi.org/10.3109/09553002.2011.611213> (cit. on p. 5).

Bibliography

- Gaglione, R. (2013). "Electronique d'acquisition d'une gamma-caméra." PhD thesis. École Doctorale Sciences pour l'ingénieur de Clermont-Ferrand (cit. on p. 64).
- Gallin-Martel, M.-L., Abbassi, L., Bes, A., Bosson, G., Collot, J., Crozes, T., Curtoni, S., Dauvergne, D., De Nolf, W., Fontana, M., Gallin-Martel, L., Hostachy, J.-Y., Krimmer, J., Lacoste, A., Marcatili, S., Morse, J., Motte, J.-F., Muraz, J.-F., Rarbi, F. E., Rossetto, O., Salomé, M., Testa, É., Vuiart, R., and Yamouni, M. (2018). "A large area diamond-based beam tagging hodoscope for ion therapy monitoring". In: *EPJ Web Conf.* 170, p. 09005. DOI: 10.1051/epjconf/201817009005. URL: <https://doi.org/10.1051/epjconf/201817009005> (cit. on p. 74).
- Gallin-Martel, M.-L., A. Bes, A. Boukhémiri, G. Bosson, J. Collot, D. Dauvergne, M. Fontana, L. Gallin-Martel, A. Gorecki, J. Y. Hostachy, J. Krimmer, A. Lacoste, S. Marcatili, J. Morse, J. F. Muraz, F. E. Rarbi, O. Rossetto, M. Salomé, É. Testa, and M. Yamouni (2016). "Large area polycrystalline diamond detectors for online hadron therapy beam tagging applications". In: *2016 IEEE Nuclear Science Symposium, Medical Imaging Conference and Room-Temperature Semiconductor Detector Workshop (NSS/MIC/RTSD)*, pp. 1–5. DOI: 10.1109/NSSMIC.2016.8069398 (cit. on p. 74).
- GE Healthcare (June 2006). "Infinia". In: Release 2.5 (cit. on pp. 80, 86).
- GeckoDrive (2010). *G203V stepper drive - data sheet*. REV7. GeckoDrive Motor Controls Inc. (cit. on p. 64).
- Gillam, J. E., C. Lacasta, I. Torres-Espallardo, C. Candela Juan, G. Llosá, P. Solevi, J. Barrio, and M. Rafecas (2011). "A Compton imaging algorithm for on-line monitoring in hadron therapy". In: vol. 7961, pp. 7961–8. DOI: 10.1117/12.877678. URL: <https://doi.org/10.1117/12.877678> (cit. on p. 18).
- Golnik, C. (2015). "Treatment verification in proton therapy based on the detection of prompt gamma-rays." PhD thesis. TU Dresden and Oncoray (cit. on pp. 46, 72).
- Gottschalk, B. (Dec. 2006). "Neutron dose in scattered and scanned proton beams: in regard to Eric J. Hall (Int J Radiat Oncol Biol Phys 2006;65:1-7)." eng. In: *Int J Radiat Oncol Biol Phys* 66.5, p. 1595. DOI: 10.1016/j.ijrobp.2006.08.014 (cit. on p. 11).
- Gottschalk, B., A. M. Koehler, R. J. Schneider, J. M. Sisterson, and M. S. Wagner (1993). "Multiple Coulomb scattering of 160 MeV protons". In: *Nuclear Instruments and Methods in Physics Research Section B: Beam Interactions with Materials and Atoms* 74.4, pp. 467–490. ISSN: 0168-583X. DOI: [https://doi.org/10.1016/0168-583X\(93\)95944-Z](https://doi.org/10.1016/0168-583X(93)95944-Z). URL: <http://www.sciencedirect.com/science/article/pii/0168583X9395944Z> (cit. on p. 8).
- Grassberger, C. and H. Paganetti (2011). "Elevated LET components in clinical proton beams". In: *Physics in Medicine and Biology* 56.20, p. 6677. URL: <http://stacks.iop.org/0031-9155/56/i=20/a=011> (cit. on p. 10).
- Gunzert-Marx, K., H. Iwase, D. Schardt, and R. S. Simon (2008). "Secondary beam fragments produced by 200 MeV/u ^{12}C ions in water and their dose contributions in carbon ion

radiotherapy”. In: *New Journal of Physics* 10.7, p. 075003. URL: <http://stacks.iop.org/1367-2630/10/i=7/a=075003> (cit. on p. 10).

Haettner, E., H. Iwase, M. Krämer, G. Kraft, and D. Schardt (2013). “Experimental study of nuclear fragmentation of 200 and 400 MeV/u C ions in water for applications in particle therapy”. In: *Physics in Medicine and Biology* 58.23, p. 8265. URL: <http://stacks.iop.org/0031-9155/58/i=23/a=8265> (cit. on p. 10).

Haettner, E., H. Iwase, and D. Schardt (2006). “Experimental fragmentation studies with ^{12}C therapy beams”. In: *Radiation Protection Dosimetry* 122.1-4, pp. 485–487. DOI: 10.1093/rpd/ncl402. URL: <http://dx.doi.org/10.1093/rpd/ncl402> (cit. on p. 10).

Halperin, E. C. (2006). “Particle therapy and treatment of cancer”. In: *The Lancet Oncology* 7.8, pp. 676–685. DOI: 10.1016/S1470-2045(06)70795-1. URL: [http://dx.doi.org/10.1016/S1470-2045\(06\)70795-1](http://dx.doi.org/10.1016/S1470-2045(06)70795-1) (cit. on p. 5).

Hamamatsu (1995). *Metal Package Photomultiplier Tube R5600 Series*. TPMH1066E08. Hamamatsu Photonics K. K. (cit. on p. 64).

Hamamatsu (2006). *Flat Panel Type Multianode Photomultiplier Tube Assembly H8500, H8500B*. TPMH1282E09. Hamamatsu Photonics K. K. (cit. on pp. 32, 62, 69).

Han, L., W. L. Rogers, S. S. Huh, and N. Clinthorne (2008). “Statistical performance evaluation and comparison of a Compton medical imaging system and a collimated Anger camera for higher energy photon imaging”. In: *Physics in Medicine and Biology* 53.24, p. 7029. URL: <http://stacks.iop.org/0031-9155/53/i=24/a=002> (cit. on pp. 80, 81, 83, 98).

Highland, V. L. (1975). “Some practical remarks on multiple scattering”. In: *Nuclear Instruments and Methods* 129.2, pp. 497–499. DOI: [https://doi.org/10.1016/0029-554X\(75\)90743-0](https://doi.org/10.1016/0029-554X(75)90743-0). URL: <http://www.sciencedirect.com/science/article/pii/0029554X75907430> (cit. on p. 8).

Hilaire, E., C. Robert, X. Lojacono, D. Sarrut, I. Buvat, F. Peyrin, and V. Maxim (Feb. 2014). “Compton imaging in proton therapy: reconstructed image of the simulated prompt- γ distribution”. In: *ICTR-PHE 2014*. Genève, Switzerland, S43. URL: <https://hal.archives-ouvertes.fr/hal-01052717> (cit. on p. 43).

Hirasawa, M. and T. Tomitani (Apr. 21, 2003). “An analytical image reconstruction algorithm to compensate for scattering angle broadening in Compton cameras.” eng. In: *Phys Med Biol* 48.8, pp. 1009–1026 (cit. on p. 18).

Hishikawa, Y., K. Kagawa, M. Murakami, H. Sakai, T. Akagi, and M. Abe (2002). “Usefulness of positron-emission tomographic images after proton therapy”. In: *International Journal of Radiation Oncology *Biology *Physics* 53.5, pp. 1388–1391. DOI: 10.1016/S0360-3016(02)02887-0. URL: [http://dx.doi.org/10.1016/S0360-3016\(02\)02887-0](http://dx.doi.org/10.1016/S0360-3016(02)02887-0) (cit. on p. 14).

Hubbell, J. H. and M. J. Berger (1987). *XCOM: Photon Cross Sections on a Personal Computer, Report NBSIR 87-3597* (1987), National Institute for Standards and Technology, U.S.A. URL: <http://physics.nist.gov/PhysRefData/XrayMassCoef/> (visited on 02/21/2017) (cit. on pp. 87, 99).

- Hueso-González, F., A. K. Biegun, P. Dendooven, W. Enghardt, F. Fiedler, C. Golnik, K. Heidel, T. Kormoll, J. Petzoldt, K. E. Römer, R. Schwengner, A. Wagner, and G. Pausch (2015). “Comparison of LSO and BGO block detectors for prompt gamma imaging in ion beam therapy”. In: *Journal of Instrumentation* 10.09, P09015. URL: <http://stacks.iop.org/1748-0221/10/i=09/a=P09015> (cit. on pp. 27, 46, 72).
- Hüfner, J., K. Schäfer, and B. Schürmann (Dec. 1975). “Abrasion-ablation in reactions between relativistic heavy ions”. In: *Phys. Rev. C* 12 (6), pp. 1888–1898. DOI: 10.1103/PhysRevC.12.1888. URL: <https://link.aps.org/doi/10.1103/PhysRevC.12.1888> (cit. on p. 9).
- ICRU (1980). “ICRU Report 33 - Radiation Quantities and Units”. In: *Journal of the International Commission on Radiation Units and Measurements, Bethesda, MD* (cit. on p. 13).
- ICRU (1998). “ICRU Report 60 - Fundamental Quantities and Units for Ionising Radiation”. In: *Journal of the International Commission on Radiation Units and Measurements, Bethesda, MD* (cit. on p. 13).
- Jemal, A., M. M. Center, C. DeSantis, and E. M. Ward (2010). “Global Patterns of Cancer Incidence and Mortality Rates and Trends”. In: *Cancer Epidemiology and Prevention Biomarkers* 19.8, pp. 1893–1907. ISSN: 1055-9965. DOI: 10.1158/1055-9965.EPI-10-0437. eprint: <http://cebp.aacrjournals.org/content/19/8/1893.full.pdf>. URL: <http://cebp.aacrjournals.org/content/19/8/1893> (cit. on p. 4).
- Kabuki, S., K. Hattori, R. Kohara, E. Kunieda, A. Kubo, H. Kubo, K. Miuchi, T. Nakahara, T. Nagayoshi, H. Nishimura, Y. Okada, R. Orito, H. Sekiya, T. Shirahata, A. Takada, T. Tanimori, and K. Ueno (2007). “Development of Electron Tracking Compton Camera using micro pixel gas chamber for medical imaging”. In: *Nuclear Instruments and Methods in Physics Research Section A: Accelerators, Spectrometers, Detectors and Associated Equipment* 580.2. Imaging 2006, pp. 1031–1035. ISSN: 0168-9002. DOI: <https://doi.org/10.1016/j.nima.2007.06.098>. URL: <http://www.sciencedirect.com/science/article/pii/S0168900207013186> (cit. on p. 99).
- Keevil, S. F. (2012). “Physics and medicine: a historical perspective”. In: *The Lancet* 379.9825, pp. 1517–1524. ISSN: 0140-6736. DOI: [https://doi.org/10.1016/S0140-6736\(11\)60282-1](https://doi.org/10.1016/S0140-6736(11)60282-1). URL: <http://www.sciencedirect.com/science/article/pii/S0140673611602821> (cit. on p. 4).
- Kereiakes, J. G. (1987). “The history and development of medical physics instrumentation: Nuclear medicine”. In: *Medical Physics* 14.1, pp. 146–155. DOI: 10.1118/1.596105. eprint: <https://aapm.onlinelibrary.wiley.com/doi/pdf/10.1118/1.596105>. URL: <https://aapm.onlinelibrary.wiley.com/doi/abs/10.1118/1.596105> (cit. on p. 4).
- Knoll, G. F. (2000). *Radiation Detection and Measurement*. Third Edition. John Wiley & Sons Inc. (cit. on p. 22).
- Krimmer, J., L. Caponetto, X. Chen, M. Chevallier, D. Dauvergne, M. De Rydt, S.-M. Deng, J.-L. Ley, H. Mathez, C. Ray, V. Reithinger, É. Testa, and Y. Zoccarato (Feb. 1, 2014). “111: Real-time monitoring of the ion range during hadrontherapy: An update on the beam tagging

- hodoscope". In: *Radiotherapy and Oncology* 110, S54–S55. DOI: 10.1016/S0167-8140(15)34132-3. URL: [http://dx.doi.org/10.1016/S0167-8140\(15\)34132-3](http://dx.doi.org/10.1016/S0167-8140(15)34132-3) (cit. on p. 32).
- Kuchment, P and F. Terzioglu (2016). "3D Image Reconstruction from Compton camera data". In: arXiv: 1604.03805 [physics.data-an] (cit. on p. 99).
- Landau, L. (1944). "On the energy loss of fast particles by ionization". In: *J. Phys.(USSR)* 8, pp. 201–205 (cit. on p. 7).
- Larsson, B. (1962). "On the application of a 185 MeV proton beam to experimental cancer therapy and neurosurgery: A biophysical study." PhD thesis. Acta Universitatis Upsaliensis (cit. on p. 12).
- Lawrence, E. O. and M. S. Livingston (Apr. 1932). "The Production of High Speed Light Ions Without the Use of High Voltages". In: *Phys. Rev.* 40 (1), pp. 19–35. DOI: 10.1103/PhysRev.40.19. URL: <https://link.aps.org/doi/10.1103/PhysRev.40.19> (cit. on p. 12).
- Ley, J.-L. (2015). "Mise en oeuvre d'un démonstrateur de caméra Compton pour l'imagerie en médecine nucléaire et pour le contrôle en temps réel de l'hadronthérapie à l'aide des rayonnements gamma prompts." PhD thesis. École Doctorale de Physique et d'Astrophysique de Lyon (cit. on pp. 23, 25, 44, 72, 83).
- Locher, G. L. (1936). "Biological effects and therapeutic possibilities of neutrons". In: *Am. J. Roentgenol. Radium Ther.* 36.1, pp. 1–13 (cit. on p. 12).
- Lojacono, X., M.-H. Richard, J.-L. Ley, É. Testa, C. Ray, N. Freud, J. M. Létang, D. Dauvergne, V. Maxim, and R. Prost (2013). "Low Statistics Reconstruction of the Compton Camera Point Spread Function in 3D Prompt-gamma Imaging of Ion Beam Therapy". In: *IEEE Transactions on Nuclear Science* 60.5, pp. 3355–3363. ISSN: 0018-9499. DOI: 10.1109/TNS.2013.2275200 (cit. on pp. 18, 43, 84).
- Mackin, D., S. Peterson, S. Beddar, and J. Polf (June 7, 2012). "Evaluation of a stochastic reconstruction algorithm for use in Compton camera imaging and beam range verification from secondary gamma emission during proton therapy." eng. In: *Phys Med Biol* 57.11, pp. 3537–3553. DOI: 10.1088/0031-9155/57/11/3537 (cit. on p. 18).
- Matsufuji, N., A. Fukumura, M. Komori, T. Kanai, and T. Kohno (2003). "Influence of fragment reaction of relativistic heavy charged particles on heavy-ion radiotherapy". In: *Physics in Medicine and Biology* 48.11, p. 1605. URL: <http://stacks.iop.org/0031-9155/48/i=11/a=309> (cit. on p. 10).
- Maxim, V. (Jan. 2014). "Filtered Backprojection Reconstruction and Redundancy in Compton Camera Imaging". In: *IEEE Transactions on Image Processing* 23.1, pp. 332–341. ISSN: 1057-7149. DOI: 10.1109/TIP.2013.2288143 (cit. on p. 43).
- Maxim, V., M. Frandes, and R. Prost (2009). "Analytical inversion of the Compton transform using the full set of available projections". In: *Inverse Problems* 25.9, p. 095001. URL: <http://stacks.iop.org/0266-5611/25/i=9/a=095001> (cit. on pp. 18, 43).

Bibliography

- McMillan, E. M. (1945). "The synchrotron - a proposed high energy accelerator." In: *Phys. Rev.* 68.143 (cit. on p. 12).
- Moding, E. J., M. B. Kastan, and D. G. Kirsch (2013). "Strategies for optimizing the response of cancer and normal tissues to radiation." eng. In: *Nat Rev Drug Discov* 12.7, pp. 526–542. DOI: 10.1038/nrd4003 (cit. on p. 5).
- Molière, G. (Feb. 1948). "Theorie der Streuung schneller geladener Teilchen II. Mehrfach- und Vielfachstreuung". In: *Zeitschrift Naturforschung Teil A* 3, pp. 78–97. DOI: 10.1515/zna-1948-0203 (cit. on p. 8).
- National Instruments (2010). *PXI Express - NI PXIe-1082 User Manual*. 372752B-01. National Instruments (cit. on p. 64).
- Nedunchezian, K., N. Aswath, M. Thiruppathy, and S. Thirugnanamurthy (Dec. 2016). "Boron Neutron Capture Therapy - A Literature Review". In: *Journal of Clinical and Diagnostic Research : JCDR* 10.12, ZE01–ZE04. DOI: 10.7860/JCDR/2016/19890.9024 (cit. on p. 12).
- Newhauser, W. D. and M. Durante (May 2011). "Assessing the risk of second malignancies after modern radiotherapy". In: *Nature Reviews Cancer* 11, p. 438. URL: <http://dx.doi.org/10.1038/nrc3069> (cit. on p. 11).
- Newhauser, W. D., U. Titt, D. Dexheimer, X. Yan, and S. Nill (2002). "Neutron shielding verification measurements and simulations for a 235-MeV proton therapy center". In: *Nuclear Instruments and Methods in Physics Research Section A: Accelerators, Spectrometers, Detectors and Associated Equipment* 476.1. Int. Workshop on Neutron Field Spectrometry in Science, Technology and Radiation Protection, pp. 80–84. ISSN: 0168-9002. DOI: [https://doi.org/10.1016/S0168-9002\(01\)01400-0](https://doi.org/10.1016/S0168-9002(01)01400-0). URL: <http://www.sciencedirect.com/science/article/pii/S0168900201014000> (cit. on p. 11).
- Newhauser, W. D. and R. Zhang (2015). "The physics of proton therapy". In: *Physics in Medicine and Biology* 60.8, R155. URL: <http://stacks.iop.org/0031-9155/60/i=8/a=R155> (cit. on pp. 7, 10).
- Newport (2017). *XPS-Q8 Universal High-Performance Motion Controller/Driver*. v.1.4.x. Newport Corporation (cit. on p. 35).
- Nurdan, T. C., K. Nurdan, A. B. Brill, and A. H. Walenta (2015). "Design criteria for a high energy Compton Camera and possible application to targeted cancer therapy". In: *Journal of Instrumentation* 10.07, p. C07018. URL: <http://stacks.iop.org/1748-0221/10/i=07/a=C07018> (cit. on p. 81).
- Oliphant, M. O. (1943). "The acceleration of particles to very high energies". In: *Classified memo submitted to DSIR, United Kingdom, Sept. 1943* (cit. on p. 13).
- Ortega, P. G., I. Torres-Espallardo, F. Cerutti, A. Ferrari, J. E. Gillam, C. Lacasta, G. Llosá, J. F. Oliver, P. R. Sala, P. Solevi, and M. Rafecas (Mar. 7, 2015). "Noise evaluation of Compton camera imaging for proton therapy". eng. In: *Phys Med Biol* 60.5, pp. 1845–1863. DOI: 10.1088/0031-9155/60/5/1845 (cit. on p. 27).

- Paganetti, H. and P. Van Luijk (2013). “Biological Considerations When Comparing Proton Therapy With Photon Therapy”. In: *Seminars in Radiation Oncology* 23.2, pp. 77–87. DOI: 10.1016/j.semradonc.2012.11.002. URL: <http://dx.doi.org/10.1016/j.semradonc.2012.11.002> (cit. on p. 13).
- Parodi, K. (2016). “On- and off-line monitoring of ion beam treatment”. In: *Nuclear Instruments and Methods in Physics Research Section A: Accelerators, Spectrometers, Detectors and Associated Equipment* 809. Advances in detectors and applications for medicine, pp. 113–119. DOI: <https://doi.org/10.1016/j.nima.2015.06.056>. URL: <http://www.sciencedirect.com/science/article/pii/S0168900215008062> (cit. on p. 14).
- Parodi, K., H. Paganetti, H. A. Shih, S. Michaud, J. S. Loeffler, T. F. DeLaney, N. J. Liebsch, J. E. Munzenrider, A. J. Fischman, A. Knopf, and T. Bortfeld (2007). “Patient Study of In Vivo Verification of Beam Delivery and Range, Using Positron Emission Tomography and Computed Tomography Imaging After Proton Therapy”. In: *International Journal of Radiation Oncology Biology Physics* 68.3, pp. 920–934. DOI: 10.1016/j.ijrobp.2007.01.063. URL: <http://dx.doi.org/10.1016/j.ijrobp.2007.01.063> (cit. on p. 14).
- Parra, L. C. (Aug. 2000). “Reconstruction of cone-beam projections from Compton scattered data”. In: *IEEE Transactions on Nuclear Science* 47.4, pp. 1543–1550. DOI: 10.1109/23.873014 (cit. on p. 18).
- Pedroni, E., S. Scheib, T. Bohringer, A. Coray, M. Grossmann, S. Lin, and A. Lomax (Feb. 2005). “Experimental characterization and physical modelling of the dose distribution of scanned proton pencil beams.” eng. In: *Phys Med Biol* 50.3, pp. 541–561 (cit. on p. 9).
- Pinto, M., D. Dauvergne, N. Freud, J. Krimmer, J. M. Létang, C. Ray, F. Roellinghoff, and É. Testa (2014). “Design optimisation of a TOF-based collimated camera prototype for online hadrontherapy monitoring”. In: *Physics in Medicine and Biology* 59.24, p. 7653. URL: <http://stacks.iop.org/0031-9155/59/i=24/a=7653> (cit. on p. 25).
- Richard, M.-H. (2012). “Design study of a Compton camera for prompt-gamma imaging during ion beam therapy”. PhD thesis. Université Claude Bernard - Lyon I (cit. on p. 22).
- Ritt, S. (2009). *9 Channel, 5 GSPS Switched Capacitor Array DRS4*. Revision 0.9. Paul Scherrer Institut (cit. on p. 29).
- Rogers, J. G., R. Nutt, M. Andreaco, and C. W. Williams (Aug. 1994). “Testing 144- and 256-crystal BGO block detectors”. In: *IEEE Transactions on Nuclear Science* 41.4, pp. 1423–1429. DOI: 10.1109/23.322926 (cit. on pp. 46, 72).
- Rutherford, E. (1911). “The scattering of α and β particles by matter and the structure of the atom”. In: *Phil. Mag. Ser.6* 21, pp. 669–688. DOI: 10.1080/14786440508637080 (cit. on p. 8).
- Saint Gobain (2016). *BGO Bismuth Germanate Scintillation material - Datasheet*. Saint Gobain Ceramics & Plastics (cit. on p. 61).

- Saint Gobain (2017). *Plastic Scintillating Fibers - Product brochure*. Saint Gobain Ceramics & Plastics (cit. on pp. 32, 35).
- Sandjong, S., M. Fontana, and É. Testa (2017). “Compton camera prototype for ion beam therapy monitoring: characterization of the BGO scintillators and simulation of the scintillating fiber beam hodoscope”. Master internship report (cit. on p. 27).
- Schall, I., D. Schardt, H. Geissel, H. Irnich, E. Kankeleit, G. Kraft, A. Magel, M. F. Mohar, G. Münzenberg, F. Nickel, C. Scheidenberger, and W. Schwab (1996). “Charge-changing nuclear reactions of relativistic light-ion beams ($5 \leq Z \leq 10$) passing through thick absorbers”. In: *Nuclear Instruments and Methods in Physics Research Section B: Beam Interactions with Materials and Atoms* 117.3, pp. 221–234. ISSN: 0168-583X. DOI: [https://doi.org/10.1016/0168-583X\(96\)00325-4](https://doi.org/10.1016/0168-583X(96)00325-4). URL: <http://www.sciencedirect.com/science/article/pii/0168583X96003254> (cit. on p. 10).
- Schardt, D., T. Elsässer, and D. Schulz-Ertner (Feb. 2010). “Heavy-ion tumor therapy: Physical and radiobiological benefits”. In: *Rev. Mod. Phys.* 82 (1), pp. 383–425. DOI: 10.1103/RevModPhys.82.383. URL: <https://link.aps.org/doi/10.1103/RevModPhys.82.383> (cit. on p. 5).
- Schardt, D., P. Steidl, M. Krämer, U. Weber, K. Parodi, and S. Brons (2008). “Precision Bragg-curve measurements for light-ion beams in water” (cit. on p. 10).
- Schneider, U. and R. Hälg (2015). “The Impact of Neutrons in Clinical Proton Therapy”. In: *Frontiers in Oncology* 5, p. 235. DOI: 10.3389/fonc.2015.00235. URL: <http://www.ncbi.nlm.nih.gov/pmc/articles/PMC4617104/> (cit. on p. 11).
- Schöne, S., G. Shakirin, T. Kormoll, C. M. Herbach, G. Pausch, and W. Enghardt (Oct. 2010). “A common approach to image reconstruction for different applications of Compton cameras”. In: *IEEE Nuclear Science Symposium Medical Imaging Conference*, pp. 2292–2293. DOI: 10.1109/NSSMIC.2010.5874192 (cit. on p. 18).
- Serber, R. (Dec. 1947). “Nuclear Reactions at High Energies”. In: *Phys. Rev.* 72 (11), pp. 1114–1115. DOI: 10.1103/PhysRev.72.1114. URL: <https://link.aps.org/doi/10.1103/PhysRev.72.1114> (cit. on p. 9).
- Singh, M. (1983). “An electronically collimated gamma camera for single photon emission computed tomography. Part I: theoretical considerations and design criteria”. In: *Medical Physics* 10.4, pp. 421–427. ISSN: 2473-4209. DOI: 10.1118/1.595313. URL: <http://dx.doi.org/10.1118/1.595313> (cit. on p. 80).
- Sonoda, S., Y. Ichimura, H. Kimura, S. Kabuki, A. Takada, T. Mizmoto, H. Kubo, S. Miyamoto, S. Komura, T. Takemura, T. Sawano, T. Kishimoto, Y. Matsuoka, Y. Mizumura, and T. Tanimori (2015). “Application of Electron Tracking Compton Camera (ETCC) in medical imaging”. In: *2015 IEEE Nuclear Science Symposium and Medical Imaging Conference (NSS/MIC)*, pp. 1–3. DOI: 10.1109/NSSMIC.2015.7582015 (cit. on p. 99).
- Spieler, H. (1998). “Semiconductor Detectors Part 2”. Lectures on Detector Techniques, Stanford Linear Accelerator Center , September 1998 - February, 1999 (cit. on p. 45).

- Stone, R. S. (June 1948). "Neutron therapy and specific ionization." eng. In: *Am J Roentgenol Radium Ther* 59.6, pp. 771–785 (cit. on p. 12).
- Stone, R. S., J. H. Lawrence, and P. C. Aebersold (1940). "A Preliminary Report on the Use of Fast Neutrons in the Treatment of Malignant Disease". In: *Radiology* 35.3, pp. 322–327. DOI: 10.1148/35.3.322. eprint: <https://doi.org/10.1148/35.3.322>. URL: <https://doi.org/10.1148/35.3.322> (cit. on p. 12).
- Takeda, S., T. Takahashi, S. Watanabe, H. Tajima, T. Tanaka, K. Nakazawa, and Y. Fukazawa (Jan. 2008). "Double-sided silicon strip detector for x-ray imaging". In: (cit. on p. 23).
- Terasic (2009). *SFP HSMC Terasic Board User Manual*. Revision 1. Terasic Technologies Inc. (cit. on p. 30).
- Terasic (2015). *SoCKit User Manual*. Revision F. Terasic Technologies Inc. (cit. on p. 30).
- Thun, M. J., J. O. DeLancey, M. M. Center, A. Jemal, and E. M. Ward (Jan. 2010). "The global burden of cancer: priorities for prevention". In: *Carcinogenesis* 31.1, pp. 100–110. DOI: 10.1093/carcin/bgp263. URL: <http://www.ncbi.nlm.nih.gov/pmc/articles/PMC2802672/> (cit. on p. 4).
- Tobias, C. A., E. A. Blakely, E. L. Alpen, J. R. Castro, E. J. Ainsworth, S. B. Curtis, F. Q. H. Ngo, A. Rodriguez, R. J. Roots, T. Tenfordf, and T. C. H. Yang (1982). "Molecular and cellular radiobiology of heavy ions". In: *International Journal of Radiation Oncology*Biology*Physics* 8.12. Particle Accelerators in Radiation Therapy, pp. 2109–2120. ISSN: 0360-3016. DOI: [https://doi.org/10.1016/0360-3016\(82\)90554-5](https://doi.org/10.1016/0360-3016(82)90554-5). URL: <http://www.sciencedirect.com/science/article/pii/0360301682905545> (cit. on p. 5).
- Tobias, C. A., J. H. Lawrence, J. L. Born, R. K. McCombs, J. E. Roberts, H. O. Anger, B. V. A. Low-Beer, and C. B. Huggins (1958). "Pituitary Irradiation with High-Energy Proton Beams. A Preliminary Report". In: *Cancer Research* 18.2, pp. 121–134. eprint: <http://cancerres.aacrjournals.org/content/18/2/121.full.pdf>. URL: <http://cancerres.aacrjournals.org/content/18/2/121> (cit. on pp. 5, 12).
- Tobias, C. A., J. E. Roberts, J. H. Lawrence, B. V. A. Low-Beer, H. O. Anger, and J. L. Born (1955). "Irradiation Hypophysectomy and related studies using 340 MeV protons an 190 MeV deuterons". In: *Lawrence Berkeley National Laboratory. LBNL Report UCRL-2907* (cit. on pp. 5, 12).
- Tornai, M. P., G. Germano, and E. J. Hoffman (Aug. 1994). "Positioning and energy response of PET block detectors with different light sharing schemes". In: *IEEE Transactions on Nuclear Science* 41.4, pp. 1458–1463. ISSN: 0018-9499. DOI: 10.1109/23.322931 (cit. on pp. 46, 72).
- Tsai, Y.-S. (1974). "Pair Production and Bremsstrahlung of Charged Leptons". In: *Rev. Mod. Phys.* 46. [Erratum: *Rev. Mod. Phys.* 49, 521(1977)], p. 815. DOI: 10.1103/RevModPhys.46.815, 10.1103/RevModPhys.49.421 (cit. on p. 9).
- Uribe, J., H. Li, T. Xing, Y. Liu, H. Baghaei, Y. Wang, M. Aykac, R. Ramirez, and W.-H. Wong (June 2003). "Signal characteristics of individual crystals in high resolution BGO detector designs

Bibliography

- using PMT-quadrant sharing”. In: *IEEE Transactions on Nuclear Science* 50.3, pp. 355–361. DOI: 10.1109/TNS.2003.812478 (cit. on p. 61).
- Vallois, Y. (2016). “Test d’un hodoscope de faisceau à fibres scintillantes”. Master internship report (cit. on p. 67).
- Vavilov, P. V. (1957). “Ionization losses of high-energy heavy particles”. In: *Sov. Phys. JETP* 5. [Zh. Eksp. Teor. Fiz. 32, 920(1957)], pp. 749–751 (cit. on pp. 7, 8).
- Veksler, V. I. (1944). “A new method of accelerating relativistic particles.” In: *Comptes Rendus (Dokal'dy) de l'Academie Sciences de l'URSS* 43.8, pp. 329–331 (cit. on p. 12).
- Webb, S. (2009). “The contribution, history, impact and future of physics in medicine”. In: *Acta Oncologica* 48, pp. 169–177. DOI: 10.1080/02841860802244158 (cit. on p. 4).
- WeissTechnik (2017). *Products brochure*. rev. Jan 2017. Weiss Technik North America, Inc. (cit. on p. 44).
- Widerøe, R. (1928). “Über ein neues Prinzip zur Herstellung hoher Spannungen”. In: *Arch. Elektrotech.* 21, pp. 387–406. URL: <http://cds.cern.ch/record/434681> (cit. on p. 12).
- Wilson, R. (2004). *A brief history of the Harvard cyclotrons*. Harvard University Press (cit. on p. 12).
- Wilson, R. R. (1946). “Radiological Use of Fast Protons”. In: *Radiology* 47.5. PMID: 20274616, pp. 487–491. DOI: 10.1148/47.5.487. eprint: <https://doi.org/10.1148/47.5.487>. URL: <https://doi.org/10.1148/47.5.487> (cit. on pp. 5, 12).
- Wroe, A. J., I. M. Cornelius, and A. B. Rosenfeld (n.d.). “The role of nonelastic reactions in absorbed dose distributions from therapeutic proton beams in different medium”. In: *Medical Physics* 32.1 (), pp. 37–41. DOI: 10.1118/1.1824194. eprint: <https://aapm.onlinelibrary.wiley.com/doi/pdf/10.1118/1.1824194>. URL: <https://aapm.onlinelibrary.wiley.com/doi/abs/10.1118/1.1824194> (cit. on p. 10).
- Yan, X., U. Titt, A. M. Koehler, and W. D. Newhauser (2002). “Measurement of neutron dose equivalent to proton therapy patients outside of the proton radiation field”. In: *Nuclear Instruments and Methods in Physics Research Section A: Accelerators, Spectrometers, Detectors and Associated Equipment* 476.1. Int. Workshop on Neutron Field Spectrometry in Science, Technology and Radiation Protection, pp. 429–434. ISSN: 0168-9002. DOI: [https://doi.org/10.1016/S0168-9002\(01\)01483-8](https://doi.org/10.1016/S0168-9002(01)01483-8). URL: <http://www.sciencedirect.com/science/article/pii/S0168900201014838> (cit. on p. 11).
- Zoglauer, A., R. Andritschke, and F. Schopper (2006). “MEGAlib The Medium Energy Gamma-ray Astronomy Library”. In: *New Astronomy Reviews* 50, pp. 629–632. DOI: 10.1016/j.newar.2006.06.049 (cit. on p. 84).
- Zoglauer, A., E. S. Boggs, M. Galloway, M. Amman, N. P. Luke, and R. Kippen (Oct. 2011). “Design, implementation, and optimization of MEGAlib’s image reconstruction tool Mimrec”. In: 652, pp. 568–571 (cit. on p. 18).

Index

- Abbassi, L., 135
Abe, M., 137
Abellan, C., 37, 131
Adam, L. E., 26, 131
Adam, L.-E., 133
Aebersold, P. C., 142
Ainsworth, E. J., 143
Akagi, T., 137
Alpen, E. L., 143
Altera, 24, 29, 33, 35, 37, 131
Amaldi, U., 134
Amman, M., 144
Andreaco, M., 141
Andritschke, R., 144
Anger, H. O., 80, 131, 143
Aspen Aerogels, 25, 131
Aswath, N., 140
Aykac, M., 143
Böttcher, S., 135
Baghaei, H., 143
Barrio, J., 136
Barth, R. F., 12, 131
Baskar, R., 5, 131
Basko, R., 18, 131
Bauer, J., 14, 131
Beddar, S., 139
Bellemann, M. E., 131, 133
Bentzen, S. M., 5, 132
Berger, M. J., 137
Bes, A., 135, 136
Bethe, H., 7, 132
Bhat, M. R., xi, 82, 132
Biegun, A. K., 137
Blakely, E. A., 5, 132, 143
Bloch, F., 7, 132
Blue, T. E., 131
Boggs, E. S., 144
Bohr, N., 7, 132
Bohringer, T., 141
Bones, P. J., 134
Born, J. L., 143
Bortfeld, T., 140
Bosson, G., 135, 136
Bothe, W., 8, 132
Boukhémiri, A., 136
Braccini, S., 11, 132
Bragg, W. H. M. A., 6, 7, 132
Brahme, A., 5, 133
Breton, D., 47, 133
Brill, A. B., 140
Brix, G., 26, 131, 133
Brons, S., 142
Brun, R., vii, 39–41, 49, 133
Brunner, S. E., 73, 133
Bui, F., 133
Buvat, I., 137
Cachemiche, J.-P., 131
Cachemiche, J.-P., 37, 133
Candela Juan, C., 136
Cantor, D., 4, 133
Caponetto, L., 138
Castro, J. R., 143
Catterall, M., 12, 133
Cecchin, D., 92, 133
Center, M. M., 138, 143
Cerutti, F., 140
Chang, P. Y., 132
Chen, X., 25, 35, 133, 138
Chevallier, M., 138
Clinthorne, N., 137
Coderre, J. A., 131
Collot, J., 135, 136
Combs, S. E., 131
Coray, A., 141
Cornelius, I. M., 144
Coudurier, V., 64, 133
Cree, M. J., 18, 134
Crespo, P., 135
Crozes, T., 135
Curtis, S. B., 143
Curtoni, S., 135
Dahoumane, M., 24, 25, 134
Dauvergne, D., 134–136, 138, 139, 141
De Marchi, S., 133
De Nolf, W., 135
De Rydt, M., 138
Debus, J., 131
Degiovanni, A., 11, 134
Delagnes, E., 133
DeLancey, J. O., 143
DeLaney, T. F., 140
Dendooven, P., 137
Deng, S.-M., 33, 134, 138

- DeSantis, C., 138
Despeignes, V., 4, 134
Dexheimer, D., 140
Doll, J., 133
Duck, F. A., 4, 134
Durante, M., vii, 5, 7–10, 134, 135, 140
Duval, P. Y., 133

Elftmann, R., 27, 135
Elsässer, T., 135
Elsässer, T., 142
Enghardt, W., 14, 135, 137, 142
Evans, T. C., 4, 135
Everett, D. B., 80, 135

Ferrari, A., 140
Fiedler, F., 135, 137
Field, S. B., 133
Fischman, A. J., 140
Fleming, J. S., 135
Fontana, M., 79, 135, 136, 141
Foray, N., 4, 135
Frandes, M., 139
Freud, N., 139, 141
Friedrich, T., 5, 135
Fukazawa, Y., 142
Fukumura, A., 139

Gaglione, R., 64, 135
Gallin-Martel, L., 135, 136
Gallin-Martel, M.-L., 74, 135, 136
Galloway, M., 144
GE Healthcare, 80, 86, 136
GeckoDrive, 64, 136
Geissel, H., 141
Germano, G., 143
Gillam, J. E., 18, 136, 140
Golnik, C., 46, 72, 136, 137
Gorecki, A., 136
Gottschalk, B., 8, 11, 136
Grassberger, C., 10, 136
Grossmann, M., 141
Gruber, L., 133
Gullberg, G. T., 131
Gunzert-Marx, K., 10, 136

Hüfner, J., 9, 138
Haberer, T., 131
Haberkorn, U., 133
Hachon, F., 133
Haettner, E., 10, 136, 137

Halperin, E. C., 5, 137
Hamamatsu, 32, 62, 64, 69, 137
Han, L., 80, 81, 83, 98, 137
Hattori, K., 138
Heidel, K., 137
Herbach, C. M., 142
Herfarth, K., 131
Highland, V. L., 8, 137
Hilaire, E., 43, 137
Hinz, R., 135
Hirasawa, M., 18, 137
Hirtl, A., 133
Hishikawa, Y., 14, 137
Hoffman, E. J., 143
Hostachy, J. Y., 136
Hostachy, J.-Y., 135
Hubbell, J. H., 87, 99, 137
Hueso-González, F., 27, 46, 72, 137
Huggins, C. B., 143
Huh, S. S., 137
Hälg, R., 142

Ichimura, Y., 142
ICRU, 13, 138
Irnich, H., 141
Iwase, H., 136, 137

Jemal, A., 4, 138, 143

Kabuki, S., 99, 138, 142
Kagawa, K., 137
Kanai, T., 139
Kankeleit, E., 141
Kastan, M. B., 139
Keevil, S. F., 4, 138
Kereiakes, J. G., 4, 138
Kimura, H., 142
Kippen, R., 144
Kirsch, D. G., 139
Kishimoto, T., 142
Kleeman, R., 132
Knoll, G. F., 22, 138
Knopf, A., 140
Koehler, A. M., 136, 144
Kohara, R., 138
Kohn, T., 139
Komori, M., 139
Komura, S., 142
Kormoll, T., 137, 142
Krämer, M., 136, 142

- Kraft, G., 136, 141
Krimmer, J., 32, 134–136, 138, 141
Kubo, A., 138
Kubo, H., 138, 142
Kuchment, P., 99, 138
Kulkarni, S. R., 135
Kunieda, E., 138
Kurz, C., 131

Létang, J. M., 135, 139, 141
Lacasta, C., 136, 140
Lacoste, A., 135, 136
Landau, L., 7, 138
Larsson, B., 12, 138
Lawrence, E. O., 12, 139
Lawrence, J. H., 142, 143
Le Gac, R., 133
Lee, K. A., 131
Ley, J.-L., 23, 25, 44, 72, 83, 134, 135, 138, 139
Li, H., 143
Liebsch, N. J., 140
Lin, S., 141
Liu, Y., 143
Livingston, M. S., 139
Llosá, G., 136, 140
Locher, G. L., 12, 139
Loeffler, J. S., 134, 140
Lojacono, X., 18, 43, 84, 137, 139
Lomax, A., 141
Lorenz, W., 133
Low-Beer, B. V. A., 143
Lu, G.-N., 134
Luke, N. P., 144

Maalmi, J., 133
Mackin, D., 18, 139
Magel, A., 141
Marcatili, S., 135, 136
Martin, C., 135
Marton, J., 133
Mathez, H., 134, 138
Matsufuji, N., 10, 139
Matsuoka, Y., 142
Maxim, V., 18, 43, 135, 137, 139
McCombs, R. K., 143
McMillan, E. M., 12, 139
Michaud, S., 140
Miuchi, K., 138
Miyamoto, S., 142

Mizmoto, T., 142
Mizumura, Y., 142
Moding, E. J., 5, 139
Mohar, M. F., 141
Molière, G., 8, 139
Morel, C., 131
Morse, J., 135, 136
Motte, J.-F., 135
Munzenrider, J. E., 140
Murakami, M., 137
Muraz, J. F., 136
Muraz, J.-F., 135
Münzenberg, G., 141

Nagayoshi, T., 138
Nakahara, T., 138
Nakazawa, K., 142
National Instruments, 64, 139
Nedunchezhian, K., 12, 140
Newhauser, W. D., 7, 10, 11, 140, 144
Newport, 35, 140
Ngo, F. Q. H., 143
Nickel, F., 141
Nightingale, J. M., 135
Nill, S., 140
Nishimura, H., 138
Nurdan, K., 140
Nurdan, T. C., 81, 140
Nutt, R., 141

Oberdorfer, F., 133
Okada, Y., 138
Oliphant, M. O., 13, 140
Oliver, J. F., 140
Orito, R., 138
Ortega, P. G., 27, 140
Ostertag, H., 131, 133

Paganetti, H., 13, 135, 136, 140
Parodi, K., 14, 131, 135, 140, 142
Parra, L. C., 18, 141
Pausch, G., 137, 142
Pawelke, J., 135
Pedroni, E., 9, 141
Peterson, S., 139
Petzoldt, J., 137
Peyrin, F., 137
Pinto, M., 25, 141
Poggiali, D., 133
Polf, J., 139

- Prost, R., 139
Pönisch, F., 135

Römer, K. E., 137
Réthoré, F., 131
Rademakers, F., 133
Rafecas, M., 136, 140
Ramirez, R., 143
Rarbi, F. E., 135, 136
Ray, C., 134, 138, 139, 141
Reithinger, V., 138
Riccardin, L., 133
Richard, M.-H., 22, 139, 141
Ritt, S., 29, 141
Robert, C., 137
Roberts, J. E., 143
Rodriguez, A., 143
Roellinghoff, F., 141
Rogers, C., 133
Rogers, J. G., 46, 72, 141
Rogers, W. L., 137
Roots, R. J., 143
Rosenfeld, A. B., 144
Rossetto, O., 135, 136
Rusquart, P., 133
Rutherford, E., 8, 141
Réthoré, F., 133

Saint Gobain, 32, 35, 61, 141
Sakai, H., 137
Sala, P. R., 140
Salomé, M., 135, 136
Sandjong, S., 27, 141
Sarrut, D., 137
Sawano, T., 142
Schäfer, K., 138
Schöne, S., 18, 142
Schürmann, B., 138
Schaart, D. R., 133
Schall, I., 10, 141
Schardt, D., 5, 10, 136, 137, 141, 142
Scheib, S., 141
Scheidenberger, C., 141
Schneider, R. J., 136
Schneider, U., 11, 142
Scholz, M., 135
Scholz, U., 135
Schopper, F., 144
Schulz-Ertner, D., 142
Schwab, W., 141

Schwengner, R., 137
Sekiya, H., 138
Serber, R., 9, 142
Shakirin, G., 142
Shih, H. A., 140
Shirahata, T., 138
Simon, R. S., 136
Singh, M., 80, 142
Sisteron, J. M., 136
Solevi, P., 136, 140
Sommerer, F., 131
Sonoda, S., 99, 142
Spieler, H., 45, 142
Steidl, P., 142
Stone, R. S., 12, 142
Suzuki, K., 133

Tajima, H., 142
Takada, A., 138, 142
Takahashi, T., 142
Takeda, S., 23, 142
Takemura, T., 142
Tammen, J., 135
Tanaka, T., 142
Tanimori, T., 138, 142
Tenfordf, T., 143
Terasic, 30, 142
Terzioglu, F., 138
Testa, É., 134–136, 138, 139, 141
Thirugnanamurthy, S., 140
Thiruppathy, M., 140
Thomlinson, R. H., 133
Thun, M. J., 4, 143
Titt, U., 140, 144
Tobias, C. A., 5, 12, 143
Todd, R. W., 135
Tomitani, T., 137
Tornai, M. P., 46, 72, 143
Torres-Espallardo, I., 136, 140
Trojan, H., 131, 133
Tsai, Y.-S., 9, 143
Turco, P., 133

Ueno, K., 138
Unholtz, D., 131
Uribe, J., 61, 143

Vallois, Y., 67, 143
Van Luijk, P., 140
Vavilov, P. V., 7, 8, 143

- Veksler, V. I., 12, 143
Vicente, M. G. H., 131
Vuiaut, R., 135
- Wagner, A., 137
Wagner, M. S., 136
Walenta, A. H., 134, 140
Wang, Y., 143
Ward, E. M., 138, 143
Watanabe, S., 142
Webb, S., 4, 143
Weber, U., 142
WeissTechnik, 44, 143
Welzel, T., 131
Widerøe, R., 12, 144
Williams, C. W., 141
Wilson, R., 12, 144
Wilson, R. R., 5, 12, 144
Wimmer-Schweingruber, R., 135
Wong, W.-H., 143
Wroe, A. J., 10, 144
- Xing, T., 143
- Yamouni, M., 135, 136
Yan, X., 11, 140, 144
Yang, T. C. H., 143
Yeo, R., 131
Yeoh, K.-W., 131
- Zaers, J., 131, 133
Zeng, G. L., 131
Zhang, R., 140
Zoccarato, Y., 134, 138
Zoglauer, A., 18, 84, 144

Acknowledgements